



저작자표시-비영리-변경금지 2.0 대한민국

이용자는 아래의 조건을 따르는 경우에 한하여 자유롭게

- 이 저작물을 복제, 배포, 전송, 전시, 공연 및 방송할 수 있습니다.

다음과 같은 조건을 따라야 합니다:



저작자표시. 귀하는 원저작자를 표시하여야 합니다.



비영리. 귀하는 이 저작물을 영리 목적으로 이용할 수 없습니다.



변경금지. 귀하는 이 저작물을 개작, 변형 또는 가공할 수 없습니다.

- 귀하는, 이 저작물의 재이용이나 배포의 경우, 이 저작물에 적용된 이용허락조건을 명확하게 나타내어야 합니다.
- 저작권자로부터 별도의 허가를 받으면 이러한 조건들은 적용되지 않습니다.

저작권법에 따른 이용자의 권리는 위의 내용에 의하여 영향을 받지 않습니다.

이것은 [이용허락규약\(Legal Code\)](#)을 이해하기 쉽게 요약한 것입니다.

[Disclaimer](#)

Magnetic resonance imaging using additional gradient for fast acquisition and artifact correction



The Graduate School
Yonsei University

Magnetic resonance imaging using additional gradient for fast acquisition and artifact correction

A Dissertation

Submitted to the Department of Electrical and Electronic Engineering

and the Graduate School of Yonsei University

in partial fulfillment of the

requirements for the degree of

Doctor of Philosophy

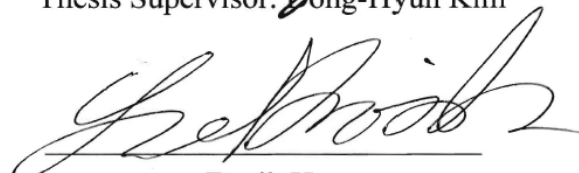
Min-Oh Kim

February 2016

This certifies that the dissertation
of Min-Oh Kim is approved.



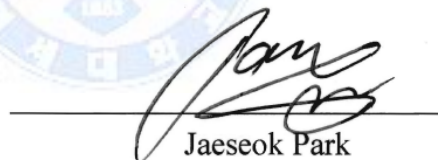
Thesis Supervisor: Dong-Hyun Kim



Dosik Hwang



Jongduk Baek



Jaeseok Park



Jongho Lee

The Graduate School
Yonsei University
February 2016

감사의 글 (Acknowledgment)

2009년 3월에 통합과정을 시작해서 7년이라는 긴 수학기간 끝에 박사 학위를 받게 되었습니다. 오랜 학위 과정 기간 동안 많은 도움을 주신 분들께 감사의 글을 올립니다.

먼저 30년이 넘는 세월 동안 당신의 자리에서 한결같이 응원해주신 아버지, 무한한 사랑으로 격려해주고 뒷바라지해주신 어머니께 진심으로 감사드립니다. 감정 표현을 잘 하지 않는 무뎡뎡한 아들이지만 항상 사랑하고 존경하는 마음을 가지고 있습니다. 고맙습니다. 요즘 건강이 나빠진 것 같아서 많이 염려되는데 앞으로 더 효도할 수 있도록 건강하셔야 합니다. 그리고 집을 떠나와 오랜 서울 생활 동안 곁에 있었지만 이제는 한 사람의 아내이자 엄마가 된 우리 누나들, 공부하는 동생에게 늘 의지가 되어줘서 고맙고 사랑합니다.

의료 영상 연구실, MILAB 동료들에게도 감사의 뜻을 전합니다. 열정적으로 토의하면서 많은 것을 가르쳐준 상영이형, 함께 밤새 실험하며 고생이 많았던 한성이형, 걸으면 무뎡뎡하지만 정이 많은 성민이형, 항상 이야기를 잘 들어주었던 천사같은 윤호형, 칙칙한 연구실 분위기를 밝게 만들어준 나래, 연구주제는 달랐지만 고양이로 공감했던 은혜, 영어 논문 작성에 도움을 많이 주었던 승욱이, 연구에 집중할 수 있게 연구실의 행정 업무를 도맡아주신 연주 선생님, 공감대가 있어 많은 이야기를 나눌 수 있었던 동엽이, 힘든 연구 주제를 도맡아 많은 도움을 준 재욱이, 포닥의 센스를 보여준 준성이형, 시퀀스 연구에 흥미를 느끼기 시작한 홍표, 13C 차기 주자 한솔이, 축구 캐릭터가 유사한 조성민, 하나하나 차근차근 일을 해나가는 태화, 의사소통이 쉽진 않지만 항상 밝게 인사해준 Saeed, 어려운 실험을 꾸준히 해나가는 준형이, 연구실 분위기 메이커 재은이, 이해력 좋은 신입 강현이까지, 연구실 사람들 모두 정말 감사합니다.

그리고 자기공명영상의 기본 지식을 쌓고 물리학적 뼈대를 세우는데 큰 도움을 주신 박재석 교수님, 학위 과정 동안 의료 영상 전반에 대한 지식뿐만 아니라 연구적으로도 많은 지도를 해주신 황도식 교수님, 학위 논문의 완성도를 높일 수 있도록 제 연구에 대한 많은 관심과 응원을 해주신 이종호 교수님, 먼 길 마다하지 않고 오셔서 학위 심사를 해주신 백종덕 교수님께 다시 한번 고개 숙여 감사드립니다.

마지막으로 7년간 저를 지도해주신 김동현 교수님. 자유롭게 연구할 수 있도록 지도해주신 것 진심으로 감사드립니다. 학위 과정 초반에는 주어진 일을 하는 것에만 익숙했던 저에게 ‘자유로운 연구’는 굉장히 막연한 일로 다가왔었습니다. 점진적으로 계획을 세우고 함께 확인해가며 꾸준히 연구를 진행했고 교수님께서 격려하며 잘 인도해주신 덕분에 이제는 자유롭게 상상하고 스스로 계획하고 즐겁게 연구하는 방법을 배운 것 같습니다. 뿐만 아니라 교수님이 학문을 대하는 자세를 통해 익숙하지 않은 분야를 열린 눈으로 바라보는 자세를 배웠습니다. 감사합니다.

박사 학위 과정 동안 함께 해주고 응원해준 모든 분들께 다시 한번 감사하다는 말을 전하며 글을 마칩니다.

2016년 겨울 김민오 드림

Content

List of Figures.....	iv
List of Tables.....	v
Abstract	1
1. Introduction.....	3
1.1 Thesis outline	4
2. MRI Basics and Background Knowledge.....	6
2.1 MRI Basics.....	6
2.1.1 Bloch Equation	6
2.1.2 Static Magnetic Field B_0	7
2.1.3 Radiofrequency Field B_1	7
2.1.4 Gradient Fields and Spatial Encoding	8
2.2 Fast Imaging Techniques	10
2.2.1 Imaging Trajectory	10
2.2.2 Parallel Imaging	12
2.2.3 Simultaneous Multislice Acquisition and Wideband Imaging.....	14
2.3 Artifacts	16
2.3.1 Common Artifacts	16
2.3.2 Chemical Shift Artifact and View Angle Tilting	17
2.3.3 Partial Volume Effect	19
2.3.4 B_1 Inhomogeneity Artifact.....	20
3. Multi and Wideband Imaging for Fast Data Acquisition	21
3.1 Introduction.....	21
3.2 CAIPIRINHA and VAT for Multiband Excitation and Bi-direction Shifts	24
3.2.1 Multiband RF and CAIPI shift	24
3.2.2 VAT shift	24
3.3 CAIPIVAT Simulation and Experiment.....	26
3.3.1 Performance Evaluation with Simulation	26
3.3.2 Phantom and invivo Head Experiment	27

3.4 Wideband imaging with Aliasing Separation Gradients	30
3.4.1 Pulse Sequence for 2D and 3D Wideband Imaging	30
3.4.2 Voxel Shearing in Image Domain	32
3.4.3 Wideband Reconstruction	35
3.5 Wideband Experiments	35
3.5.1 Voxel Shearing in Grid Phantom Experiment	36
3.5.2 Parallel Imaging with GRAPPA Technique	38
3.5.3 Invivo Head Experiment	38
3.6 Discussions	41
3.6.1 Multiband Imaging	41
3.6.2 Wideband Imaging	42
4. MR Tomosynthesis	45
4.1 Introduction	45
4.2 Materials and Methods	46
4.2.1 MOV Pulse Sequence	46
4.2.2 Image Reconstruction	49
4.2.3 Simulations	53
4.2.4 Data Acquisition and Reconstruction	54
4.2.4 SNR Analysis	55
4.3 Results	56
4.3.1 Simulations	56
4.3.2 Experiments	59
4.4 Discussion	63
5. Fast B_1^+ Mapping and Correction in bSSFP	66
5.1 Introduction	66
5.2 Methods	68
5.2.1 B_1^+ Estimation Pulse Sequence	68
5.2.2 B_1^+ Estimation Error Simulation	70
5.2.3 Experiments	70
5.3 Results	71
5.3.1 Simulation	71
5.3.2 Experiments	72

5.4 Discussion.....	75
6. Summary	79
References.....	82
국문요약	93



List of Figures

Figure 2.1 Two illustrative figures of slice selection and thickness control	9
Figure 2.2 Spin diagrams during spatial encoding process	10
Figure 2.3 EPI pulse sequence and k-space trajectory	11
Figure 2.4 Spiral pulse sequence and k-space trajectory	11
Figure 2.5 Illustrations of SENSE parallel imaging	13
Figure 2.6 RF pulse design for multiband excitation.....	14
Figure 2.7 Example images of SMA.....	15
Figure 2.8 Multiband excitation and CAIPIRINHA shift	16
Figure 2.9 Example images of common MR artifacts	16
Figure 2.10 VAT pulse sequence diagram	18
Figure 2.11 Illustrations of VAT principle and example images	19
Figure 3.1 Pulse sequence diagram and illustrations of CAIPIVAT shift	25
Figure 3.2 SNR simulation of simultaneous two-slice imaging.....	27
Figure 3.3 Water-fat-air phantom model experiments using CAIPI and CAIPIVAT	28
Figure 3.4 invivo brain experiments using CAIPI and CAIPIVAT.....	29
Figure 3.5 Pulse sequence diagrams of extended wideband imaging and illustrative figures of its principle	31
Figure 3.6 Illustrations of voxel shearing.....	34
Figure 3.7 Grid phantom experiment results	37
Figure 3.8 GRAPPA reconstruction process	39

Figure 3.9 6x and 12x Invivo 3D head imaging	40
Figure 4.1 MOV pulse sequence diagram	46
Figure 4.2 X-ray tomosynthesis vs. MRT	47
Figure 4.3 Impulsive bar response to MOV sequence	48
Figure 4.4 PSFs of 3DFT and three MRT reconstruction techniques.....	56
Figure 4.5 Simulation results using numerical high resolution 3D phantom.....	57
Figure 4.6 SNR simulation results on 3D Shepp-logan phantom.....	58
Figure 4.7 Acquired raw images using MOV pulse sequence	59
Figure 4.8 Phantom experiment results of MRT	60
Figure 4.9 Invivo experiment results of MRT	60
Figure 4.10 All axial slices of 3D imaging using 3DFT and MRT	62
Figure 5.1 Pulse sequence diagram for B_1^+ estimation	68
Figure 5.2 Simulation result of B_1^+ estimation error	72
Figure 5.3 Phantom experiment along flip angle variation.....	73
Figure 5.4 Step-by-step presentation of B_1^+ mapping and correction in phantom	74
Figure 5.5 Invivo brain and liver experiment results.....	75

List of Tables

Table 4.1 Overview of MRT performances compared to 3DFT	61
---	----

Abstract

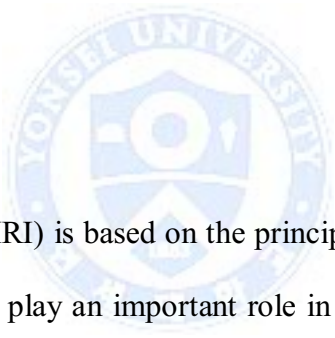
Magnetic resonance imaging using additional gradient for fast acquisition and artifact correction

Min-Oh Kim

Dept. of Electrical and Electronic Eng.

The Graduate School

Yonsei University



Magnetic resonance imaging (MRI) is based on the principle of nuclear magnetic resonance (NMR). Gradient magnetic fields play an important role in the transition from NMR to MRI because they can encode the spatial information of spins by creating additional magnetic fields depending on the spatial position. Furthermore, gradient fields are used in various MR applications with special patterns of gradient sequence such as in saturation, preparation, motion sensing, etc. New gradient coils are continuously being developed and their performances such as maximum amplitude, duty cycle, and slew rate are getting higher. This dissertation focuses on the applications of additional gradients for fast acquisition and artifact correction.

Three applications using additional gradients are presented in this thesis: Multi and wideband imaging, MR tomosynthesis (MRT), and fast B_1^+ mapping and correction methods.

These methods are aimed to improve MRI performance and image quality by reducing scan time and alleviating image artifacts.

In multi and wideband imaging methods, additional gradients are applied during readout time and these gradients tilt images along the specific direction. This technique can separate or shift the aliased regions caused by undersampled phase encodings (PEs). In multiband imaging, fast acquisition is achieved by modifying the radio-frequency (RF) pulse to excite multislice simultaneously. Using an additional gradient, the inverse problem in slice parallel imaging can be conditioned better. In wideband imaging, aliasing in two dimensional (2D) and three dimensional (3D) images are separated and moved to readout direction. By reducing the total number of PEs, total scan time can be reduced significantly.

In the second application termed MRT, the additional gradient is also applied during readout time. By varying the amplitude of this gradient, several 2D images are acquired and these images are reconstructed similar to 3D images using tomosynthesis algorithm used in x-ray system. With this technique, partial volume artifact can be reduced along specific direction and aliasing along slice direction in 3D imaging can be resolved as well.

In the third application, two trajectories are used in one pulse sequence for fast B_1^+ mapping and imaging. In balanced steady-state free precession (bSSFP), spiral readout is adapted during the transient-state to acquire B_1^+ information and following bSSFP image is acquired using Cartesian trajectory. B_1^+ map and bSSFP image are acquired sequentially, therefore, spatial intensity modulation induced by B_1^+ inhomogeneity in bSSFP image can be compensated using this B_1^+ information

Keywords: magnetic resonance imaging, gradient manipulation, fast imaging, artifact correction.

Chapter 1

Introduction

Magnetic resonance imaging (MRI) is widely used in both clinical and research fields because of its distinct advantages. It is based on nuclear induction phenomenon (1) facilitated by magnetic field and radio frequency (RF) wave. It makes MRI relatively safe modality since it is free from the exposure to the ionizing radiation in x-ray and computed tomography (CT). Furthermore, it gives excellent contrasts depending on the tissue properties such as relaxation parameters, structures, and compositions. In addition, advanced imaging techniques are also possible, that reflects chemical composition (2), physiological properties (3,4), neural activation (5), temperature (6), electric (7) and magnetic properties (8), etc.

In spite of these advantages, the imaging time of MRI is relatively longer than that of other clinical imaging modalities. In general, total scan time of MRI is tens of minutes and it is proportional to the spatial resolution, field-of-view (FOV), signal-to-noise ratio (SNR) and the number of applied pulse sequences. To reduce the imaging time, a lot of fast imaging techniques have been developed such as multiecho techniques, fast acquisition trajectories, undersampling and reconstruction techniques, simultaneous multislice acquisition, etc. In these techniques, it is important to achieve scan time reduction while minimizing the decrements of SNR and spatial resolution. Several fast imaging techniques are briefly described in chapter 2.

MR artifacts which degrade the image quality are problematic in diagnosis and research using MRI. There are a lot of artifacts and they come from various sources such as physical, chemical and physiological effects, signal generation, reception and sampling, hardware imperfections, etc. Compensating or utilizing these artifacts is a key factor in technical developments of MRI. .

Three methods introduced in this dissertation are focused on fast imaging and artifact corrections. Those techniques are utilized by designing new pulse sequences with additional gradients. For fast acquisition, modified multi and wideband imaging techniques are proposed. The idea behind these techniques is that aliasing from undersampling can be decomposed and separated to readout direction by applying appropriate gradients during data acquisition. Another technique is for reducing partial volume and slice aliasing artifacts. Projection 2D images at different view angles are acquired and reconstructed to 3D image. The last one aims to compensate B_1^+ induced intensity modulation. In Cartesian bSSFP imaging, additional spiral acquisitions are introduced to estimate B_1^+ quickly at transient-state with variable flip angles.

1.1 Thesis Outline

In chapter 2, the basic components of MRI and background knowledge are covered. The basic MR physics are briefly described to give an insight to MR signal generation and acquisition. In addition, the common fast imaging techniques and MR artifacts are introduced to help understanding the following imaging techniques in this dissertation.

Additional gradients play an important role in the following chapters. In chapter 3, modified multi and wideband imaging techniques are proposed. Using the additional gradients, acceleration in data acquisition and improvement in the reconstructed image are achieved by introducing the readout directional shifts depending on the location along the slice direction.

In chapter 4, MR tomosynthesis (MRT) technique is introduced. This method uses tomosynthesis reconstruction originated from x-ray image to make 3D image from several 2D projection images. Slice (volume) selective projection images with different projection angles are acquired by adjusting the amplitude of the additional gradient. Several tomosynthesis

reconstruction techniques are reformatted to MR imaging situation and the pros and cons of MRT are discussed.

In chapter 5, the concept using additional gradients is slightly different to the other chapter. Here, it becomes to use two different trajectories, spiral and Cartesian, in one pulse sequence. A fast B_1^+ mapping and correction technique is proposed using spiral readout in the modified transited-state signal in balanced steady-state free precession (bSSFP) imaging. This technique is analyzed using Bloch simulation. Phantom and invivo experiment results are presented and the potential applications are discussed.

Finally, in chapter 6, I will summarize the key issues and present some future potential applications and/or extensions of the works presented in this dissertation.



Chapter 2

MRI Basics and Background Knowledge

2.1 MRI Basics

In this subchapter 2.1, Bloch equation which governs the interaction between magnetization and external magnetic field and three main components of MRI (static magnetic field, radio frequency field and gradient field) are covered.

2.1.1 Bloch Equation

Nuclear induction phenomenon which is a basis of NMR signal was mathematically explained by Felix Bloch at 1946 (1). Nowadays, the equations based on that paper are referred as Bloch equation in general. Joseph Larmor showed that the external magnetic field \vec{B} creates a torque on magnetization vector \vec{M} and it makes precession of \vec{M} with a specific angular frequency $\omega = \gamma\vec{B}$ called Larmor frequency. With time-varying $\vec{M}(t)$ and $\vec{B}(t)$, they affect each other. Thus, in Bloch equation, the interaction of $\vec{M}(t)$ and $\vec{B}(t)$ is explained with time variable. Bloch equation with relaxation time constants is

$$\frac{d\vec{M}(t)}{dt} = \vec{M}(t) \times \gamma\vec{B}(t) - \frac{(M_z(t) - M_0)\vec{z}}{T_1} - \frac{(M_x(t)\vec{x} + M_y(t)\vec{y})}{T_2} \quad (2.1)$$

, where M_0 , $M_z(t)$, $M_x(t)$ and $M_y(t)$ are the equilibrium, longitudinal, transverse magnetizations of x and y directions and γ , T_1 and T_2 are the gyromagnetic ratio, spin-lattice relaxation time, and spin-spin relaxation time, respectively.

2.1.2 Static Magnetic Field B_0

B_0 is a main magnetic field in MRI. 1.5 tesla (T) and 3T scanners are widely used in clinical sites and even higher field scanners are used in research sites. The most popular method to make this strong magnetic field is to use superconducting solenoidal coil. Using the static B_0 field, the randomly pointing polarization vectors are aligned parallel or antiparallel to B_0 . Therefore, the net magnetization \vec{M} is generated and this vector is a potential MR signal.

Homogeneity of B_0 field is very important because B_0 determines the resonance frequency. If B_0 field is inhomogeneous, numerous artifacts can arise such as spatial distortion, abrupt signal shading, and failures of frequency-dependent techniques. Therefore, the process and techniques for homogenizing the B_0 field called shimming are necessary. There are two categories, passive and active methods. In the passive shimming, the inhomogeneous field at the specific location is compensated by using some pieces of metal which can induce additional magnetic fields by B_0 field (9-11). Otherwise, the active shimming uses coils that produce magnetic field by adjusting injection current (12). This technique is relatively complicated than the passive shimming, however, it is more flexible in adjusting the magnetic field because the amount of injection current and its pattern can be chosen adaptively.

2.1.3 Radiofrequency Field B_1

With external magnetic field B_0 , magnetization is aligned along B_0 direction. However, it does not generate any signal without RF field (B_1). The frequency of RF field should be matched to the Larmor frequency to affects to the longitudinal magnetization. RF field is applied to the perpendicular direction to the B_0 field to tip down the magnetization to

transverse plane. After B_1 is applied, the magnetization rotates at the Larmor frequency in transverse plane. This rotation called precession generates time-varying magnetic flux and consequently it induces time-varying voltage at the receiver coil following the Faraday's Law. This process is the signal generation and reception in MRI.

There are many kinds of RF pulses depending on the spatial/spectral selectivity, the shape of RF envelope, the combination with gradient pulse and so on. Focusing on the aim of B_1 field, excitation, inversion and refocusing can be the basic functions of RF pulse. Excitation process is demonstrated in the previous paragraph. The aim of the excitation pulses is to generate MR signal, thus at least one excitation pulse is required in every MR pulse sequence. Inversion pulse tips the magnetization to the opposite direction of B_0 field. Therefore, the magnetization is weighted by T_1 relaxation depending on inversion time. Refocusing pulses are similar to the inversion pulses except that the refocusing pulse is applied after excitation pulse to generate the spin echo signal by inverting the dephasing direction of spins in the transverse plane.

2.1.4 Gradient Fields and Spatial Encoding

Gradient field is a linearly varying magnetic field with spatially allocated gradient coils. It plays an important role in MR imaging because it can make spatially different magnetic fields to introduce the spatial information to MR signal (13). Furthermore, gradient fields are used in a lot of applications with special patterns of gradient sequence such as saturation, preparation, flow sensing, etc.

Slice selective excitation process is illustrated in Fig. 2.1. The slice selection gradient induces linearly varying frequencies along the slice direction (z). Therefore, the slice

thickness is defined by the bandwidth of the applied RF pulse and the amplitude of slice selection gradient.

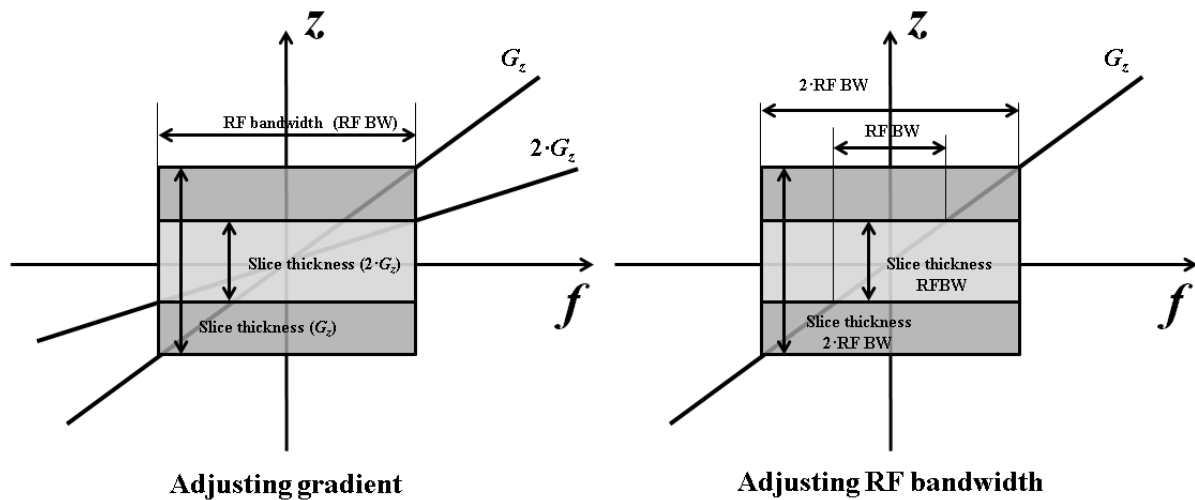


Figure 2.1 Illustrations of slice selection process and thickness control

In general MR imaging, the spatial coordinates of protons are encoded using the frequency and phase information. The phase encoding gradient makes phase differences along phase encoding direction (y) and frequency encoding gradient makes frequency differences along frequency encoding direction (x) during data acquisition. Phase and frequency encodings are analogous to the different starting point and different speed in run race, respectively. Spin diagrams are illustrated in Fig. 2.2 how the spins are affected by the phase and frequency encoding gradients in Fourier-encoding gradient echo pulse sequence. In three-dimensional (3D) imaging, one more phase encoding gradient is applied along the slice direction.

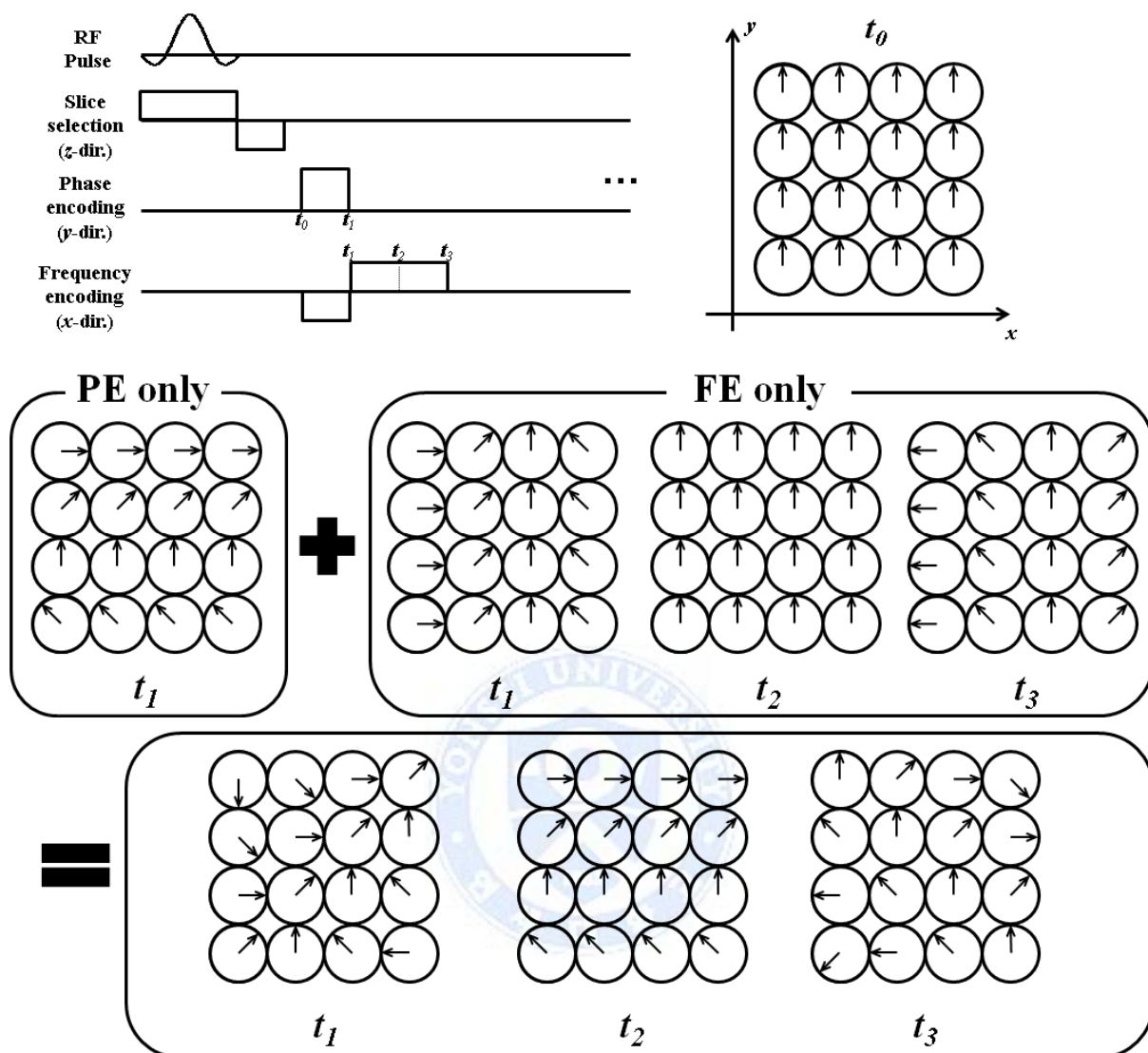


Figure 2.2 Spin diagrams during spatial encoding process

2.2 Fast Imaging Techniques

2.2.1 Imaging Trajectories

The most robust and widely used trajectory is Cartesian trajectory. This type of trajectory uses frequency and phase encodings to fill the rectilinear k-space. In general, one phase encoded line is acquired per excitation with frequency encoding and this acquisition strategy

is called Fourier-acquisition. Intuitively, data acquisition time can be reduced by increasing the number of filling lines per excitation. The acquisition strategy which acquires two or more phase-encoding lines after an excitation is called echo planar imaging (EPI) which is one of the fast imaging trajectories (14). Meanwhile, there are non-Cartesian trajectories such as radial and spiral trajectories which are not confined in rectilinear grid. Non-Cartesian trajectories require gridding process (15) which interpolates data points to rectilinear grid to reconstruct image using Fourier transform. Radial trajectory has motion-robustness because every radial line passes through the center of k-space and that results in an averaging effect while reconstructing MR image. Spiral trajectory can reduce the total data acquisition time since it traverses a lot of k-space points in short time.

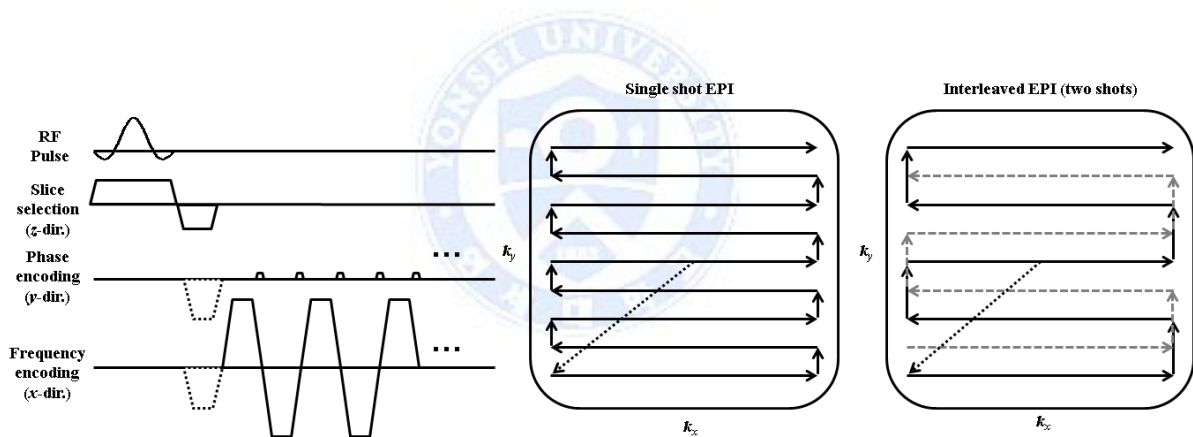


Figure.2.3 EPI pulse sequence and single shot and interleaved trajectories.

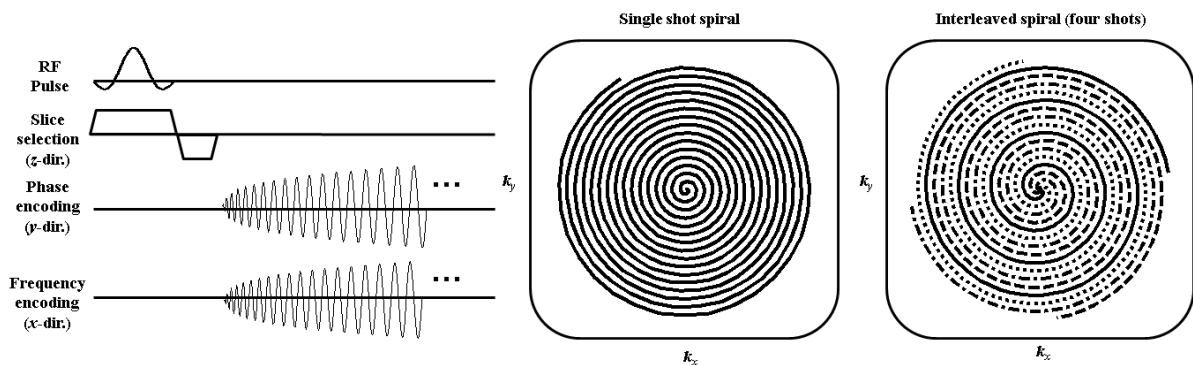


Figure.2.4 Spiral pulse sequence and single shot and interleaved trajectories.

The most important thing in trajectory design is understanding the inverse relationship between image domain and k-space. The data sampling interval Δk is inversely proportional to the FOV, and the maximum data acquisition position k_{\max} is also inversely proportional to the image resolution. Thus, for better resolution while maintaining the FOV, more scan time is required to increase k_{\max} .

The imaging trajectory is defined by the integration of applied gradients during data acquisition.

$$k(t) = \frac{\gamma}{2\pi} \int_0^T G(t) dt \quad (2.2)$$

Various trajectories can be designed to cover k-space by manipulating gradients according to Eq. 2.2.

2.2.2 Parallel Imaging

In the past, signal reception was performed using single-channel receiver coil. However, nowadays, receiver coils that have 128-channel or even more channels are introduced to improve signal to noise ratio (SNR). In addition to SNR gain, multi-channel coils have one more advantage that they have spatial information themselves according to the location and the sensitivity of each coil. Therefore, with multi-channel receiver coil, there is a margin to reduce the spatial encoding time. Generally, reducing the number of spatial encodings can shorten the scan time at the cost of aliasing artifact caused by insufficient samplings to the field of view (FOV) requirements. Thus, the aim of parallel imaging technique is unfolding the aliased image using the spatial information of receiver coils. There are two representative methods in parallel imaging: sensitivity encoding (SENSE) (16) based on coil sensitivity in image domain and generalized autocalibrating partially parallel acquisition (GRAPPA) (17) based on auto-calibration signals (ACS) in k-space. Concept and procedure of SENSE

parallel imaging are presented in Fig.2.5. Using coil sensitivity information, aliased image along PE direction is unfolded after solving inverse problem.

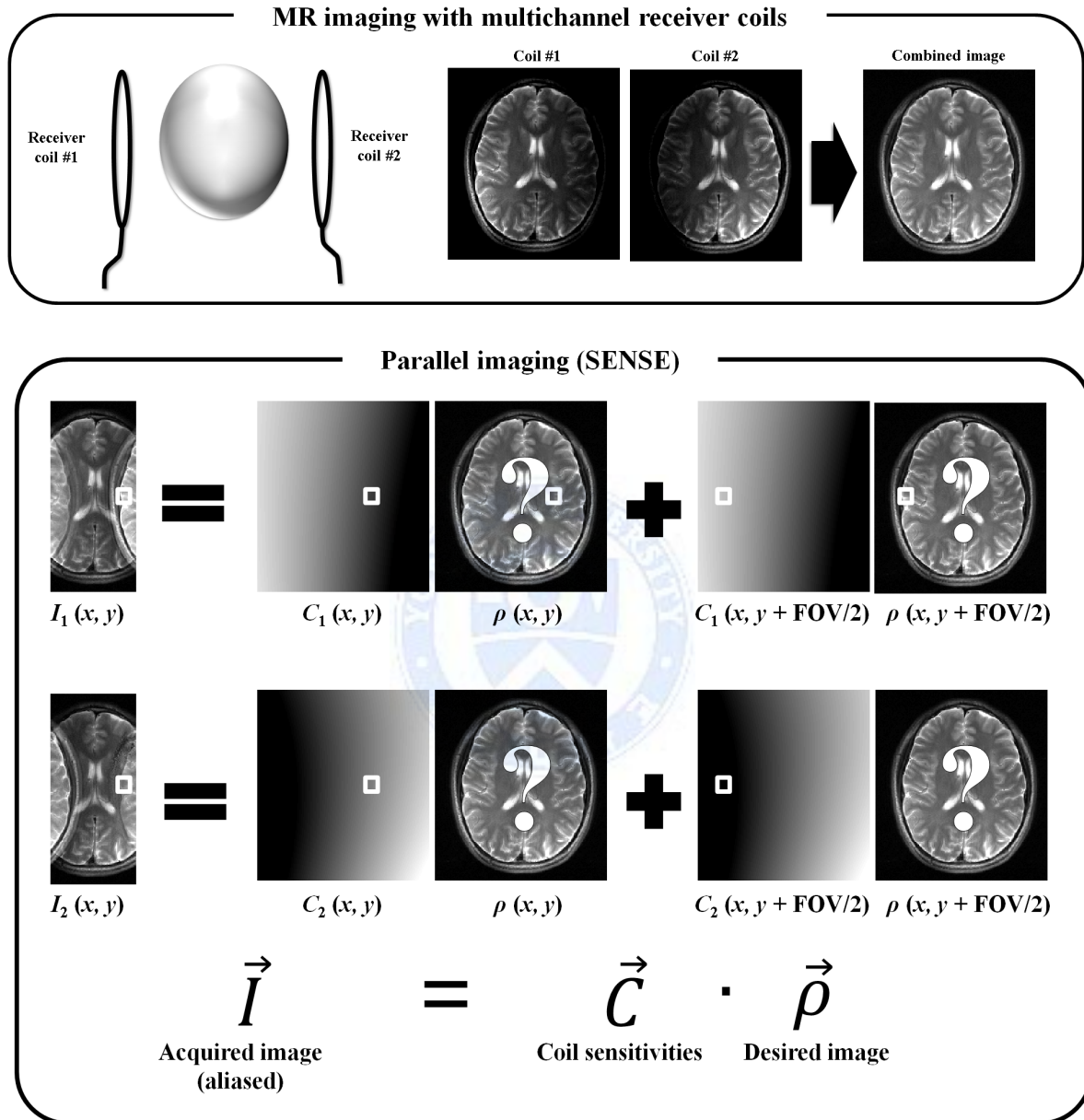


Figure 2.5 Illustrations of SENSE parallel imaging

2.2.3 Simultaneous Multislice Acquisition (SMA) and Wideband Imaging

In multi-slice imaging, total scan time can be effectively optimized by using the idle time from the end of current slice events to the next repetition. For example, if the repetition time (TR) is 300ms and other events for the current slice finished at 20ms, then 15 slices can be acquired with the same acquisition time of single slice acquisition.

Meanwhile, in SMA, multiple slices are simultaneously excited at once with a specially designed multiband RF pulse. Cosine modulation or Hadamard encoding (18) can be used for multiband RF. Simple two-slice excitation pulse using cosine modulation is shown in Fig. 2.6.

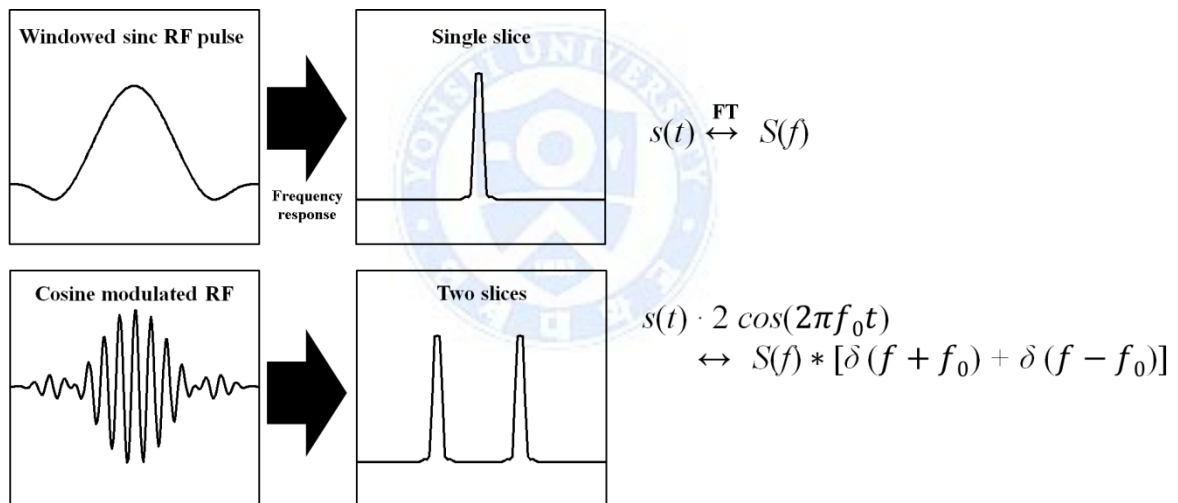


Figure 2.6 RF pulse design for multiband excitation

The excited multiple slices are stacked up and mixed in the reconstructed image using FT only. Therefore, to avoid this aliasing artifact, an additional gradient called separation gradient is applied along slice-select direction during the readout time. Then, the excited slices are shifted along the readout direction and the amount of shift depends on the location of each slice along the slice direction. By increasing the readout FOV (total readout

bandwidth), multiple slices are sequentially displayed along the readout direction at the cost of blurring. This technique is also called wideband imaging (19,20) originated from the widely enlarged total readout bandwidth. The example images are shown in Fig. 2.7. In addition, it often represents 3D imaging that uses the separation gradient because wider band is required for 3D imaging and there is a single wideband case such as non-selective excitation.

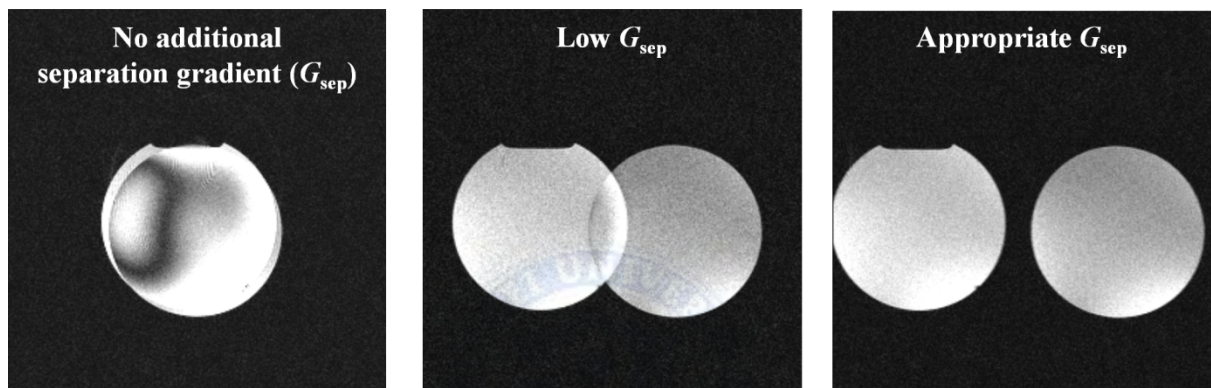


Figure 2.7 Example images of SMA acquisition according to the amplitude of the additional separation gradient.

Otherwise, the aliased multi-slice image can be separated using the coil sensitivity information. One simple method is using a different coil at each slice (21). This technique, however, is not practical because of its condition that each coil does not affect to the others. Another method is using the parallel imaging reconstruction technique along slice direction. However, in some cases, the coil sensitivity along the slice direction varies slowly and it causes ill-conditioning while solving the inverse problem. In order to make the inverse problem easy to solve, each slices are shifted along PE direction by introducing some different phase at each slice by manipulating RF pulse. This technique is called controlled aliasing in parallel imaging results in higher acceleration (CAIPIRINHA) (22) (Fig. 2.8).

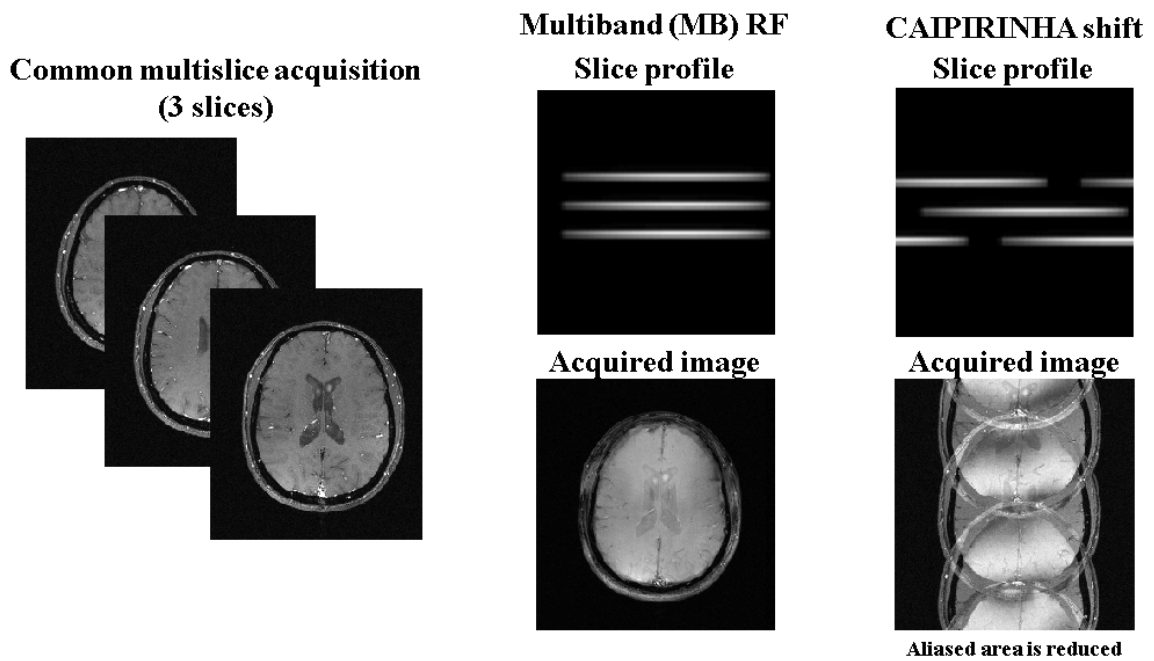


Figure 2.8 Multiband excitation and CAIPIRINHA shift

2.3 Artifacts

2.3.1 Common Artifacts

There exist numerous artifacts in MRI and technical developments have been achieved while overcoming or utilizing the artifacts. Most commonly observed artifacts are B_0 inhomogeneity, B_1 inhomogeneity, eddy-current, chemical shift, aliasing, motion (flow) artifacts and so on (23). Understanding the basis of artifacts gives an insight into the physics and a chance to reverse artifact to useful information. The example images of MR artifacts are shown in Fig. 2.9.

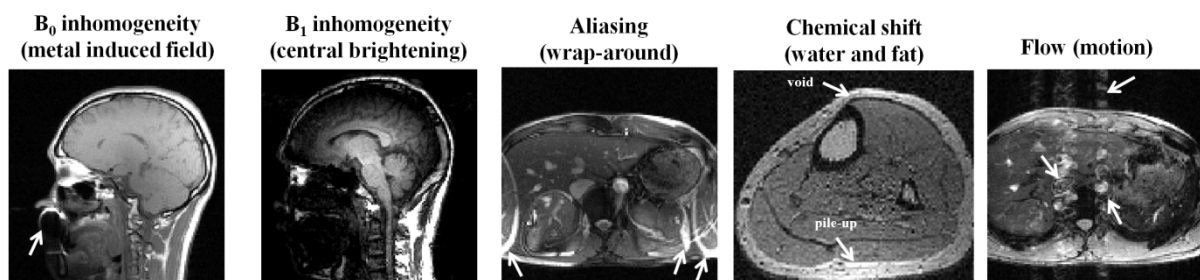


Figure 2.9. Example images of MR artifacts

I will briefly describe about chemical shift, partial volume, B_1^+ (transmit field) artifacts which will be covered in detail later in this dissertation.

2.3.2 Chemical Shift Artifact and View Angle Tilting

Chemical shift artifacts arise from the small difference in resonant frequency because of different molecular environments of nuclei. This artifact is usually observed at fat tissue because ^1H protons in fat are surrounded by electron clouds which can partially shield the external magnetic field. Therefore, fat resonates at slightly lower frequency than water about 440 Hz at 3.0T. In common MR imaging situation, frequency term is assigned spatially using gradient pulses for selective excitation and readout process. If the system frequency is adjusted to water, the spatial coordinate of fat is mis-assigned during frequency encoding process since the resonant frequency of fat is lower than that of water. Consequently, in the final reconstructed image, the location of fat proton is mapped to lower part of the readout gradient field. Due to the spatial shift of fat protons, the fat signal is piled up or canceled with water signal along one frequency encoding direction depending on the echo time (in-phase or out-of-phase, respectively). Along the opposite direction, the fat signal is voided. The important thing to remember is that the chemical shift artifacts occur not only in water-fat situation, but also at the interface of any substances which have different chemical shifts. The amount of pixel shift depends on the readout bandwidth per pixel which can be computed in advance based on the receiver bandwidth and the size of the frequency encoding matrix. If the readout bandwidth per pixel is 210Hz, then the chemical shift of fat tissue is $420 \text{ Hz} / 210 \text{ Hz/pixel} = 2 \text{ pixels}$. Thus, narrow bandwidth should be avoided in general to prevent mixing up at the important interfaces such as cartilage, spines, optic nerve, etc.

There are several methods to alleviate chemical shift artifacts. The most effective method is increasing the readout bandwidth per pixel as described before. Above this, magnetization

preparation can eliminate the chemical shift artifact by saturating the signal from the artifact source using spectral selective RF pulse (24). However, its performance is spatially varying because, in the most cases, the spectral selective RF pulse is sensitive to B_0 field inhomogeneity. Besides this method, water- and fat-only images can be acquired using the in- and out-of-phase characteristics by adjusting the echo time (TE) according to the resonance frequency difference (25).

Total inhomogeneity artifact correction was introduced at 1988 (26). In the proposed pulse sequence named “view angle tilting” (VAT), an additional compensation gradient is applied with the same amplitude of slice selection gradient during the readout time. With this pulse sequence, chemical shift artifacts are shifted back and other in-plane distortions such as susceptibility artifacts are also corrected; signal pile-up and void is resolved and filled at the cost of little blurring in the resultant image. The example image of VAT and chemical shift correction process are shown in Fig. 2. 11. Since this dissertation is focused on the application of additional gradients, VAT technique and its modification will be covered in detail.

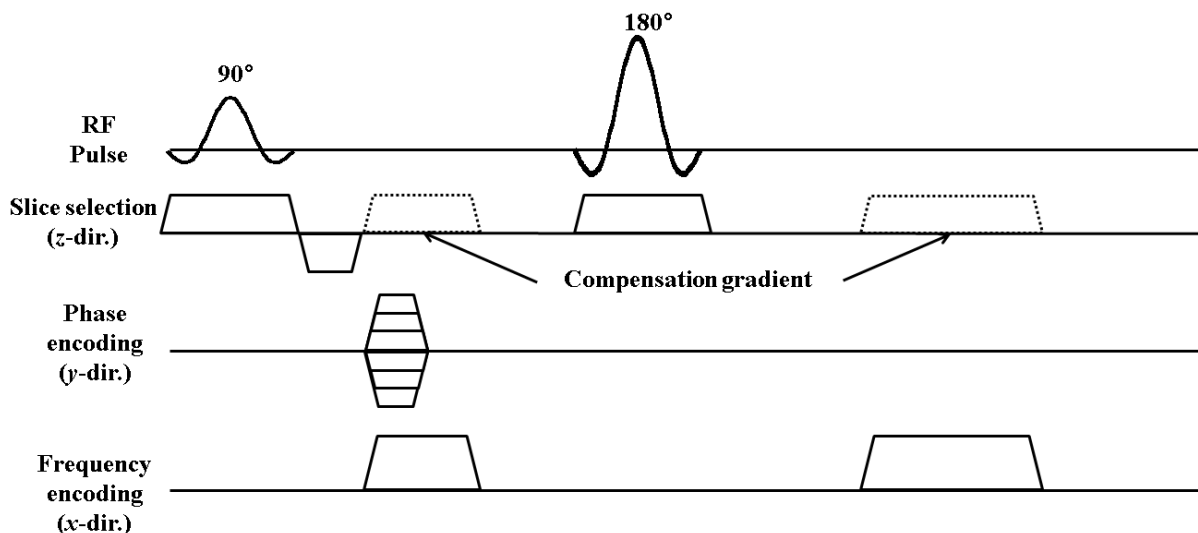


Figure 2.10 VAT pulse sequence diagram

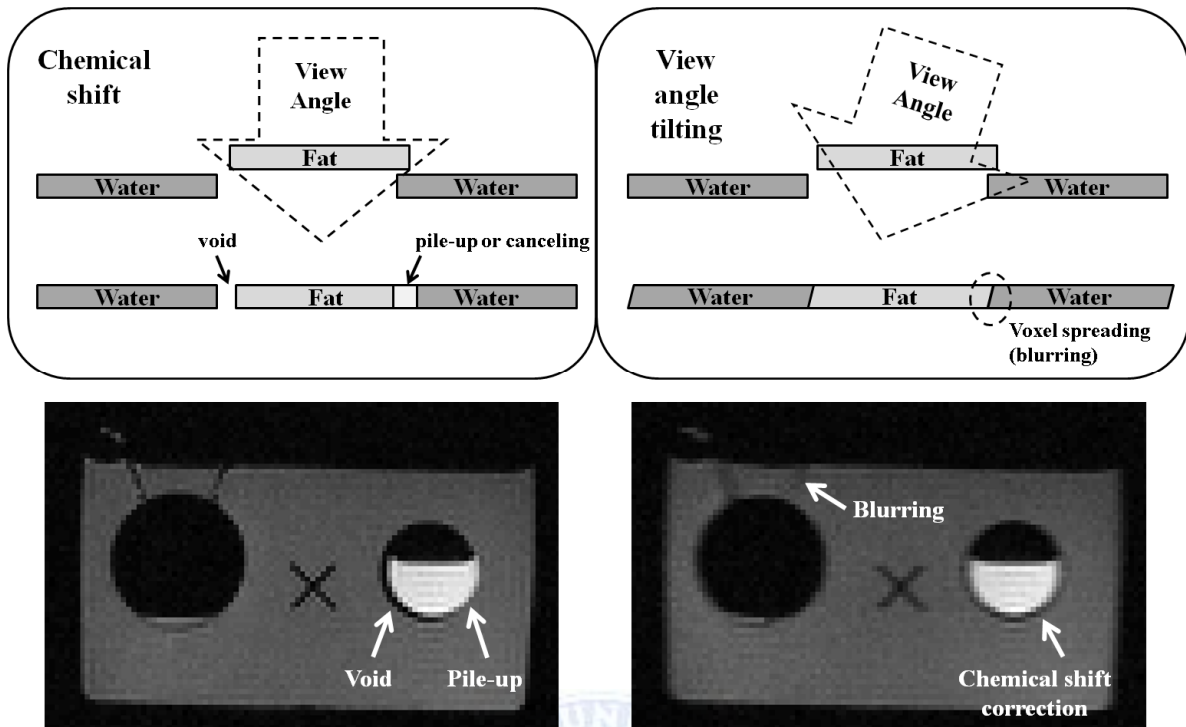


Figure 2.11 Illustrations of VAT principle and example images

2.3.3 Partial Volume Effect

In MRI, cubical voxels are used to measure and express the anatomical images. However, human body is not in rectangular shape like bricks, thus different tissue signals are mixed up at the curved interface and rounded boundaries. Basically, partial volume effect comes from the lack of spatial resolution. This phenomenon can affect the accuracy of diagnosis because it makes the small lesion vague due to the surrounding tissues. The partial volume can be reduced by increasing spatial resolution according to the shape of the subject or the region-of-interest (ROI). For high resolution imaging, the data acquisition time increases and SNR decreases in general.

2.3.4 B₁ Inhomogeneity Artifact

RF pulses are applied repeatedly to excite spins and generate MR signal. Without any subject, transmit field is uniformly distributed. On the other hand, with the dielectric material like human body, the electromagnetic waves experience several phenomena called dielectric effect such as reflection, refraction, wavelength change, interference (27,28). Because of these factors, B₁ field distributes non-uniformly and causes the intensity modulation in the acquired image. This artifact is one of obstacles in quantification studies (29-31).

B₁ inhomogeneity can be partially describe by the standing wave interference which depends on the size of imaging subject and the RF wavelength determined by the B₀ field strength. At 1.5T, the RF wavelength is about 52cm which is relatively long compared to the size of human body, thus B₁ inhomogeneity is hardly observed. However, at 3.0T, the wavelength is shortened to 26 cm which can be the same or smaller than the imaging region. In general, constructive and destructive interferences of standing wave make bright and dark areas respectively. In addition to RF wavelength, electrical and magnetic properties of imaging tissue such as magnetic permeability, conductivity and permittivity can affect the spatial distribution of B₁ field. Considering this factor reversely, if B₁ distribution information is acquired, then the electrical properties of tissue can be estimated based on Maxwell equation. This technique is called MR electric property tomography (7).

B₁ inhomogeneity artifact can be compensated by mapping the spatial distribution of B₁. A lot of B₁ mapping techniques have been introduced (27,28,32-35). One representative technique is double angle method (DAM) which uses two spin echo images acquired with $\alpha-180^\circ$ and $2\alpha-180^\circ$. Image intensity modulations can simply corrected by demodulating the applied B₁ field. Based on DAM, fast transmit field mapping technique inserting additional spiral gradients during transient-state in bSSFP will be introduced in this dissertation.

Chapter 3

Multi- and Wide band imaging for fast data acquisition

3.1 Introduction

Reducing data acquisition time is important for clinicians and patients as well as researchers. Therefore, various methods for reducing data acquisition time have been proposed and widely studied. Data acquisition time can be reduced directly by using fast k-space sampling trajectory(36,37), partial k-space sampling(38) or undersampling(39) which typically results in aliasing artifacts. Many techniques have been proposed for resolving or separating this aliasing artifact as in parallel imaging techniques using multi-channel receiver coil(39-41). Time efficiency can be improved in multi-slice imaging by using a slice interleaved acquisition. In addition, simultaneous multi-slice data acquisitions were introduced, which collect signals from separately excited regions by increasing data bandwidth(42,43), controlling aliasing(44), multi-coil arrays(45), or stepped B_0 field method(46).

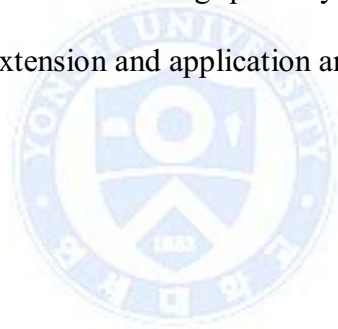
Among these techniques, simultaneous multi-slice acquisition (SMA)(42) uses cosine-modulated RF pulse to excite multiple slices simultaneously and separates the excited slices by applying an additional gradient along the slice direction during the readout (RO) time. This concept has been successfully combined with parallel imaging technique(47,48) and was analyzed in a telecommunication perspective in wideband MRI(49). Acceleration in wideband MRI is accomplished by extending the signal bandwidth during excitation as well as acquisition. In other words, simultaneously excited multiple slices by multiband RF are separated in the frequency domain by an additional gradient and this separated signal is

acquired by enlarging the total RO bandwidth. These methods achieved through-plane acceleration. However, the additional slice-selection gradient causes voxel shearing which results in blurring as trade-off. From a k-space perspective, this blurring comes from a sinc modulation to the acquired signal. This sinc function depends on the excitation slice profile and the applied additional gradient (49,50). A sinc demodulation can be applied to correct this blurring at the cost of noise amplification as in VAT technique (51,52).

Meanwhile, the simultaneously excited slices can be shifted along PE direction by modifying the phase of the applied multiband RF pulse. With this approach called CAIPIRINHA, the aliased regions can be reduced and consequently the number of unfolding problems is reduced as well. In addition, slice-wise shifts make the sensitivity of each coil more independent. While solving the slice-parallel imaging, therefore, its inverse problem is conditioned well.

In this chapter, two methods are introduced. First, focusing on through-plane acceleration, slice-CAIPIRINHA and VAT techniques are merged. By applying the compensation gradient of VAT, field inhomogeneity corrected and accelerated multi-slice acquisition can be achieved. Furthermore, both PE and RO directional shifts make the inverse problem easy to solve. In addition, the inevitable blurring from the compensation gradient is addressed by deblurring techniques, constrained least square filter, used in digital image processing (53). The techniques are based on deconvolution process using point spread function (PSF) of imaging system. Experiments were performed on three phantoms and *in vivo*. The phantoms are water-fat and air-tissue models which can show the capability of chemical shift and B_0 artifacts correction. In addition, *in vivo* experiment was also performed. Deblurring techniques were applied to acquired images. Future extensions and applications are also discussed.

Second, the wideband approach is extended to accelerating single slice 2D imaging and merged with 3D imaging acceleration along both in-plane and through-plane PE directions. In contrast to the previous studies, the proposed method does not require special RF pulses for multi-slice/slab excitation using cosine modulation. In addition, further acceleration can be accomplished by combining parallel imaging technique. The patterns of the anisotropic resolution are described resulting from the voxel shearing that occurs due to the additional gradients (aliasing separation gradients), which were discussed in previous studies (42,47,49). The analyses of this characteristic in image domain and k-space are provided. Experiments were performed with the proposed method on a grid phantom to show the pattern of the anisotropic resolution and in vivo subjects to demonstrate the acceleration capability and the compatibility with generalized auto calibrating partially parallel acquisition (GRAPPA) technique (41). Future potential extension and application are also discussed.



3.2 CAIPIRINHA and VAT for Multiband Excitation and Bidirectional Slice Shifts (CAIPIVAT)

3.2.1 Multiband RF and CAIPI shift

Cosine modulated RF pulse is designed based on Shinnar-Le Roux algorithm to excite multiband with better excitation profile. The excitation profile affects to the amount of VAT blurring and it is crucial for deblurring process to define PSF kernel. Cosine function for multiband excitation is defined according to the distance between desired slices (d_{slice}) as $\cos(w \cdot t \cdot d_{\text{slice}})$ where w is frequency and t is time. The number of simultaneously excited slices can be increased by cosine modulation repeatedly. However, the number of simultaneously excited slices is limited by peak power of RF because it increases proportional to the number of slices in simple multi-band RF design scheme. Thus, advanced multi-band RF design is required to reduce peak power (54,55). CAIPIRINHA technique makes each excited slice shift along PE direction by inducing linear phase using different RF phase at each slice. The phase term of each band are varied according to the number of bands and the amount of shift. Then the coil sensitivity of each slice is virtually shifted and it makes easy to solve parallel imaging problem. In other words, ill-conditioned unaliasing problems due to similar coil sensitivities of excited slices are conditioned well by retaining the independency (reducing the similarity) of coil sensitivity using CAIPI shift. In addition, aliased portions which need to be resolved are reduced as well.

3.2.2 VAT shift

This multiband scheme is combined with VAT technique. VAT can correct in-plane field inhomogeneity artifacts by introducing slice-selection gradient at readout timing, namely, compensation gradient. This VAT gradient can be regarded as separation gradient in SMA. The amplitude of compensation gradient is determined by the amplitude of slice selection

gradient. View angle is defined by the amplitude ratio between the applied compensation gradient and the readout gradient. However, it has one drawback called blurring or voxel spreading. In this study, the blurring artifact is addressed by k-space demodulation using slice profile information.

By combining these two techniques, CAIPIVAT, each slice shifts along RO and PE directions depending on its position along the slice direction (Fig. 3.1). This characteristic can increase the reconstruction performance because the aliased regions are reduced further and the coil sensitivity of each slice retains more independency again. In addition, in-plane field inhomogeneity artifact can be mitigated by VAT.

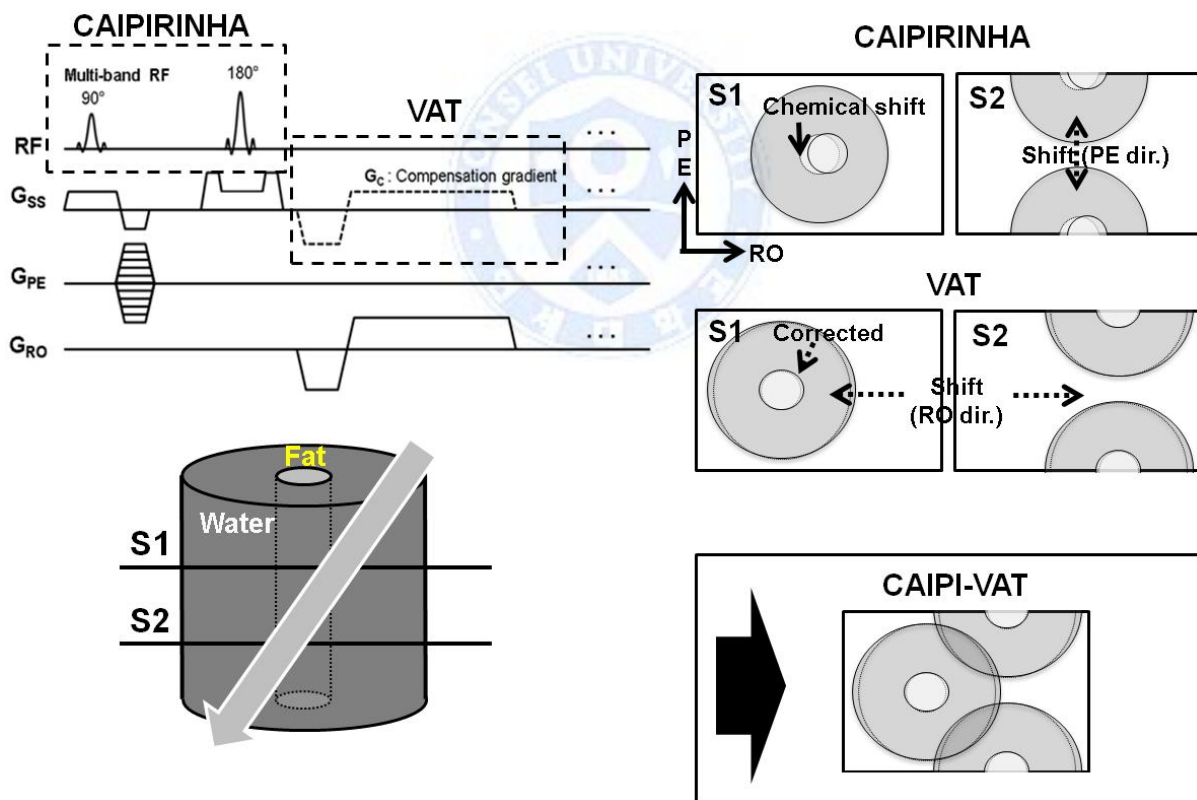


Figure 3.1 Pulse sequence diagram and illustrations of slice shifts in CAIPIVAT. Shifts along PE and RO directions are achieved by CAIPIRINHA and VAT respectively.

3.3 CAIPIVAT Experiments

Three slices with 9.0 mm gap are simultaneously excited and $\pm\text{FOV}/3$ shift are induced by RF phase variation at each TR. All experiments are performed on a 3T scanner (Tim Trio, Siemens Medical Solutions, Erlangen, Germany). The imaging parameters are TR/TE = 650.0/12.0ms, resolution = $1.0 \times 1.0 \text{ mm}^2$, slice thickness = 2.0 mm and readout bandwidth = 390 Hz/pixel and the view angle is 63.1° . Phantom experiments are performed to compare the acceleration performance between CAPI and CAIPIVAT and to show the compensation of field inhomogeneity artifact. In addition, *in vivo* head experiments are also performed on healthy volunteer to show chemical-shift artifact robustness as well as acceleration. Each data is reconstructed using slice-GRAPPA technique which resolves the aliased slices by calculating GRAPPA kernel of each slice with reference image information.

3.3.1 Performance Evaluation with Simulation

SNR performances of two-slice VAT, CAIPIRINHA and CAIPIVAT are tested in simulation (Fig.3.2). The receiver coil sensitivities are assumed that varies less than 10% for 50mm along slice direction. View angle is set to 60° and VAT blurring is not considered. SNR is calculated based on g-factor equation (56). ‘No shift’ shows very poor reconstruction performance due to the similar coil sensitivity along slice direction. Likewise, CAIPIRINHA apparently does not display much advantage over slice distances. CAIPIRINHA and CAIPIVAT start at almost the same SNR because the VAT shift is near zero at the beginning. However, as the distance between slices increase, the SNR of CAIPIVAT increases as well. The SNR of VAT overtakes the SNR of CAIPIRINHA after 23mm point. Furthermore, after 40mm, aliasing can be avoided using VAT-only. According to the simulation result,

CAIPIVAT shows better SNR performance due to the reduced the number of problems to solve and increment in independency of coil sensitivity.

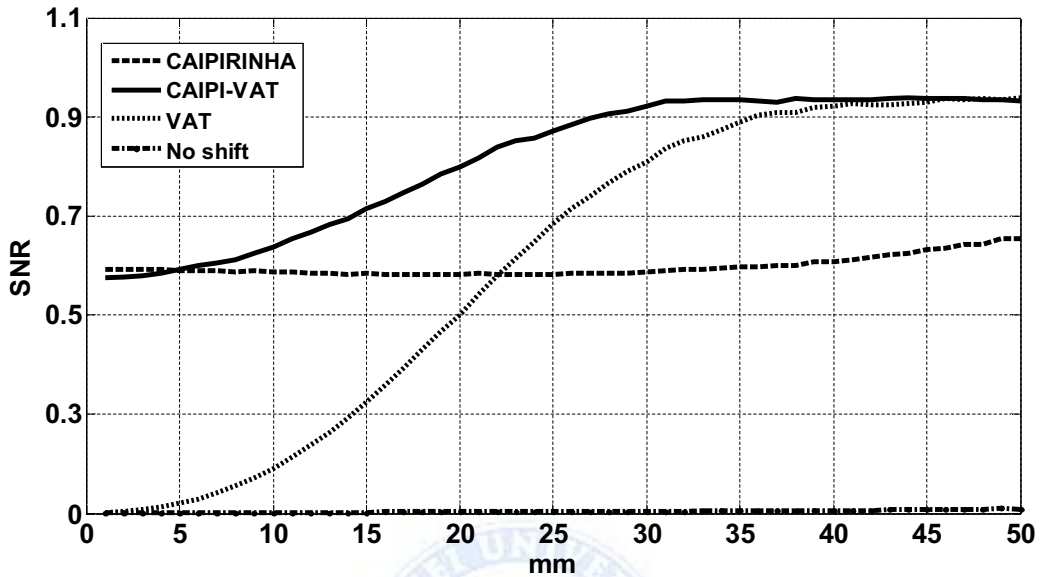


Figure 3.2 SNR simulation of two-slice imaging case. The SNRs of no-shift, VAT, CAIPIRINHA and CAIPIVAT along the slice distance are shown.

3.3.2 Phantom and in vivo Head Experiment

Using water-fat-air model phantom, field inhomogeneity artifact which appeared as slight signal pile up at the air-water interface and chemical shift artifact due to oil are corrected in CAIPIVAT acquisition as shown in Fig. 3.3. Furthermore, comparing the acquired images with CAIPI and CAIPIVAT, the aliased regions are significantly reduced in CAIPIVAT, and consequently, this property makes the unfolding problems easy to solve.

In in vivo imaging, the chemical shifts due to fatty tissue around skull are corrected in CAIPI-VAT and it shows less parallel imaging artifact. VAT blurrings due to additional slice-selection gradient are reduced using simple k-space demodulation technique.

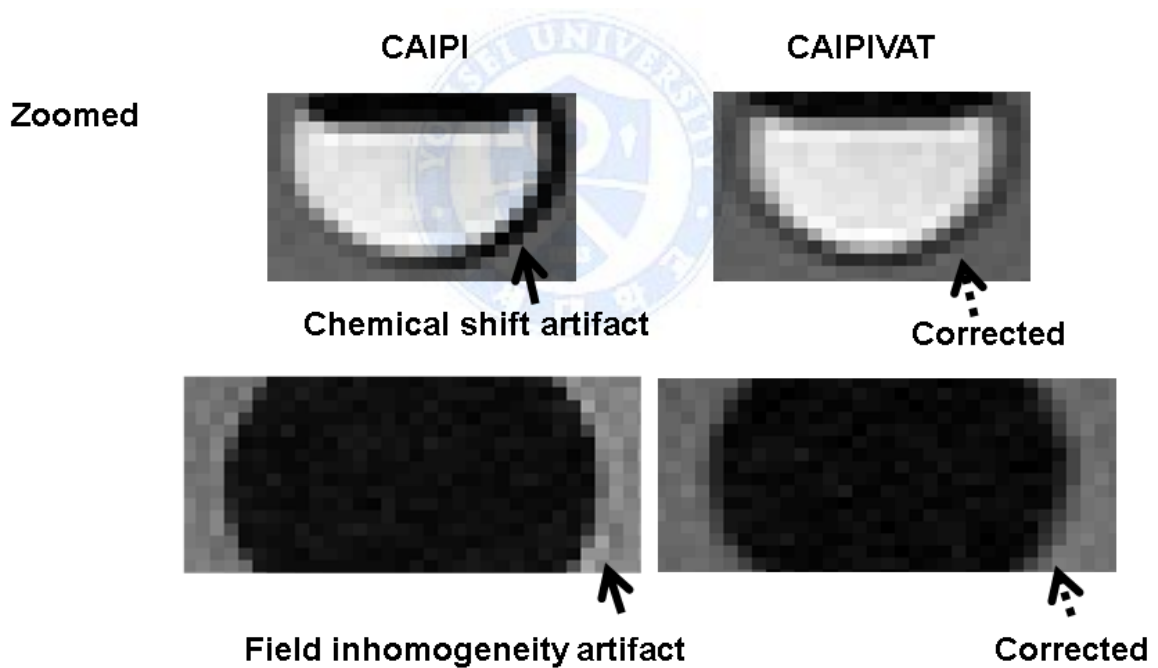
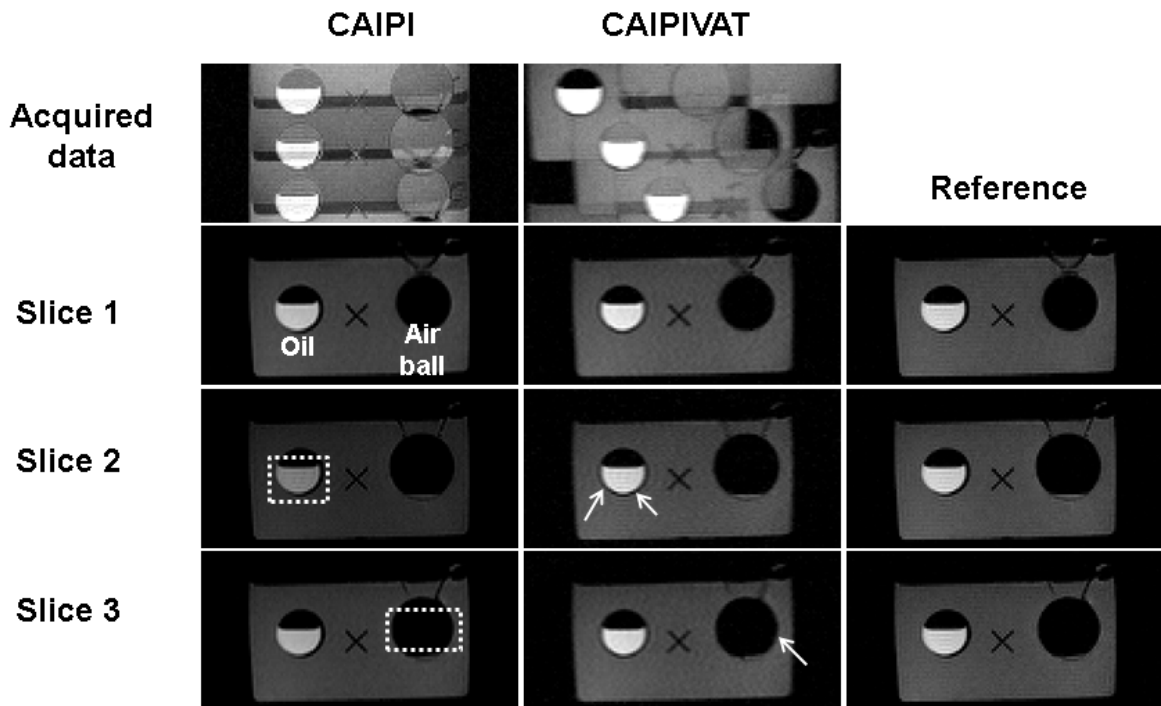


Figure 3.3 Water-fat-air model phantom experiment results using CAIPI and CAIPIRINHA. Standard SE images are shown in third column for reference. Chemical shift artifact from oil and field inhomogeneity artifact from air-tissue interface are alleviated using CAIPIVAT.

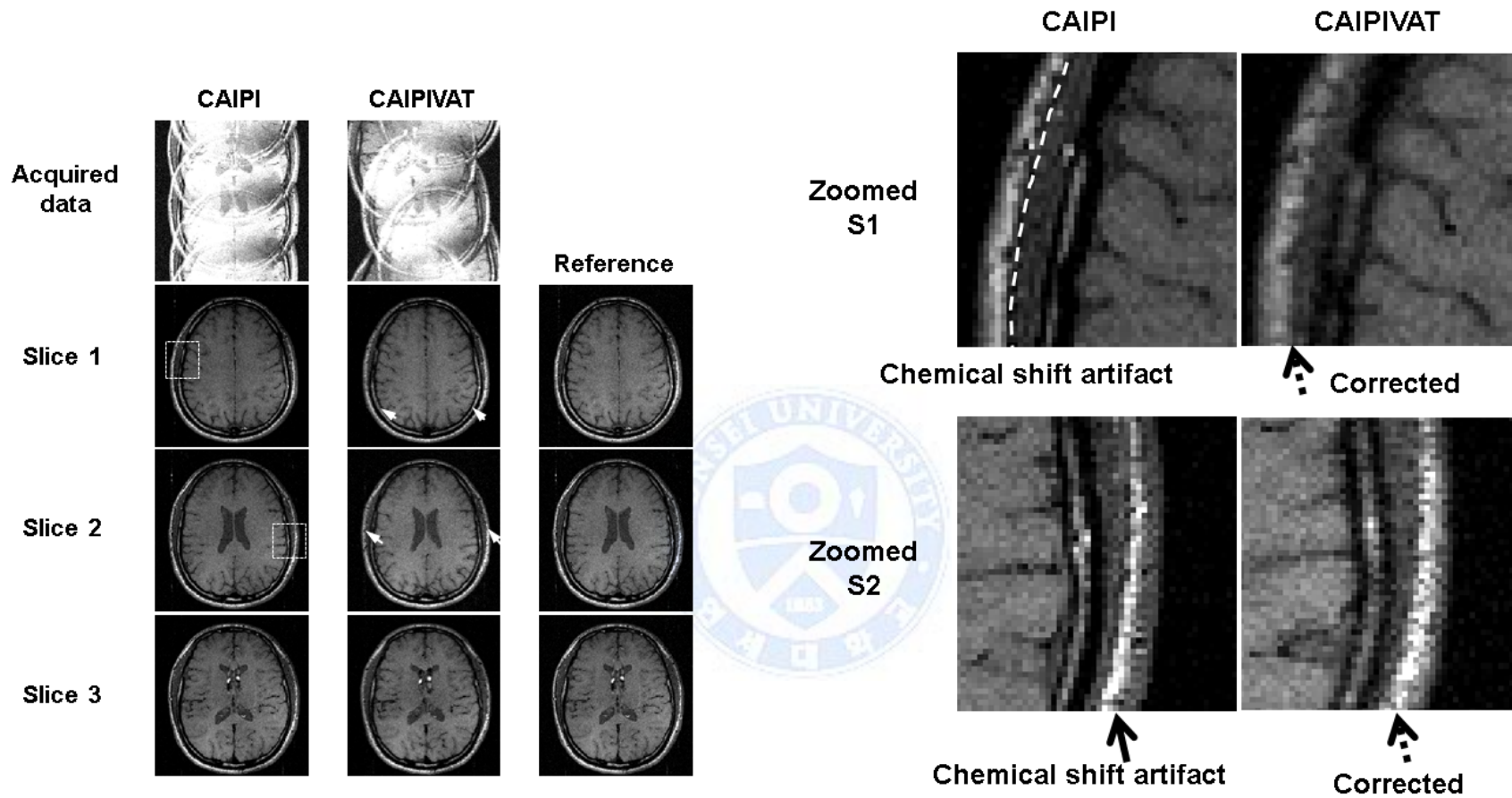


Figure 3.4 In vivo brain experiment results using CAIPI and CAIPIRINHA. Standard SE images are shown in third column for reference.

Chemical shift artifacts at skull bone and scalp are alleviated using CAIPIVAT. In zoomed slice 1, signal void due to chemical shift is indicated by dotted white line and its corrected version is indicated by dotted black arrow.

3.4 Wideband imaging with Aliasing Separation Gradients

3.4.1 Pulse Sequence for 2D and 3D Wideband Imaging

An aliasing separation gradient is applied during the readout time (Fig. 3.5). The separation gradient can be applied to any Cartesian sampling sequences without altering the contrast mechanisms and the echo formulation strategies. Here, the conventional gradient echo (GRE) pulse sequence is simply modified. Aliasing artifacts resulting from undersampling in PEs can be separated to RO direction by applying $G_{PE_{sep}}$ and/or $G_{SS_{sep}}$ along the undersampled direction. The concept of aliasing separation is illustrated in Fig. 3.5(c, d).

For 2D imaging acceleration, the aliasing separation distance, d_{sep} , can be defined as

$$d_{sep} = \frac{G_{PE_{sep}}}{G_{RO}} \cdot FOV_{G_{PE}}, \quad (3.1)$$

where $FOV_{G_{PE}}$ is the field-of-view along G_{PE} direction. Assuming that the longest length of the imaging object along RO direction is l_{max} , then l_{max} can be considered as the minimum separation distance required for an alias-free image (i.e., $d_{sep, min} = l_{max}$). In this case, the required separation gradient is

$$G_{PE_{sep}} \geq \frac{l_{max}}{FOV_{G_{PE}}} \cdot G_{RO}. \quad (3.2)$$

According to Eq. (3.2), larger $G_{PE_{sep}}$ is needed to achieve higher acceleration (small $FOV_{G_{PE}}$). To accelerate in both PE directions for alias-free 3D image [Fig. 3.5(b)], the required separation gradient along slice selection (SS) direction is

$$G_{SS_{sep}} \geq \frac{l'_{max}}{FOV_{G_{SS}}} \cdot G_{RO}. \quad (3.3)$$

Here, l'_{max} is equal to $R_{PE} \cdot l_{max}$ since the longest length of the imaging object along RO

direction is redefined due to in-plane acceleration by PE reduction factor R_{PE} [Fig. 3.5(d)]. Consequently, a proportionally larger $G_{SS,sep}$ compared to $G_{PE,sep}$ is required for acceleration in two directions in 3D imaging.

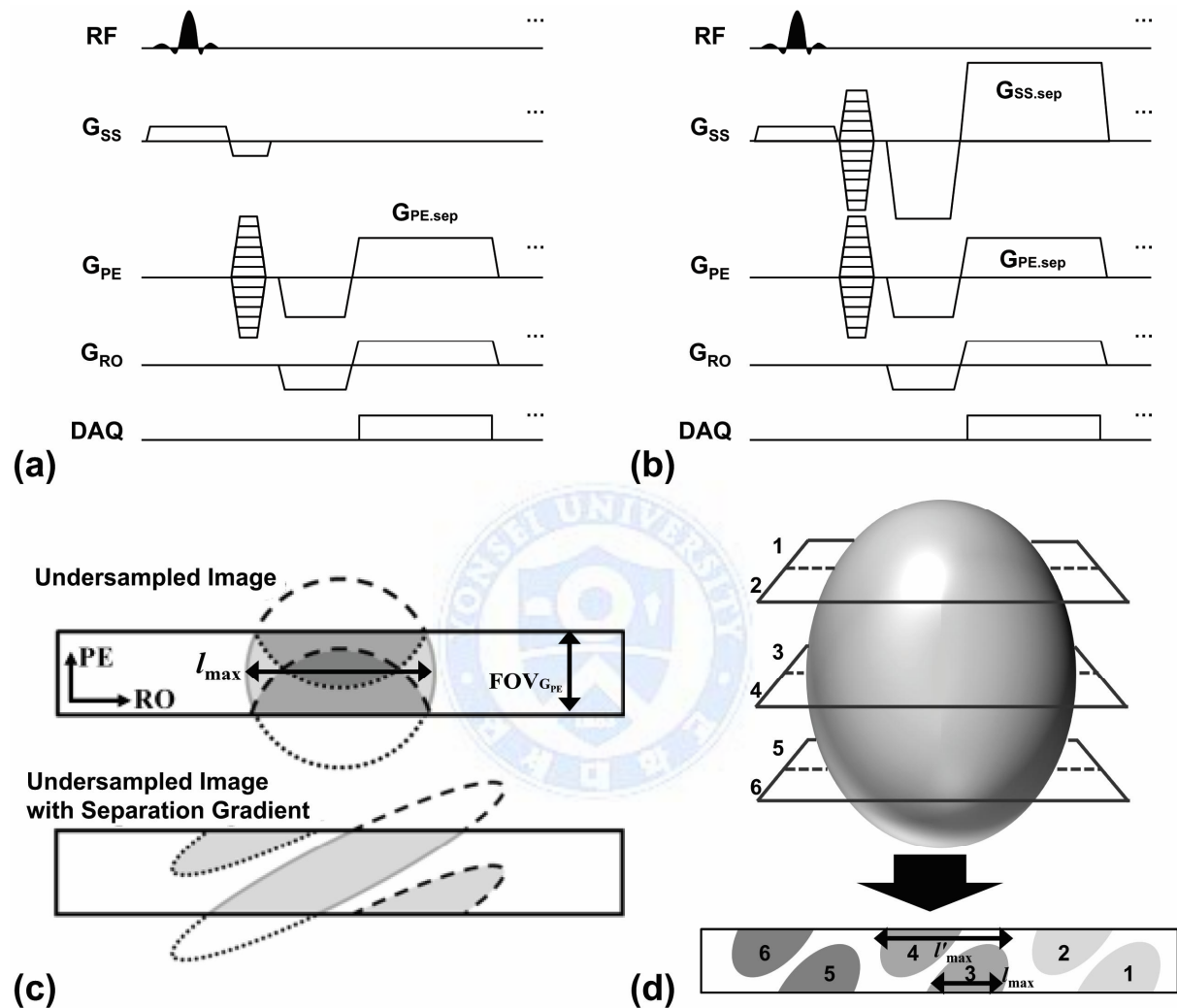


Figure 3.5 Pulse sequence diagram for (a) 2D and (b) 3D imaging with aliasing separation gradients. The separation gradients, $G_{PE,sep}$ and/or $G_{SS,sep}$ (dashed lobes), are simultaneously applied during data acquisition. Undersampling of the phase encode gradients are represented by dotted line. The phase-encoding gradient and the pre-phasing gradient in G_{PE} and G_{SS} can be merged to decrease the minimum echo time if necessary. The concept of acceleration and aliasing separation for (c) 2D and (d) 3D imaging are illustrated in the image domain. The required separation distances for alias-free image are noted as l_{max} for 2D and l'_{max} for 3D.

3.4.2 Voxel Shearing in Image Domain (diagonal sampling in k-space)

With the proposed acquisition method, voxel is modified to sheared form as illustrated in Fig. 3.6. The amount of shearing depends on the ratios, 1) $G_{PE_{sep}}$ over G_{RO} and 2) PE resolution over RO resolution. As shown in Fig. 3.6(d), larger gradient ratio for higher acceleration aggravates voxel shearing resulting in increased spread of signals. On the other hand, finer PE resolution compared to RO resolution can reduce the amount of spreading as illustrated in Fig. 3.6(e). In practice, the PE resolution is typically set identical to the RO resolution in 2D imaging. So, reducing the voxel spreading using higher PE resolution than RO resolution might not be appropriate for 2D imaging. However, in 3D imaging where slice-direction PE resolution (slice thickness) higher than RO resolution, the voxel spreading can be reduced by imaging slice thinner than the RO resolution.

In k-space perspective, the effective FOV and resolution are re-defined with respect to the sampling trajectory of the proposed method which samples k-space diagonally in k_x - k_y with slope $G_{PE_{sep}}/G_{RO}$ and/or in k_x - k_z with $G_{SS_{sep}}/G_{RO}$. Considering the acceleration for 2D imaging, sampling occurs along one diagonal direction k_{diag1} with slope $G_{PE_{sep}}/G_{RO}$. This can be represented by,

$$k_{diag1,max} = k_{x,max} \cdot \sqrt{\left(G_{PE_{sep}}/G_{RO}\right)^2 + 1} \quad (3.4)$$

$$\Delta k_{diag1} = \Delta k_x / OS \cdot \sqrt{\left(G_{PE_{sep}}/G_{RO}\right)^2 + 1}, \quad (3.5)$$

where Δk_x is the RO sampling interval for aliasing-free image and OS is the RO oversampling factor. According to Eq. (3.4) and (3.5), the proposed sampling pattern causes an improvement of resolution in k_{diag1} and a reduction of FOV_{diag1} , which should be compensated by increasing OS . On the other hand, along the perpendicular diagonal direction

with slope $-G_{RO}/G_{PE_{sep}}$, k_{diag2} can be represented by

$$k_{diag2,max} = ky_{max} \cdot \left(\sqrt{\left(G_{PE_{sep}}/G_{RO} \right)^2 + 1} \right)^{-1} \quad (3.6)$$

$$\Delta k_{diag2} = \Delta ky \cdot R_{PE} \cdot \left(\sqrt{\left(G_{PE_{sep}}/G_{RO} \right)^2 + 1} \right)^{-1}. \quad (3.7)$$

Here, Δky is the PE sampling interval for aliasing-free image and R_{PE} is the PE reduction factor. According to Eq. (3.6) and (3.7), this sampling pattern causes a loss of resolution along the direction of k_{diag2} and an increase of FOV_{diag2} . This increase, however, is canceled by the PE reduction factor R_{PE} . By maintaining Δk_{diag2} similar to Δky , the aliasing artifacts due to PE undersampling can be avoided. The effective resolution has an anisotropic pattern defined by the gradient ratio G_{sep}/G_{RO} as in Eq. (3.4) and (3.6). These anisotropic diagonal resolutions are noted in Fig. 3.6(d, e). The resolution and FOV characteristics for 3D imaging can be determined by a simple expansion to another PE direction

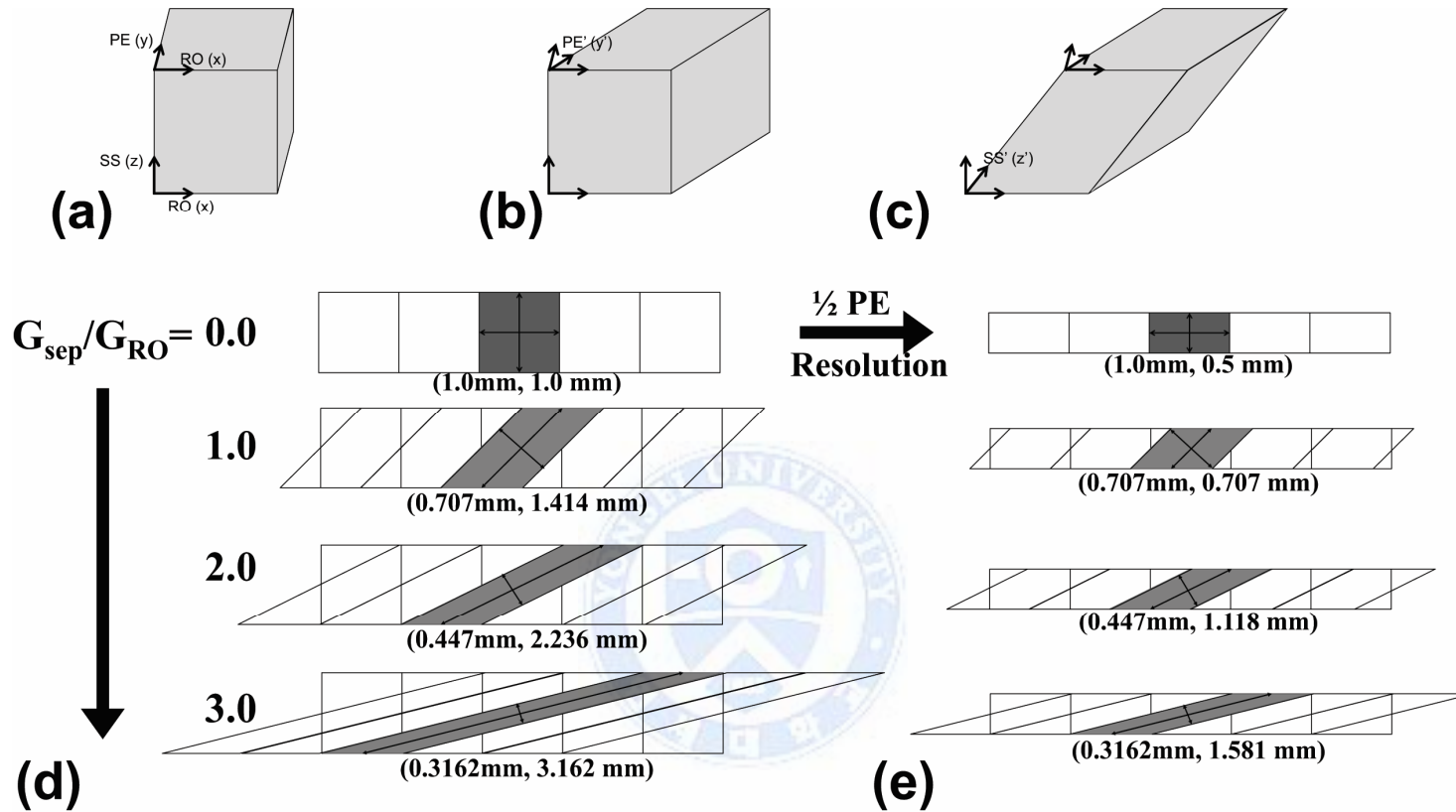


Figure 3.6 Illustrations of voxel shape modification. (a) Normal imaging voxel. (b) Sheared voxel along PE direction due to $G_{PE,sep}$. (c) Sheared voxel along PE and SS directions with $G_{PE,sep}$ and $G_{SS,sep}$ both. (d) Relationship between voxel spreading and the gradient ratio G_{sep}/G_{RO} . The voxel spreading is increased with bigger separation gradient. (e) Voxel spreading when PE resolution is increased by 2. Voxel spreading portion can be reduced by high resolution imaging along PE direction. Note the anisotropic resolutions (diagonal lengths of sheared voxels) are noted in (d) and (e).

3.4.3 Wideband Reconstruction

The acquired data using the proposed method can be reconstructed by two methods, 1) shift and combine method or 2) gridding. For the shift and combine method, the acquired image can be regarded as being shifted along RO direction in the image domain. Here, a shift-corrected image can be obtained by multiplying linear phase in k-space according to the applied separation gradient. After shift correction, the image is divided into $R_{PE} + R_{SS}$ parts and these parts are combined depending on the desired FOV. This shift and combine method is fast, simple and intuitive. However, this process disregards the diagonally sampled k-space regions. With gridding, diagonal k-space sampling can be taken into concern and the high k-space regions can be properly reflected into the reconstructed image. This in turn also corrects for the image shift. The gridding process is fast and simple due to the uniform sampling density of the proposed acquisition method. Therefore, all the results shown in this study are reconstructed by using the conventional gridding algorithm(57).

For further acceleration, parallel imaging technique is combined with the proposed method. GRAPPA sampling is achieved in the proposed method by performing additional undersampling. GRAPPA reconstruction is thus aimed to recover from this additionally undersampled data. Since the proposed method oversamples highly during the readout time to acquire a wideband signal, the GRAPPA kernel should be chosen considering the readout oversampling factor. In image domain perspective, the aliased regions due to GRAPPA undersampling are also separated diagonally. Therefore this results in the reduction of aliased portions which is desirable for parallel imaging reconstruction.

3.5 Wideband Experiments

Experiments were performed on a 3T scanner (Tim Trio, Siemens Medical Solutions, Erlangen, Germany) with a manually designed grid phantom and invivo and an 12-channel

birdcage receiver head coil was used for imaging. For the phantom study, a combination of $G_{PE_{sep}}$ and G_{RO} were tested to illustrate the effect of acceleration and voxel shearing. The scan parameters for the single slice phantom imaging were TR = 30ms, TE = 9.8ms, RO bandwidth/pixel = 390Hz/pixel, resolution = 1.0 x 1.0 mm², slice thickness = 2.0 mm, $G_{PE_{sep}} / G_{RO} = [0, 2, 3, 4, 5, 6]$, $R_{PE} = [0, 2, 3, 4, 5, 6]$, OS = 6, measured data size (RO x PE) = 1536 x [256, 128, 88, 64, 48, 40], final image size = 256 x 256 and total acquisition time = [7.68, 3.84, 1.92, 1.32, 0.96, 0.72, 0.60]s. For comparison, conventional Cartesian sampled images which require the same acquisition time as the proposed method were also acquired. For invivo whole brain imaging, the parameters were TR=30ms, TE=7.8ms, RO bandwidth/pixel = 390Hz/pixel, resolution = 1.0 x 1.0 x 0.5 mm³, $G_{PE_{sep}} / G_{RO}=1.5$, $G_{SS_{sep}} / G_{RO} =3.0$, $R_{total} = 6$ ($R_{PE} = 2$, $R_{SS} = 3$), OS = 6, measured matrix size (RO x PE x Slice) = 1152 x 96 x 192, final matrix size = 192 x 192 x 576 and total acquisition time = 9m 13s. The total acquisition time was reduced to 5m 46s for GRAPPA sampling (GRAPPA factor $R_{GRAPPA}=2$ and 24 ACS lines).

3.5.1 Voxel Shearing in Grid Phantom Experiment

The acquired and reconstructed images of grid phantom are shown with the corresponding k-space data in Fig. 3.7. The undersampling portions and the gradient ratios $G_{PE_{sep}} / G_{RO}$ are noted. The images in Fig. 3.7(b) show the relationship between acceleration and voxel shearing. As expected, higher acceleration causes more voxel shearing. The pattern is anisotropic due to the sheared voxel characteristic as depicted in Fig. 3.7. The grid structure in the phantom image along one diagonal direction is more resistant to blurring than along the other direction. This is because the sampled and empty regions are increased diagonally with respect to the applied separation gradient in k-space. In addition, sensitivity to B0

inhomogeneity increases with the undersampling factor [dotted arrows in Fig. 3.7(b) and (c)]. However, when comparing with the acquisition method of simply reducing the number of PE lines [Fig. 3.7(c)], the overall inhomogeneity effects and ringing artifacts are reduced. This is because of the reduced k-space coverage along k_y in conventional Cartesian sampling. B_0 inhomogeneity artifact occurs when the sampled k-space region does not sufficiently cover the echo shift (Δk) caused by B_0 field inhomogeneity.

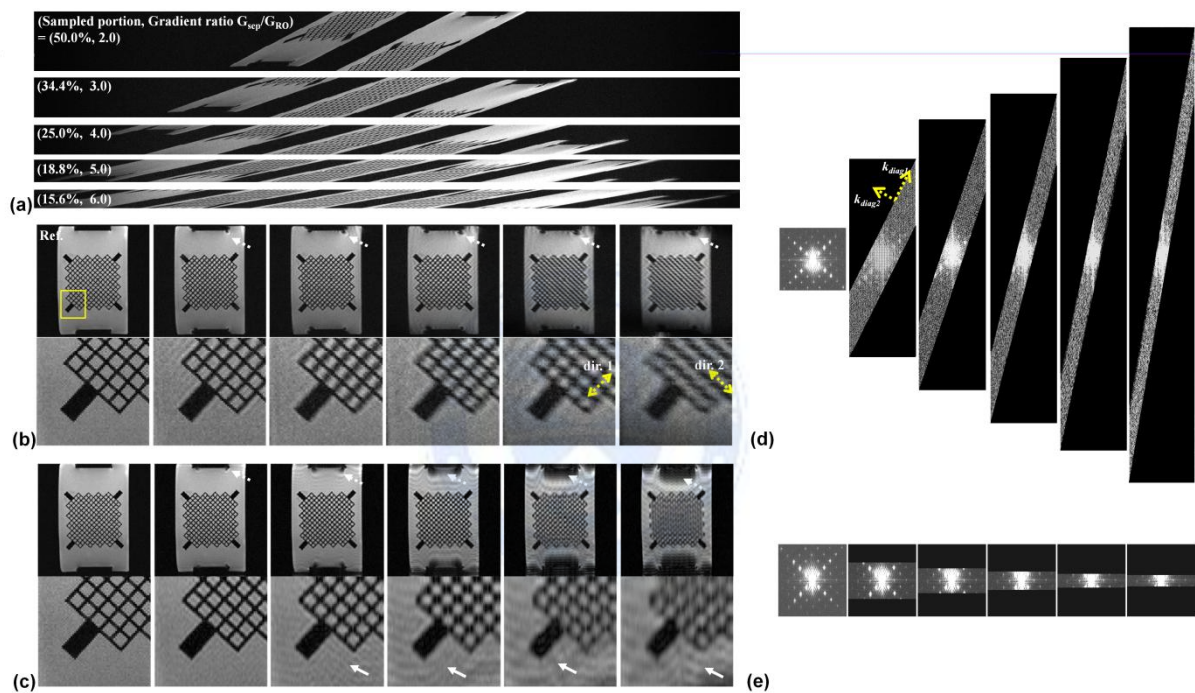


Figure 3.7 Phantom experiment results with different undersampling and gradient ratios ($G_{PE,sep}/G_{RO}$) and acquisition time matched GRE images. (a) Acquired raw image data using the proposed method. (b) Reference image and reconstructed images of (a). (c) GRE images with the same acquisition time as (b). The yellow boxed region is magnified to visualize the anisotropic resolution pattern and ringing artifacts. The grid structure shows directional dependence in (b). Overall ringing (white arrows) and inhomogeneity induced artifacts (white dotted arrows) are more apparent in (c) compared to (b) due to the reduced area coverage of k-space. (d, e) Corresponding k-spaces of (b) and (c), respectively.

3.5.2 Parallel Imaging with GRAPPA Technique

GRAPPA undersampling with factor 2 was further applied to the acquired phantom data (Fig. 3.8). The image at each reconstruction step and the corresponding k-space are shown. The aliasing regions due to GRAPPA undersampling are separated diagonally as indicated by arrow in Fig. 3.8(b) therefore making it easy to resolve the aliasing. GRAPPA undersampled lines are filled properly as shown in the zoomed k-space image. The difference between the images with and without GRAPPA is mostly in the noise level [Fig. 3.8(d)]. This result suggests that parallel imaging technique can be combined to the proposed method to increase the acceleration capability. However, in combining parallel imaging technique, its intrinsic problems (58) such as g-factor dependency and SNR loss are inevitable.

3.5.3 In vivo Head Experiment

The acquired in vivo head images are shown in Fig. 3.9. Figure 3.9(a) shows the two in-plane and three through-plane parts acquired simultaneously (6x acceleration) and separated along RO direction in a single image. The final reconstructed images for the 6x acceleration in Fig. 3.9(b) show little blurring because minimum separation gradients ($G_{PE_{sep}} / G_{RO} = 1.5$ and $G_{SS_{sep}} / G_{RO} = 3.0$) were applied and the slice thickness was half of the RO resolution ($1.0 \times 1.0 \times 0.5 \text{ mm}^3$). Fig. 3.9(c) shows reconstructed image using GRAPPA undersampled data with factor 2 (total 12x acceleration). Decrease in SNR and some residual aliasings are observed when applying GRAPPA technique. The corresponding data acquisition time is reduced from 55m 18sec to 9m 13s using proposed method [Fig. 3.9(b)] and further reduction to 5m 46s with GRAPPA [Fig. 3.9(c)].

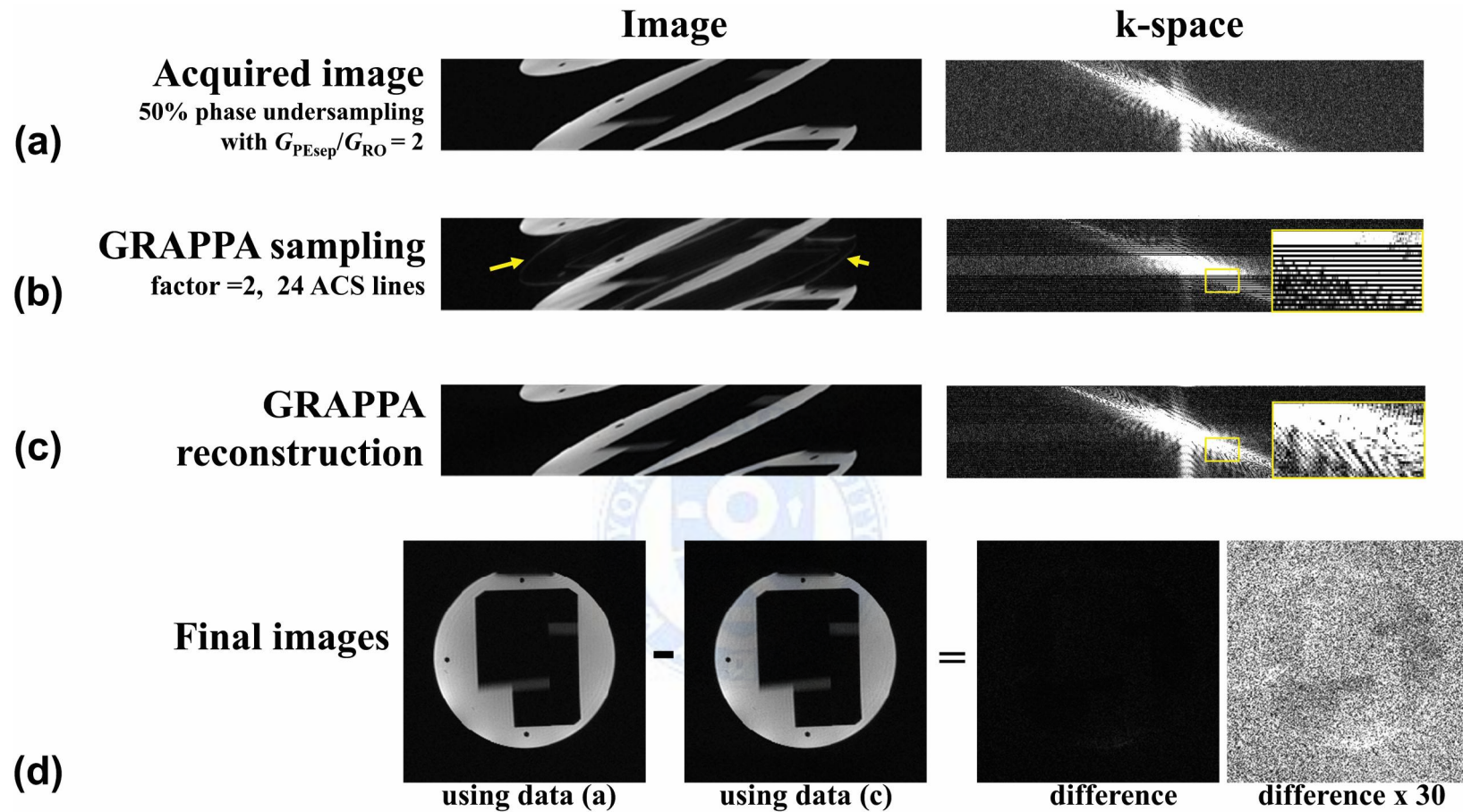


Figure 3.8 (a) Acquired raw image with 50% undersampling using the proposed method. (b) GRAPPA sampled image with additional factor 2 (24 ACS lines). (c) GRAPPA reconstructed image. (d) Final reconstructed images from (a) and (c) and difference image. In k-space image, the yellow boxed regions are magnified to visualize the undersampled lines and their reconstruction results.

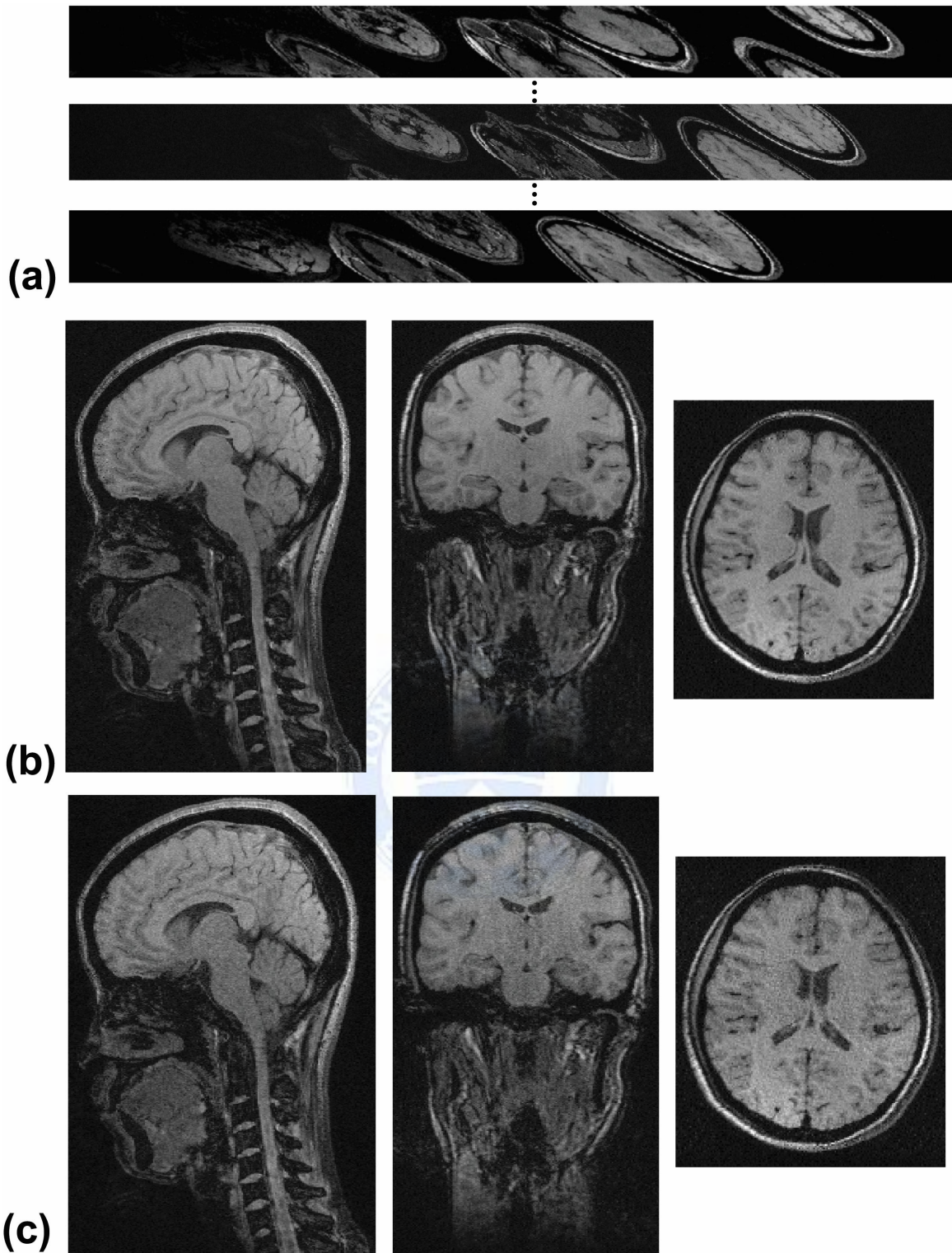


Figure 3.9 In vivo 3D imaging results. (a) Three representative axial images from 192 slices without GRAPPA (6x acceleration, 2X along in-plane PE, 3X along through-plane PE). (b) Sagittal, coronal and axial views of reconstructed images using (a). (c) Reconstructed images with GRAPPA. (12x acceleration with PE undersampling factor 2 and 24 ACS lines)

3.6 Discussions

3.6.1 Multiband imaging

First of all, the number of voxels to solve the unfolding problem is reduced because of the bi-directional shifted image along both PE and RO direction. Furthermore, ill-conditioned problems due to similar coil sensitivity of each slice can be conditioned better by increasing independency of coil sensitivity. Therefore, this feature results in reducing g-factor and gives a chance to increase multi-slice excitation factor. In addition, VAT technique has its own ability of compensating in-plane field inhomogeneity artifacts at the cost of partial volume blurring due to the VAT gradient. This blurring, however, it can be compensated by k-space demodulation with the kernel from slice profile information.

In general, the appropriate number of simultaneous multislice factor depends on the receiver coils, and imaging parameters. In other words, the number of receiver coils, the geometric distribution of their sensitivities, volume coverage and slice gap are important to decide the multiband factor. In this chapter, without CAIPI shifting technique, SNR loss was observed using multiband factor = 3 although 12-channel birdcage receiver coil was used. Since the receiver sensitivity of birdcage head coil varies little along head-foot direction, SNR loss occurred during unfolding process. Therefore, the receiver properties, imaging parameters and shifting technique should be carefully considered when choosing the multiband factor.

In order to increase the number of excitation bands, special technique is required such as variable-rate selective excitation (VERSE)(54) or power independent of number of slices (PINS)(55) because peak RF power increases proportional to the number of slices in simple multi-band RF design scheme. These advanced multiband RF design scheme are essential especially in selective 180° RF pulse in SE based sequences.

In conclusion, by combining CAIPI and VAT techniques, parallel multi-slice imaging with better performance than CAIPI and field inhomogeneity corrected acquisition can be achieved. This combination can be useful for reducing data acquisition time in SEMAC(59) which has been proposed for correcting metal induced artifacts.

3.6.2 Wideband imaging

The SMA technique(42) was originally proposed to acquire multiple slices simultaneously and its concept was further analyzed in wideband MRI(49). The extended wideband imaging which can accelerate along both PE directions is introduced in this chapter. By applying separation gradients along both PE directions in 3D MR imaging, aliasing artifacts caused by PE undersampling has been successfully separated and a 6X acceleration is achieved for whole brain 3D MR imaging with slight blurring due to voxel shearing. Further acceleration was accomplished by combining parallel imaging technique which gave a 12X acceleration. In addition, the GRAPPA kernel applied here can be regarded as an anisotropically shaped kernel due to the diagonally sampled k-space data in the proposed method. This anisotropic GRAPPA kernel can also allow further increase in the undersampling factor compared to the number of receive coils(60).

The proposed wideband method can be simply implemented and applied to gradient echo sequences as well as spin echo based sequences. Furthermore, in contrast to previous publications which have been using multiband RF pulses, the proposed method works for standard 2D and 3D imaging experiments with a simple slab excitation including non-selective excitation RF pulse. Multi-band RF pulses to separate excitation regions may be necessary to combine this method with the CAIPIRINHA (44) approach for further acceleration along the slice direction. However, when using multi-band RF pulse, the RF power increases proportionally with the number of excitation bands, which inevitably

prolongs the RF duration to avoid the RF power or specific-absorption-ratio limitations. In addition, the basic idea is similar to the parallel 2D SENSE or 2D CAIPIRINHA approaches that aim to modify the aliasing pattern in order to achieve a better parallel imaging reconstruction performance. However, the proposed wideband method prevents aliasing and does therefore not suffer from noise amplification in contrast to parallel imaging(61).

The high acceleration capability shown in the experiment results can be useful for volumetric pre-scan imaging to acquire global variations of B_0 or coil sensitivity which need not be high resolution. In addition, the proposed method might be used for increasing the temporal resolution in line tagged cardio-vascular imaging when one considers the anisotropic resolution pattern as shown in the grid phantom results.

Despite the easy implementation and the high acceleration capability, some drawbacks such as maximum gradient limitation, B_0 inhomogeneity effect and voxel modification exist. When G_{sep} with maximum power is not sufficient to achieve the desired separation distance, G_{RO} should be decreased and it increases the minimum TE and reduce the RO bandwidth thereby causing more chemical shift and susceptibility artifact. In addition, the sensitivity to B_0 inhomogeneity becomes larger when applying higher G_{sep} amplitude. If the sampled k-space does not cover the echo shift caused by B_0 inhomogeneity, the reconstructed image suffers from signal loss and distortion. However, compared to simply reducing the number of PE lines in conventional Cartesian sampling, the proposed method is more resistant to B_0 inhomogeneity since it diagonally samples k-space and covers larger k-space area than Cartesian sampling. As shown in the phantom experiment results, voxel modification in a sheared form occurs in the image domain, which results in an anisotropic resolution characteristic. In the k-space perspective, un-sampled and sampled regions cause an anisotropic diagonal resolution pattern. As the gradient ratio ($G_{\text{sep}}/G_{\text{RO}}$) becomes larger, the

sampled k-space region is tilted and stretched more and results in further voxel shearing. To reduce this blurring due to voxel shearing, the gradient amplitude ratio should be kept as small as possible although this will directly affect the acceleration factor. Hence, this method can be useful especially in huge volume and thin-slice thickness 3D imaging which can reduce the voxel spreading. .



Chapter 4

MR Tomosynthesis

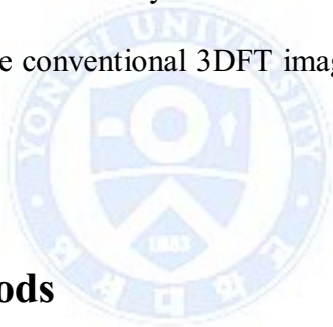
4.1 Introduction

3D MR imaging is widely used for a variety of purposes and has been implemented using different approaches. One of the most common acquisition strategies for 3D MR imaging is to use Cartesian sampling where the selected 3D volume is spatially encoded with phase encodes along two perpendicular spatial directions. The resulting raw data fills a Cartesian 3D k-space matrix, which is reconstructed by a 3D inverse Fourier transform (FT). Different 3D k-space non-Cartesian sampling trajectories exist.(62-65) Generally, reconstruction is performed after interpolating onto a Cartesian k-space sampling grid. Data sampling and reconstruction is widely considered as Fourier domain sampling followed by the FT.

In this chapter, a different 3D imaging approach is introduced which uses 2D projection images acquired at multiple view angles followed by an appropriate reconstruction method. The data acquisition method used, named multiple-oblique view (MOV) pulse sequence, is similar to the VAT pulse sequence.(50) The VAT pulse sequence was originally proposed to correct for chemical-shift and susceptibility-induced artifacts in 2DFT imaging sequences by turning on an additional gradient in the slice-selection direction during the readout. This can be seen as effectively “tilting” the view angle of the selected slice. In this approach, projection images are acquired at different view angles using the MOV pulse sequence by changing the amplitude of the additional gradient. With multiple 2D projection images acquired at different view angles, a set of slice images can be reconstructed which is similar

to the reconstruction used for the tomosynthesis technique recently seen in digital x-ray imaging.(66)

Various reconstruction methods can be used in tomosynthesis.(66-72) Here, the widely used methods, namely, the shift-and-add (SAA), matrix inversion (MI) and iterative back-projection (IBP) reconstruction method are investigated. Furthermore, these algorithms are modified to adapt to the MOV images. In the following, a brief description of these algorithms is provided. The whole data acquisition and reconstruction procedure is similar to x-ray tomosynthesis and hence naming it magnetic resonance tomosynthesis (MRT). Simulations are performed to verify that these reconstruction methods can be applied to MOV images and to analyze the characteristics of MRT. Experiments are done for phantom and in vivo. Although the aim of this study is not focused on comparison, the proposed methods are shown along with the conventional 3DFT imaging method which is regarded as the gold standard for 3D imaging.



4.2 Materials and Methods

4.2.1 MOV Pulse Sequence

An MOV pulse sequence (Fig. 4.1) is used to acquire projection images similar to the images used in tomosynthesis. The MOV pulse sequence can be understood as acquiring images of selectively excited regions projected along the slice-selection direction (z-direction) according to view angles. The view angle θ is determined as the ratio of the additional slice-selection gradient G_{SS_add} to the readout gradient G_{RO} .

$$\theta = \arctan\left(\frac{G_{SS_add}}{G_{RO}}\right) \quad (4.1)$$

Here the view angle is formed in the readout direction (x-direction) as indicated in Fig. 4.1.

Note that the view angle is limited by the gradient system and cannot reach $\pm 90^\circ$ unless turning off G_{RO} .

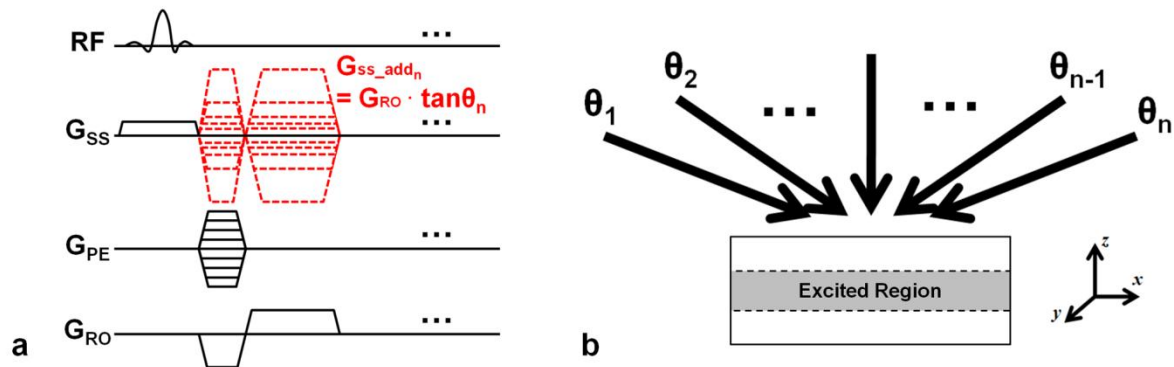


Figure 4.1 (a) MOV pulse sequence diagram and (b) the concept of this pulse sequence from an image domain perspective. The view angles are determined by the ratio of the amplitudes of the readout gradient (G_{RO}) and the additional slice-select gradient (G_{SS_add}).

The image acquisition scheme of the MOV pulse sequence can be regarded as a parallel beam x-ray system where the source and detector move towards opposite directions in a parallel manner. The difference between the x-ray system and the MOV pulse sequence is shown in Fig. 4.2. The primary drawback of x-ray tomosynthesis is blurring due to the residual image contents from distant slices. However, in the MOV images, only the excited region is projected as shown in Fig. 4.2b. This selective excitation scheme in MR can reduce the tomosynthesis blur from the components outside the region of interest (ROI). In tomosynthesis, the goal is to resolve into several planes that the x-ray beam traversed. The number of resolved planes in the reconstruction process should be large enough to ignore the discretization error because the subject is a continuous object. The above description of data acquisition can be expressed as a sum of convolutions of highly resolved n planes with shifted impulses determined by the projection angle. The acquired image $MOV_\theta(x, y)$ along a view angle θ is

$$MOV_{\theta}(x,y) = \sum_{i=1}^n m_i(x,y) \otimes \delta(x-d_{i,\theta}, y), \quad (4.2)$$

where \otimes is convolution, m_i is a true image of i th resolved plane, n is the number of resolved planes, $\delta(x-d_{i,\theta}, y)$ is the impulse shifted $d_{i,\theta}$ along the x-direction corresponding to the slice position of i th resolved plane at an angle θ . For example, Fig. 4.3 shows images of an impulsive bar object viewed at view angles of $\theta = 0^\circ, \pm 30^\circ$ and $\pm 60^\circ$ assuming $1.0 \times 1.0 \text{ mm}^2$ in-plane resolution, 8mm excited slice thickness resolved into 8 planes with 1.0 mm thickness each.

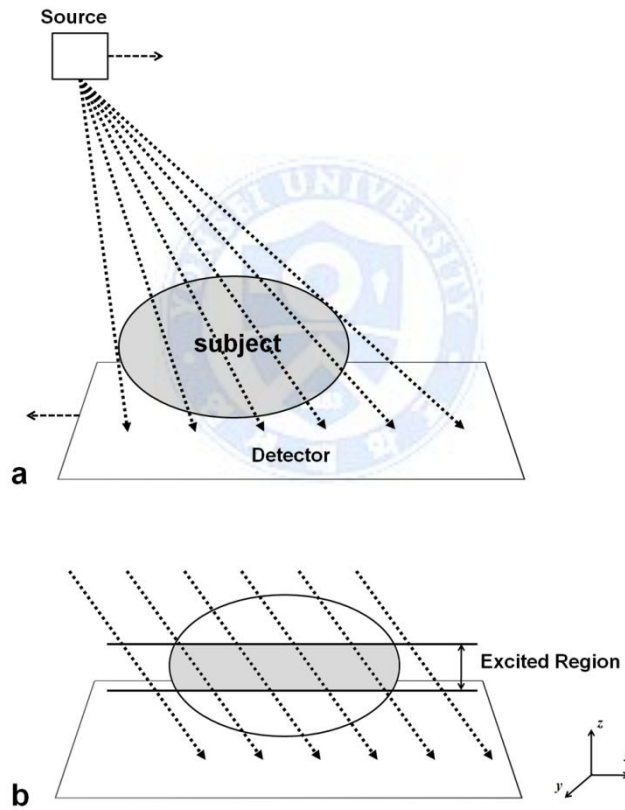


Figure 4.2 Comparison between x-ray tomosynthesis and MRT. (a) Image acquisition scheme of x-ray tomosynthesis system. The source and detector move parallel along opposite directions to acquire the projection images at different angles. The rays spread out radially from the source. (b) Image acquisition scheme of MOV pulse sequence. The components in the excited region are projected along the set view angle.

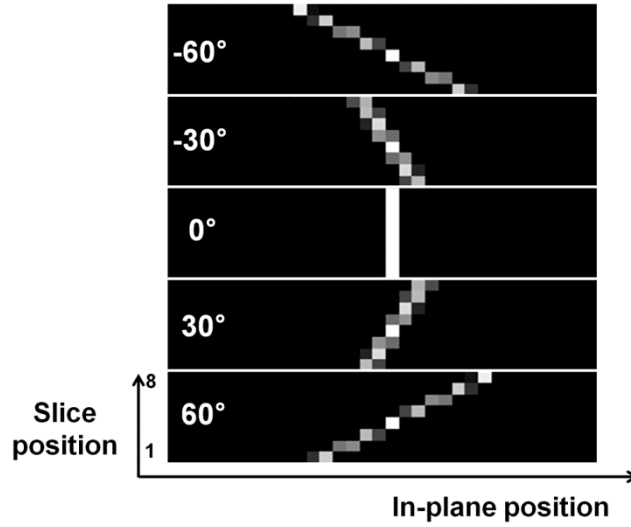


Figure 4.3 Images of an impulsive bar object (shown in the 0° image) viewed at different view angles of 0° , $\pm 30^\circ$ and $\pm 60^\circ$ for slice position 1 to 8. The in-plane position is the readout direction.

4.2.2 Image Reconstruction

4.2.2.i Shift-and-add (SAA) method

The SAA method is the easiest method for generating a set of slice images by simply adding the MOV images shifted back into its original position. This method assumes that the components at different slice positions, which experience varying amount of shifts, are projected onto different in-plane positions for each view angles. The projected positions in the MOV images depend on the distance from the center of the excited thickness to the plane of interest (POI) and the view angle. The amount of shift $d_{i,\theta}$ can be defined by three parameters; the number of resolved slice n , the excited thickness h and the view angle θ . Given an effective resolution $\Delta z = h/n$, and the amount of shift $d_{i,\theta}$ is

$$d_{i,\theta} = \left(i \cdot \Delta z - \frac{h}{2} \right) \cdot \tan\theta, \quad 1 \leq i \leq n \quad (4.3)$$

The acquired MOV images are shifted back according to the calculated shift values and then one plane is reconstructed by the summation of these back-shifted images. This procedure is performed n times by changing the POI to reconstruct all the other planes. This method is used because of the simplicity of the algorithm. However, after SAA reconstruction, although the true components within POI are dominant, components outside of the POI are distributed across the reconstructed image, resulting in a blur artifact. The main topic in tomosynthesis reconstruction is to remove these blur artifacts.

4.2.2.ii Matrix inversion (MI) method

MI method can reduce the blur artifacts in SAA images. If the true image in the i th plane is defined as m_i , then the reconstructed SAA images s_i can be expressed as

$$\begin{aligned}
 s_1 &= m_1 \otimes f_{11} + m_2 \otimes f_{12} + \cdots + m_n \otimes f_{1n} \\
 s_2 &= m_1 \otimes f_{21} + m_2 \otimes f_{22} + \cdots + m_n \otimes f_{2n} \\
 &\vdots \\
 s_n &= m_1 \otimes f_{n1} + m_2 \otimes f_{n2} + \cdots + m_n \otimes f_{nn},
 \end{aligned} \tag{4.4}$$

where f_{ij} is the blurring function for the components in the j th plane that appear in the i th SAA image. s_i is dominated by m_i and therefore f_{ii} , the diagonal components, can be expressed as $A\delta(x, y)$ meaning that no blurring occurred due to m_i . However, the off-diagonal components consist of shifted impulses located along the x-direction and can be calculated using (3). Furthermore, f_{ij} and f_{ji} are the same since they are in diagonal symmetric relation. Taking the Fourier transform of the above equations gives

$$\begin{aligned}
 S_1 &= M_1 \cdot F_{11} + M_2 \cdot F_{12} + \cdots + M_n \cdot F_{1n} \\
 S_2 &= M_1 \cdot F_{21} + M_2 \cdot F_{22} + \cdots + M_n \cdot F_{2n} \\
 &\vdots \\
 S_n &= M_1 \cdot F_{n1} + M_2 \cdot F_{n2} + \cdots + M_n \cdot F_{nn},
 \end{aligned} \tag{4.5}$$

where F_{ij} is the Fourier transform of the blurring function f_{ij} , and S_i and M_i are the

Fourier transforms of s_i and m_i , respectively. The above equation can be rewritten in a simple matrix form

$$\begin{bmatrix} S_1 \\ S_2 \\ \vdots \\ S_n \end{bmatrix} = \begin{bmatrix} F_{11} & F_{12} & \cdots & F_{1n} \\ F_{21} & & & \\ \vdots & & \ddots & \\ F_{n1} & & & F_{nn} \end{bmatrix} \begin{bmatrix} M_1 \\ M_2 \\ \vdots \\ M_n \end{bmatrix}, \quad (4.6)$$

$$\mathbf{S} = \mathbf{F} \cdot \mathbf{M}, \quad (4.7)$$

Since the image acquisition scheme of the MOV pulse sequence is known information, the amount of blurring for each plane can be calculated. The true image \mathbf{M} can be solved by taking the inverse solution. If matrix \mathbf{F} is invertible, the solution \mathbf{M} can be stated simply as

$$\mathbf{M} = \mathbf{F}^{-1} \cdot \mathbf{S}, \quad (4.8)$$

$$\mathbf{m} = IFT\{\mathbf{M}\} = IFT\{\mathbf{F}^{-1} \cdot \mathbf{S}\}. \quad (4.9)$$

If the matrix \mathbf{F} is ill-conditioned due to the low frequency components, regularization methods or frequency blending methods can be used during the inverse process.(73) Here, the pseudo-inverse using singular value decomposition is used to solve the inverse problem. To deal with the ill-conditioned matrix due to the low frequencies, the singular values near zero are thresholded.

4.2.2.iii Iterative back-projection (IBP) method

This method focuses on deblurring using back-projected images. The back-projection (BP) algorithm commonly used in computed tomography (CT) is applied to the acquired MOV data. The approach is valid since the MOV pulse sequence can be regarded as collecting

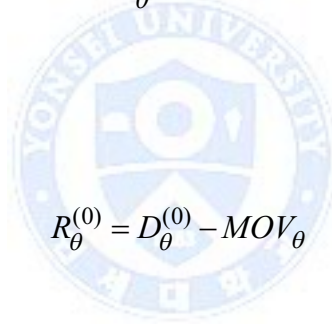
projected parallel ray data as mentioned before. A detailed description of this algorithm can be found in (66). In the first step, back project the MOV images along slice direction.

$$T^{(0)} = BP\{MOV_{\theta}\}, \text{ for all acquisition angles } \theta \quad (4.10)$$

The results of this process is initial images $T^{(0)}$ which are the same as the results of the SAA reconstruction. Afterwards, a forward-projection (FP) is applied

$$D_{\theta}^{(0)} = FP\{T^{(0)}\}, \text{ for all acquisition angles } \theta \quad (4.11)$$

and the MOV data is subtracted from $D_{\theta}^{(0)}$ to find the residual values $R_{\theta}^{(0)}$ caused by blurrings in the SAA images.



$$R_{\theta}^{(0)} = D_{\theta}^{(0)} - MOV_{\theta} \quad (4.12)$$

The residual data $R_{\theta}^{(0)}$ are then projected back again and subtracted to the initial back-projection image $T^{(0)}$.

$$T^{(1)} = T^{(0)} - BP\{R_{\theta}^{(0)}\}, \text{ for all acquisition angles } \theta \quad (4.13)$$

$T^{(1)}$ is now less blur than $T^{(0)}$. The above routine is performed iteratively until the residual values $R_{\theta}^{(0)}$ are less than some specific threshold value. The final result is the deblurred images $T^{(N_{iter})}$.

4.2.2.iv Reformatted reconstruction using thinner slice thickness and/or extended field-of-view (FOV)

The number of slices and/or the FOV can be flexibly chosen in the reconstruction process mentioned above to adjust to the MR situation.

Increasing the number of slices enables thinner slices to be reconstructed. By doing this, the resolution in the slice direction can be partially increased. Especially, this can be of value in the reconstruction of imaging objects with high structural variations in certain directions. It is notable that this procedure is different from the zero-padding interpolation procedure commonly used in the reconstruction process.

Another extension is the flexibility in choosing the reconstructed FOV. Extending the FOV can be of value since it can resolve signals outside of the slice-select region. This mostly comes from non-ideal RF profile in the selection procedure. Transition bands in the RF profile and/or side-lobes exist outside the desired regions. By using an extended FOV reconstruction, these components can be resolved.

With these approaches, conventional reconstruction methods used in tomosynthesis can be adapted to fit the characteristics of the acquired MOV data.

4.2.3 Simulations

Simulations were performed using a 3D impulsive object to estimate the spatial spread and the full width half maximum (FWHM) of the point spread function (PSF). A manually designed 3D oval shell phantom was also used to apply and compare the various reconstruction methods mentioned. The size of designed 3D phantom was $256 \times 256 \times 64 \text{ mm}^3$ on a $256 \times 256 \times 128$ matrix. MOV images were generated by projecting the phantom along tilted view angles as shown in Fig. 4.2. The number of view angles was 33 from -80° to 80° with 5° interval. The acquisition resolutions assumed were $2.0 \times 2.0 \times 64.0 \text{ mm}^3$ with 128

x 128 matrix for the MOV images. The MOV images were reconstructed as 3D images with 2.0 mm slice thickness and 0.5 mm slice thickness when using the reformatted thinner slice reconstruction as mentioned above. For comparison, conventional 3DFT phantom images were also generated assuming 2.0 x 2.0 x 2.0 mm³ resolution with an 128 x 128 x 32 matrix.

4.2.4 Data acquisition and reconstruction

Phantom (agar filled vascular wax phantom) and in vivo head MR images were obtained on a 3T scanner (Tim-Trio System, Siemens Medical Solutions, Erlangen, Germany). A spoiled gradient echo sequence (SPGR) was modified by incorporating the MOV pulse sequence. The scan parameters of the MOV pulse sequence were TR = 30.0 ms, TE = 7.68 ms, 10.0 mm nominal excitation slice thickness and 17 view angles from -80° to 80° with 10° interval. For phantom acquisition 1.0 x 1.0 mm² in-plane resolution was used while for in vivo acquisition the in-plane resolution was adjusted to either 2.0 x 2.0 mm² (12 channel head coil) or 1.2 x 1.2 mm² (body coil) to demonstrate high and low SNR cases respectively. For the reconstruction, the resolved slice thickness was set to 0.63 mm with 16 slices using the SAA, MI and IBP approaches. Using the reformatted thinner slice reconstruction, the number of slices was increased to 64 slices with 0.157 mm thickness. In all phantom and in vivo reconstruction, the reformatted extended FOV reconstruction method was applied. Conventional 3DFT SPGR sequence with nearly identical scan time as the MOV acquisition was also acquired for comparison with 16 phase encodings along the same nominal excitation region. The processing time, FWHM of PSF, SNR of each reconstruction method were measured for the in vivo case to provide quantitative comparison between 3DFT and MRT. In addition, the SNR of the 3DFT image after applying a smoothing filter such that the FWHM of the 3DFT PSF matches the FWHM of the other reconstruction method was calculated.

4.2.5 SNR analysis

The noise characteristics of x-ray and MR systems are different. The noise characteristic of x-ray follows Poisson distribution which depends on the ray-path and the amount of photons. In MR, the noise is characterized as being Gaussian and it depends on the acquisition time and the voxel size. SNR of MR signal can be represented as Eq. (4.14).

$$SNR \propto \Delta x \Delta y \Delta z \sqrt{T_{acq}} \quad (4.14)$$

, where Δx , Δy and Δz are the resolutions along each direction and T_{acq} is total acquisition time. Consider conventional 3DFT and MOV image acquisitions. If the slab thickness is h and the number of phase encodings along the slice direction is N_{phase} , the slice direction resolution for 3DFT imaging would be h/N_{phase} . Since the MOV is a 2D pulse sequence, the slice thickness of one MOV image corresponds to the slab thickness h . The total acquisition time of 3DFT images is N_{phase} times longer than the acquisition time of single MOV acquisition, therefore from Eq. (4.14), the thickness factor and the acquisition time factor make the MOV image have $\sqrt{N_{phase}}$ times higher SNR than 3DFT images. Furthermore, the MOV pulse sequence acquires multiple view angle data meaning that the total number of acquired MOV images is N_{angle} and each of these images has $\sqrt{N_{phase}}$ times higher SNR compared to 3DFT images. In the case of SAA reconstruction, which is the simplest tomosynthesis reconstruction, we can regard the reconstruction process as simply averaging all the MOV images which will increase the SNR by $\sqrt{N_{angle}}$ fold. Hence, the SNR of the center slice of the SAA reconstructed images is approximately $\sqrt{(N_{phase} \cdot N_{angle})}$ times higher than the SNR of 3DFT images. Almost all other tomosynthesis reconstruction methods start from this SAA images as its initial starting point. The high SNR of SAA images drive reconstructed images using other methods to have high SNR even though other reconstruction methods will amplify noise components during the de-blurring process.

Simulations were performed on 3D Shepp-logan phantom to show the SNR behavior of the MRT method by varying the amount of noise. As a reference, the same simulations were performed for the conventional 3DFT method as well. The FOV was set at 256 x 256 x 32 mm³ and the matrix size is 128 x 128 x 32 for conventional 3DFT imaging and 128 x 128 with 35 view angles, -85° to 85° with 5° interval, MOV images for MRT reconstruction. Gaussian noise with different standard deviations $\sigma=1, 2, 3, 4$ and 5 were added.

4.3 Results

4.3.1 Simulation

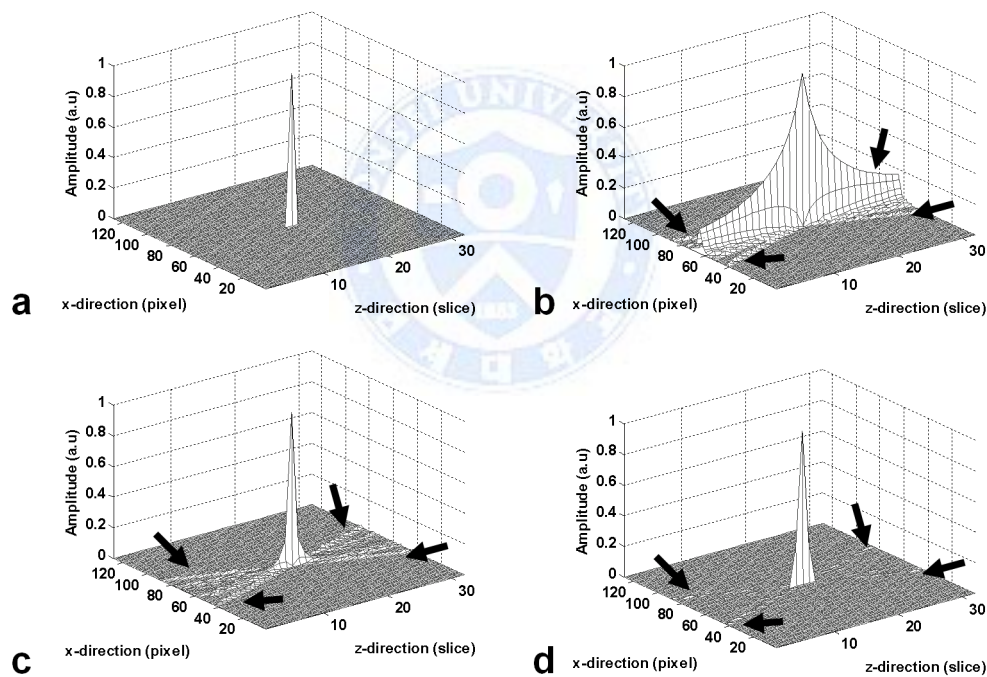


Figure 4.4 Simulation results of PSF for (a) 3DFT, (b) SAA, (c) MI and (d) IBP reconstructions in the x-z plane. The FWHM ratios of SAA, MI and IBP to 3DFT reconstructions are 7.88, 1.34 and 1.32 respectively. Side-lobe components spreading to other regions are shown (arrows). The magnitude has been normalized for each method.

Figure 4.4 shows the PSFs of each reconstruction method. The PSFs are shown only along the readout (x) direction and slice-selection (z) direction. The PSF patterns of each MRT methods showed no difference along the phase encode (y) direction compared to the 3DFT. The FWHM of the SAA method shows the largest FWHM value along the z-direction, which is approximately eight-fold FWHM of the 3DFT method. However, the FWHM of the other two deblurring methods, namely MI and IBP, shows slight partial blurring compared to the results from the 3DFT reconstruction. More precisely, the FWHM ratios of MI to 3DFT and IBP to 3DFT were 1.340 and 1.325, respectively. In addition, as indicated by arrows in Fig. 4.4(b-d), MI and IBP methods show residual components along the projection lines similar to streak artifacts. These results suggest that the reconstruction methods (except SAA) can be applied to generate 3D MR images using the proposed approach. However, a partial loss in resolution along the slice direction compared to the conventional 3DFT method can be expected.

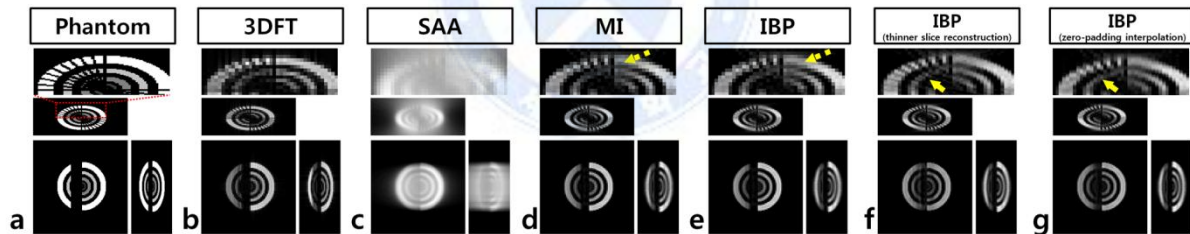


Figure 4.5 Simulation results for an oval 3D phantom with radial stripes (a) using 3DFT (b), SAA (c), MI (d) and IBP (e) . For each reconstruction method, the mid axial (left bottom), mid coronal (upper), and mid sagittal (right) images are shown. The magnified images of the boxed region in the mid coronal image are also shown (top). Resulting images using the reformatted thinner slice reconstruction and the simple zero-padding interpolation are shown in (f) and (g) respectively.

Figure 4.5 shows the reconstruction results including the reformatted thinner slice reconstruction approach from the manually designed 3D phantom. The original phantom

contained radial stripes [Fig. 4.5(a)]. The SAA method [Fig. 4.5(c)] shows severe blur giving an unacceptable result. The MI and IBP methods show intensity loss [dotted arrows in Fig. 4.5(d and e)] due to blurring along the slice direction which is angularly dependent. The regions of the intensity loss are related with the blurring and streak patterns from the PSF simulations. Using the thinner slice reconstruction, however, detail information [solid arrow in Fig. 4.5(f)] can be obtained compared to the original IBP reconstruction. As is also observable, this is different from simple zero-padding interpolation [Fig. 4.5(g)].

Figure 4.6 shows the noise simulation results on 3D Shepp-logan phantom. It is obvious that the results show SNR improvement in the case of using MRT method. SNR of 3D imaging case is inverse-proportional to the noise power as in common MRI. However, in MRT, this relationship does not hold as the graph in fig. 4.6.

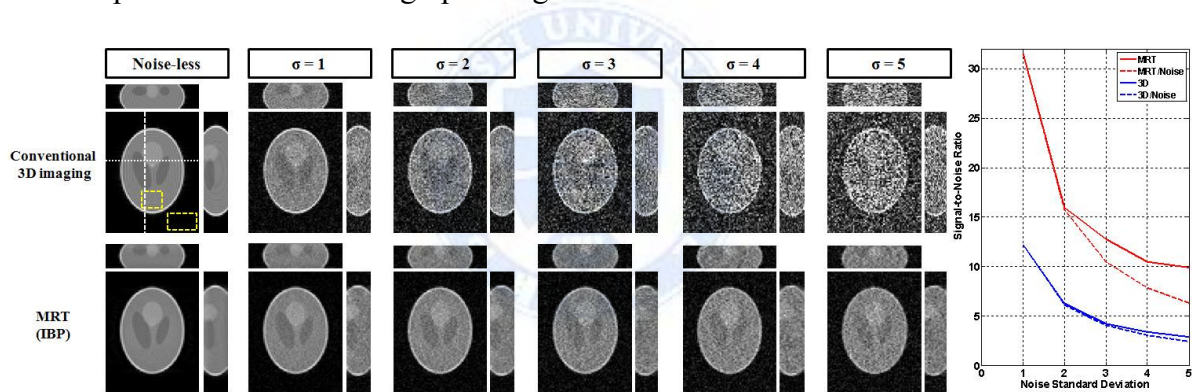


Figure 4.6 Simulation results on 3D Shepp-logan phantom. For each image set, the upper image corresponds to the mid coronal view (dotted line), the image on the right corresponds to the mid sagittal view (dashed line), and the largest images are the 9th slice image of 32 slices. The upper row set images are conventional 3D imaging with inscribed noise standard deviation and the lower row images are IBP reconstruction results. The computed SNR is plotted at the right side (solid curve) along with the theoretical SNR graph (dot curve). The dotted boxes in the image indicate the signal and noise region used to calculate SNR. The dotted boxes indicate the signal region and the noise region using to calculate SNR.

4.3.2 Experiments

Figure 4.7 shows five sample raw images of the 17 multiple projections acquired with the MOV pulse sequence prior to reconstruction for both phantom and in vivo. Note the displacement of the vascular phantom along varying view angle is similar to x-ray tomosynthesis images. Slice directional information is mapped to the readout direction thereby enabling a 3D reconstruction.

The effects of using the reformatted extended FOV approach is shown with the phantom images in Fig. 4.8. Bright artifact pattern is observed in Fig. 4.8(a) obtained with a 3DFT acquisition. This is also seen in Fig. 4.8(b) reconstructed without the extended FOV approach. These are due to components outside the prescribed slice that are partially excited which subsequently roll over to the reconstructed region. Using the extended FOV reconstruction with wider range in the z-direction allows alleviation of these RF excitation imperfection effects as in Fig. 4.8(c).

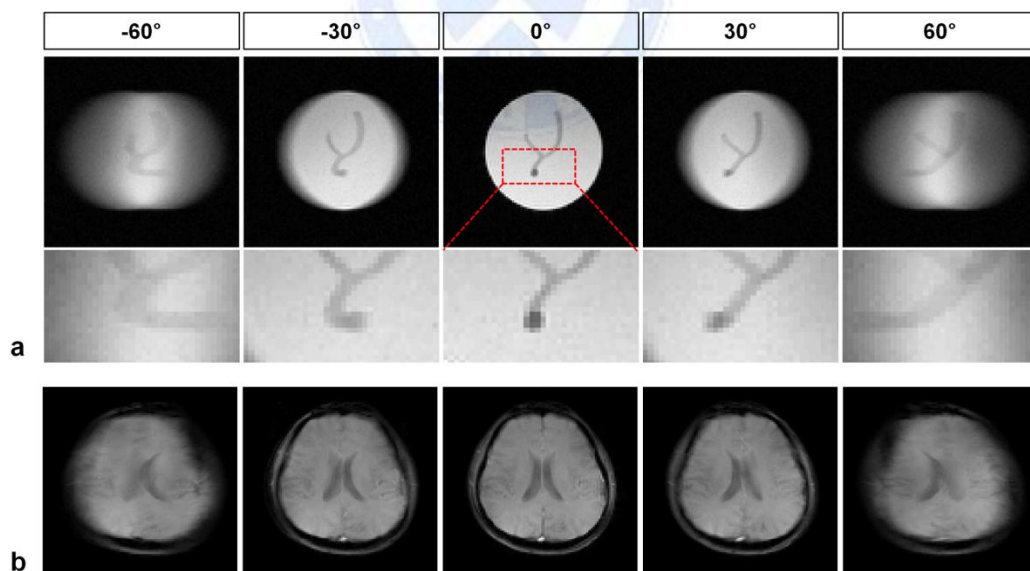


Figure 4.7 Acquired raw images using the MOV pulse sequence from the vascular phantom (a) and in vivo (b). The corresponding view angles are -60° , -30° , 0° , 30° and 60° . The boxed region magnified in (a) demonstrate that the vascular region are depicted as images viewed at the different view angles.

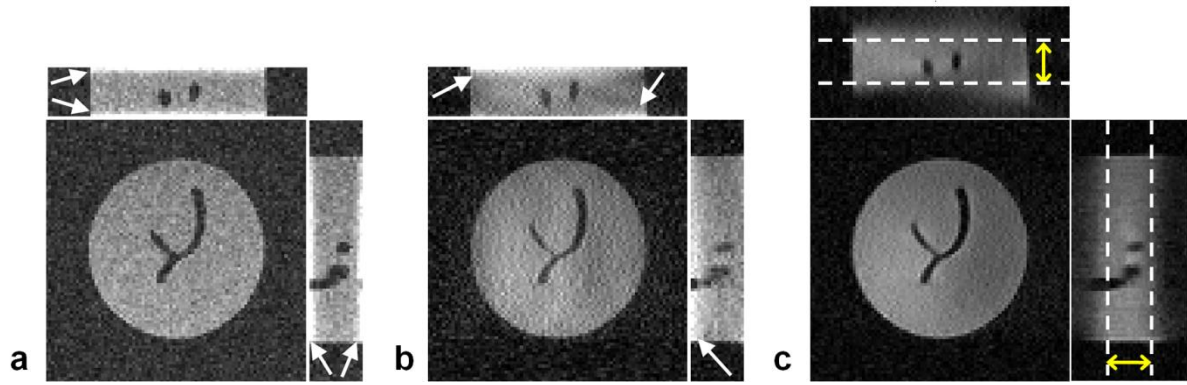


Figure 4.8 Phantom experiment results of 3DFT imaging (a), MRT (MI) method without (b) and with (c) the extended FOV reconstruction. Aliasing artifacts due to the imperfect excitation profile are observed in (a) and (b) (arrows). The extended FOV was set to three times the nominal imaging thickness (dashed lines). Unwanted components from outside of the nominal excited slice are spread out.

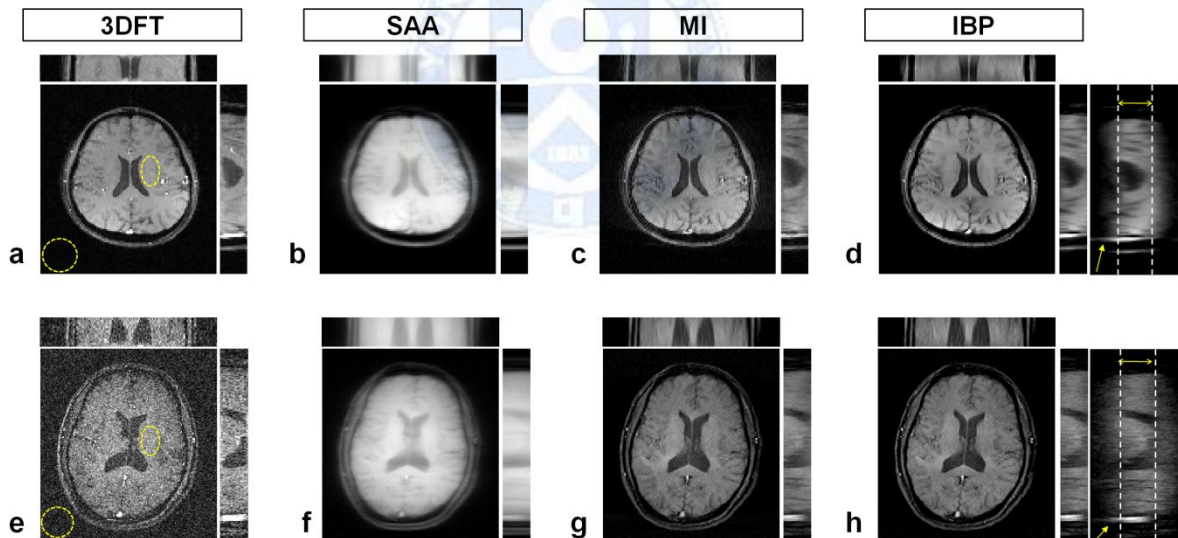


Figure 4.9 In vivo results for high SNR (a-d) and low SNR (e-h) experiment. The 3DFT method and the MRT method with different reconstructions are shown for comparison. All MRT images are reconstructed using the extended FOV method. As an example, the full extended FOV that are actually reconstructed are also shown in (d) and (h). The boundaries of the actual imaging thickness are drawn with dashed lines. The regions for SNR calculation are circled by yellow dashes.

	3DFT		SAA	MI	IBP
SNR (Filtered SNR ^a)	Case1 ^b	52.34	867.08 (104.74)	78.86 (63.19)	84.11 (62.93)
	Case2 ^c	6.87	284.64 (22.73)	31.47 (9.05)	38.54 (8.93)
FWHM of PSF	1.00		7.88	1.34	1.32
Processing Time	0.06 s		8.12 s	87.84 s	112.76 s

^aSNR of 3DFT image after applying smoothing filter. Each smoothing filter follows the FWHM of PSF of each MRT reconstruction.

^bHigh SNR in vivo case in Fig. 8a-d (2.0x2.0 mm² inplane resolution and using 8ch birdcage receiver coil)

^cLow SNR in vivo case in Fig. 8e-h (1.2x1.2 mm² inplane resolution and using body receiver coil)

Table 4.1 Overview of MRT performances compared to 3DFT

The reconstructed images of the phantom and in vivo data are shown in Fig. 4.9. In-plane axial images show satisfactory results using MI and IBP reconstruction. These results are particularly noticeable in the low SNR case [Fig. 4.9(e-h)] where improved images with lower noise are obtained compared to the 3DFT images. However, reconstructed images using the MRT methods show slight blurring along the slice-direction as expected from the simulation results. Table 4.1 provides quantitative values of MRT performance showing the processing time, FWHM of PSF, and SNR of each reconstruction method. MRT reconstruction requires much more time than 3DFT reconstruction although further optimization can shorten it. In the parenthesis, the SNR after filtering the 3DFT PSF to match other reconstruction method FWHM is noted. The smoothing process can give SNR gain to the 3DFT image with less computational effort. However, MRT reconstruction has higher SNR compared to the smoothing filtering, especially in low SNR in vivo case,. The images using the extended FOV IBP reconstruction [Fig.4.9(d, h)] are interesting since it shows the superior sagittal sinus to be localized at a shifted position (arrow) with respect to other static tissue. This is presumably due to flow during the time interval between excitation and data acquisition, which can be resolved using the extended FOV reconstruction.

All the reconstructed slices using the MRT method are shown in Fig. 4.10(a). The reconstructed MRT images show comparable morphometric information with the 3DFT

images [Fig. 4.10(b)]. As previously shown, bright images due to the unwanted signals from outside of ROI are observed for the 3DFT images since the FOV selected coincides with the slice thickness resulting in wrapping artifacts. The MRT method, by incorporating the extended FOV reconstruction can alleviate this problem.

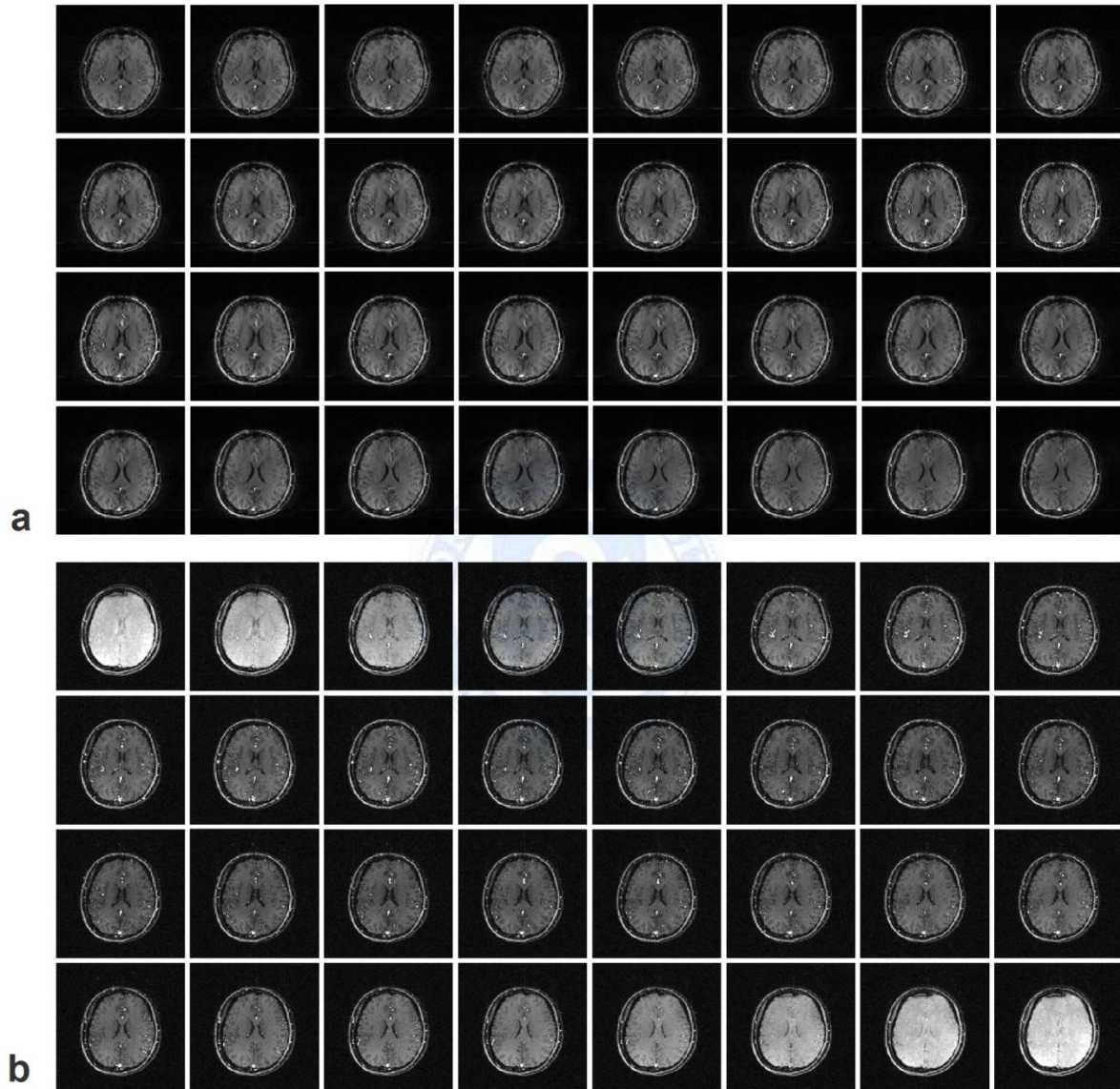


Figure 4.10 All axial slices obtained using (a) MRT (MI reconstruction) and (b) 3DFT with 32 phase encodings in z are shown. The aliasing artifacts are observed around the end of slices in (b). Using extended FOV reconstruction, the aliasing artifact problem can be alleviated in (a).

4.4 Discussion

The VAT pulse sequence was originally proposed to correct susceptibility induced artifacts by effectively acquiring images at an oblique view.(50) Here, the view angle tilting concept is extended. By acquiring data at multiple different view angles, the reconstruction problem is formulated to be equivalent to that used in tomosynthesis. Reconstruction methods used in tomosynthesis were applied. It is shown that 3D MR imaging can be achieved using the presented method. Although MRT images provided along with the conventional 3DFT images, this study is not aimed at the comparison of these two methods. The main focus is to introduce an alternative approach for 3D MR imaging by reformatting the data acquisition and reconstruction problem to that of the x-ray tomosynthesis technique. The proposed method is implemented and extended on the most basic reconstruction algorithms used in tomosynthesis reconstruction.

MR images are normally reconstructed via FT from the k-space domain. Here, the samples are collected in k-space but reconstruction can be performed in image domain since they are considered as projections at different view angles. In using various reconstruction methods, the characteristics associated with each algorithm are readily seen in the final images. Other algorithms used in tomosynthesis to be readily incorporated into MOV acquisition data. For example, to account for the spatial blur, various iterative methods with spatial priors or statistical modeling used in the x-ray tomosynthesis or CT reconstruction can be incorporated to the MRT method.(74) In addition, other image based model reconstruction methods using regularization approaches can be included to enhance different features.(75)

From a k-space perspective, MOV samples k_z during k_x readout sampling. A different view angle corresponds to a different k_z trajectory while k_x readout is maintained. After all view angles are acquired, two trigonal-prism shaped regions in k_z - k_x perspective will be sampled. The maximum extent of k_z sampling will be longer than the maximum extent of k_z sampled

using 3DFT indicating that the MRT method need not have worse resolution. In some sense, the trajectory is similar to an anisotropic radial trajectory(76) with additional unsampled regions near the kz axis. The sequence, however, is a simple modification of conventional 2DFT sequence as shown in Fig. 4.1 and therefore can be readily applied to gradient echo, spin echo or other imaging sequences.

Reconstructed image quality seems to depend on the shape of the imaged object. Various shaped phantoms were simulated (results not shown) which gave results with increased or decreased amounts of the artifacts that were observed in Fig. 4.5. A quantitative analysis of resolution and/or SNR was therefore difficult to perform although the PSF simulations and Table 1 provides give a general view. In general, imaging structures having k-space spectral components mainly filling the sampled k-space regions are likely to reconstruct well while those dominated by spectral components filling the unsampled regions are likely to have artifacts. These include structures mainly have a horizontal feature. The applications of the proposed method are therefore likely to be apt to predetermined structures with vertical structures, e.g., high resolution angiographic imaging through the vertical vessels. The SNR characteristics of 3DFT and MRT have been previously provided by Kim et al., (77) and the results show that MRT is not governed by the typical resolution and SNR tradeoff relationship known in 3DFT MR imaging. The SNR gain in MRT is a consequence of the widened PSF in reconstruction process and the data acquisition strategy of MOV sequence which samples the k-space origin repeatedly resulting in larger total signal power compared to 3DFT. If regularization or other particular tomosynthesis algorithms are used for reconstruction, the SNR characteristics can be changed accordingly.

A detailed study of the optimal view angles and their separation should be provided. In x-ray tomosynthesis, the amount of dose and hardware limitations are considered to find the optimal acquisition geometry. Under the limited total dose condition, the number of

projections and the SNR of reconstructed images have an inverse relation. In this case, the optimal acquisition is maximizing the angular range which can improve through-plane resolution while choosing the number of projections considering the SNR of reconstructed images.(78) However, in MR, there is no the dose limitation to prevent acquisition of more projection data. Specific absorption rate (SAR) issues can be ignored with SPGR sequence which uses low flip angle excitation scheme. Then, just more time is needed to acquire more projection data. It is natural that SNR improvement can be achieved by averaging more acquisitions in MR. In other words, more projection data makes the reconstructed images have better SNR. But, the number of projection data is fixed as the number of slice-phase encodings in the conventional 3DFT acquisition to match the acquisition time of two methods. With the fixed number of projections, the view angle range and separation should be considered. By maximizing the view angle range, the through-plane resolution of the MRT images can be increased.

By using the reformatted thinner slice and/or extended FOV approach, the performance of the reconstruction was improved. This is important because the thinner slice reconstruction provides additional structural information since higher spatial frequency regions along k_z that are sampled can be incorporated in the reconstruction process. Therefore, this method is different from the simple zero-padding interpolation. The extended FOV reconstruction can incorporate the RF imperfections into the reconstruction process. With this, imperfections in slice profile and/or chemical shift misregistration in RF excitation could be resolvable. In addition, this reconstruction algorithm may be useful for localization of flow and motion components. Since flow components (in the slice direction) are encoded simultaneously during the data acquisition, velocity measurements seem to be feasible. Further exploration of these potential applications is a subject of future studies.

Chapter 5

Fast B_1^+ mapping and correction in bSSFP

5.1 Introduction

Balanced steady-state free precession (bSSFP) is routinely performed in clinical imaging such as cardiac cine, angiography, and abdominal imaging (79,80). The bSSFP imaging technique has distinct advantages such as high signal-to-noise ratio (SNR) efficiency compared to conventional spoiled gradient echo (SPGR), and high contrast-to-noise ratio (CNR) especially between flow and stationary tissues (81). The drawbacks are the sensitive to B_0 and B_1^+ inhomogeneity. Banding artifacts occur where the phase accumulation due to field inhomogeneity during the TR period is near $\pm\pi$. Furthermore, B_1^+ inhomogeneity also causes spatial signal variation in conjunction with B_0 -induced variation (82). Since T_2/T_1 weighting in bSSFP depends on the flip angle, its contrast can be altered by B_1^+ inhomogeneity (83,84). In clinical applications of bSSFP imaging, unwanted signal modulations due to nonuniform B_1^+ distribution were reported especially over 3T machine (85-87) and it can be an error source in several functional studies in neuronal, cardiovascular, abdominal MRI (88,89).

The spatial distribution of B_1^+ depends on the main magnet strength which determines the resonance frequency and wavelength of applied RF pulse (27,32). Moreover, the size and electrical properties of the imaging object also affect the B_1^+ distribution. Thus, B_1^+ map has a patient-specific feature and needs to be estimate individually. This B_1^+ mapping can be useful for many MR applications such as determining local specific absorption ratio (SAR)(90), shimming transmit field in parallel transmit system (91-93), correcting B_1^+

inhomogeneity induced intensity distortions in quantitative studies (29-31) or estimating electrical properties (94). Many B_1^+ mapping techniques have been developed. B_1^+ map estimated using relationships between acquired signals at different flip angles is often used. Among them the double angle method (DAM) is commonly referred to as the gold standard(32). Although this technique requires the TR to be 5 times longer than the T_1 of the subject thus prohibiting clinical usage, many previous studies regarding new B_1^+ mapping methods compared their results to DAM to evaluate the performance in terms of accuracy, signal-to-noise ratio (SNR), relaxation dependency, etc. Several B_1^+ mapping methods using SSFP signal were proposed (95-97). Recently, B_1^+ mapping method using unbalanced SSFP imaging was introduced (35). It used the frequency of signal oscillations in the transient phase of SSFP and MR spectroscopic analysis was adapted to extract the oscillation frequency. In this technique, tissue relaxation related errors were ignorable with short TR acquisition. Furthermore, B_1^+ mapping particularly in a 2D multislice imaging was rather insensitive to off-resonance than that of 3D imaging. Since total acquisition time increased to acquire more accurate oscillation pattern, it has a trade-off between speed and accuracy.

In this chapter, a fast B_1^+ mapping method using magnitude information from the early stages of the transient-state in bSSFP is proposed. During transient-state, flip angles (FA) are modified to acquire images similar to DAM with single-shot spiral readout applied for efficient acquisition-space coverage. In addition, a bridge pulse is inserted for smooth transition to the following bSSFP image acquisition stage. Using the estimated B_1^+ map, intensity modulations induced by B_1^+ inhomogeneity are corrected. Bloch simulations are performed to assess the performance of the proposed B_1^+ mapping technique with various parameters such as T_1 , T_2 , FA and off-resonance. The B_1^+ mapping and correction is demonstrated using phantom and in vivo studies.

5.2 Methods

5.2.1 B_1^+ Estimation Pulse sequence

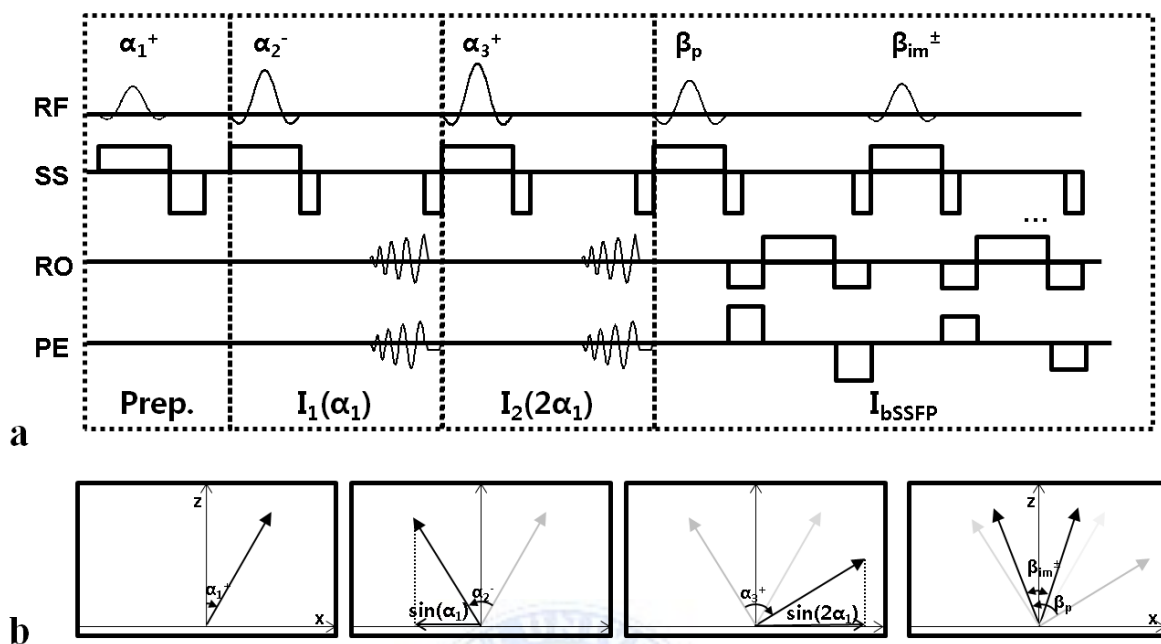


Figure 5.1 (a) A pulse sequence diagram of the proposed B_1^+ estimation ($|\alpha_2| = 2|\alpha_1|$ and $|\alpha_3| = 3|\alpha_1|$). (b) Illustrations of magnetization changes corresponding to each sequence block in (a)

Signals in bSSFP can be divided into the transient- and steady-state. Signal fluctuations in the transient state can be stabilized by catalyzation schemes such as $\alpha/2$ or Kaiser-windowed ramp preparation (79). These transient state signals are sometimes used to fill the periphery of k-space where the effects are small to the overall image contrast but increases time efficiency. Normally, the signals are usually discarded. . In this transient-state, the amplitude of signal is governed by factors such as FA, T_1 , T_2 and ΔB_0 . In order to enable B_1^+ mapping during the transient state, the conventional bSSFP sequence is modified [Fig. 5.1(a)] such that it consists of 4 blocks, namely, the preparation, I_1 , I_2 , and imaging block. In the preparation stage, an α_1 pulse is introduced to prepare for the B_1^+ mapping and catalyzing bSSFP signal, followed by two opposite-phase pulses (α_2 and α_3) in the I_1 and I_2 blocks for the double angle acquisition stage. Finally, β_p is applied as a bridge pulse and β_{im} pulses are applied for normal

bSSFP imaging. During the double angle acquisition stage, the FAs α_2 and α_3 are can be defined in different ways depending on the acquisition order of the images which will be dominated by $\sin(\alpha_1)$ and $\sin(2\alpha_1)$. As an illustration, the first one is to let $|\alpha_2| = 2|\alpha_1|$ and $|\alpha_3| = 3|\alpha_1|$ which results in $I_1 \propto \sin(\alpha_1)$ and $I_2 \propto \sin(2\alpha_1)$. Another one is to let $|\alpha_2| = 3|\alpha_1|$ and $|\alpha_3| = 3|\alpha_1|$ which results in $I_1 \propto \sin(2\alpha_1)$ and $I_2 \propto \sin(\alpha_1)$. Then, β_p should be $2\alpha_1 + \beta_{im}/2$ or $\alpha_1 + \beta_{im}/2$, respectively. Figure 5.1(b) shows the magnetization changes during the individual sequence blocks for the case when $|\alpha_2| = 2|\alpha_1|$ and $|\alpha_3| = 3|\alpha_1|$. For fast B_1^+ mapping, two assumptions are made, 1) B_1^+ varies slowly in spatial domain; a low resolution image can represent B_1^+ distribution, and 2) T_1 and T_2 relaxations are negligible if TR is much shorter than T_1, T_2 ; FA dominates overall signal in the early-stage of transient state in bSSFP. Under these assumptions, the I_1 and I_2 signals are acquired using single-shot spiral technique and the B_1^+ map can be calculated from these two data sets in a similar manner to DAM. The conventional bSSFP image can be acquired following a bridge β_p pulse and β_{im} pulses. Thus, total scan time increment due to the B_1^+ mapping is negligible compared to the conventional bSSFP acquisition ($2 \cdot TR$ increment). Furthermore, FAs for B_1^+ mapping (α) and imaging (β_{im}) are applied independently by means of the bridge pulse (β_p), therefore, image contrast can be manipulated regardless of α . Moreover, SAR can be well controlled.

With these assumptions, the signals of I_1 and I_2 can be represented by $\sin(\alpha_1)$ and $\sin(2\alpha_1)$ respectively [Fig. 5.1(b)]. Therefore, the actual flip angle distribution can be estimated by,

$$\alpha_{\text{actual}} = \cos^{-1}(I_2/2I_1).$$

Meanwhile, as time elapses, the transient-state signal is affected more by T_1 and T_2 relaxations. Thus, in order to minimize the relaxation effect and off-resonance, TR should be shortened as much as possible which is also desired in bSSFP to avoid banding artifact. Thus a single-shot spiral k-space acquisition is used during the acquisition of I_1 and I_2 signals. Although the short TR limits readout duration and consequently limits spatial resolution of

the single-shot spiral trajectory, the low resolution images I_1 and I_2 are sufficient with the assumption of a slow-varying spatial B_1^+ field.

5.2.2 B_1^+ Estimation Error Simulations

The amount of the B_1^+ estimation error caused by the assumption that T_1 and T_2 relaxations during 2TR are negligible was quantified. Furthermore, the influence of flip angle α and off-resonance which can also affect the accuracy of B_1^+ map were checked. Normalized estimation error was calculated using the estimated B_1^+ and true B_1^+ using the following parameters which were tested via Bloch simulation. First, the simulation assumed $TR = 5\text{ms}$, $\alpha_1 = 30^\circ$, $\Delta B_0 = 0\text{Hz}$ with varying T_{1s} (10~1000ms, 10ms interval), T_{2s} (10~1000ms, 10ms interval) to analyze the error and its tendency according to relaxation parameters. T_2 values with longer corresponding T_1 were excluded from the simulation. Next, based on the first simulation results, B_1^+ estimation errors were computed with varying T_{2s} (10 ~ 1000ms, 10ms interval), FAs (1~60°, 1° interval), off-resonances (0~200 Hz, 10 Hz interval) and fixed $T_1 = 1000\text{ms}$ to explore the optimal α value which can make the estimated B_1^+ map less sensitive to T_2 relaxation and off-resonance.

All post-processing methods were implemented on a PC (Intel Pentium Processor 2.4 GHz, 8 GB of RAM) operating on a Microsoft Windows 7 operating system using MATLAB R2009b (Mathworks, Natick, MA, USA).

5.2.3 Experiments

All experiments were performed on a 3T MR scanner (Tim Trio, Siemens, Erlangen). A cylindrical water phantom of which T_1 and T_2 are 120ms and 80ms respectively and *in vivo* brain images were acquired with a 12-channel birdcage receiver head coil. *In vivo* liver images were acquired with breath-hold using a body-matrix receiver coil. In the phantom

experiment, various flip angles of α from 30° to 70° with 5° interval were tested to check for the optimal flip angle for B_1^+ mapping. The applied RF pulse used a hamming windowed sinc with 1.2ms duration. A conventional B_1^+ mapping, specifically the DAM, was acquired for comparison using spin-echo (SE) sequence with TR = 3000ms, TE = 12ms, flip angle 60° - 180° for I_1 and 120° - 180° for I_2 . All bSSFP images were acquired following parameters; TR = 5ms, TE = 2.5ms, $\beta_{im} = 30^\circ$, FOV = 256 x 256 mm², matrix size = 12x12 (148 samples) for spiral B_1^+ acquisition and 128x128 for normal bSSFP imaging, slice thickness = 5.0mm, total acquisition time = 653ms.

The purpose of this study is correcting B_1^+ -induced intensity modulation in bSSFP. B_1^+ correction was performed by demodulating $\sin(B_1^+ \cdot (\beta_{im}/2))$ on the acquired image. For comparison, the acquired image was demodulated by $\sin(\beta_{im}/2)$ as well. In order to evaluate the correction performance, normalized standard deviations (σ) of intensities excluding the background region were calculated with the images before and after B_1^+ correction because σ values can represent the homogeneity of the phantom image.

5.3 Results

5.3.1 Simulation

Figure 5.2(a) represents the B_1^+ estimation errors for difference T_1 and T_2 values. According to the simulation result, the estimation errors are affected more by T_2 than T_1 . In other words, the performance of the proposed B_1^+ mapping highly depends on T_2 . This T_2 dependency can be supported by the fact that T_1 is relatively longer than T_2 in practice although both T_1 and T_2 are important factors on B_1^+ estimation. Based on this simulation result which suggests that the proposed B_1^+ mapping is less sensitive to T_1 , the following simulations were performed with fixed T_1 ($T_1 = 1000$ ms). The accuracy of B_1^+ estimation according to various T_2 and α is shown in Fig.5.2(b). In general, B_1^+ was overestimated with relatively small α

($<30^\circ$) as well as short T_2 s similar to the previous simulation result. According to this result, larger α is helpful in acquiring more accurate B_1^+ map. Furthermore, the effect of off-resonance on B_1^+ estimation highly depends on applied α value [Fig. 5.2(c)]. Under inhomogeneous B_0 field, large α ($>50^\circ$) is preferable for more accurate B_1^+ map. Although the reliability range is narrower for increasing ΔB_0 , the estimated B_1^+ with α approximately 60° shows less sensitivity to off-resonance and T_2 values compared to smaller α values.

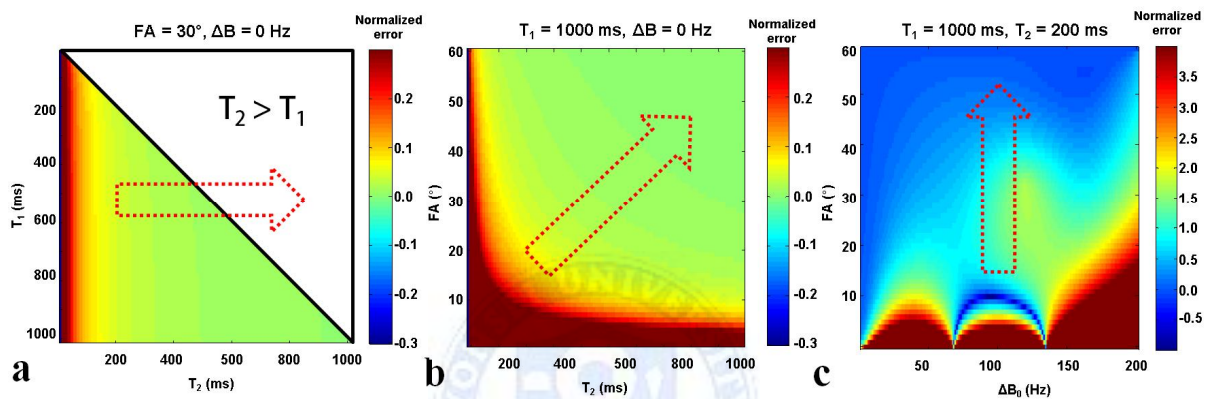


Figure 5.2 Simulation results with varying T_1 , T_2 , FA and ΔB_0 . Fixed parameters are noted above each figure and varying parameters are along x and y axes. Normalized error was calculated (estimated / true - 1) thus 0.0 is the best result. (a) B_1^+ estimation performance with varying (a) T_1 and T_2 , (b) T_2 and FA and (c) FA and ΔB_0 . A red dotted arrow on each figure indicates the direction of improved B_1^+ estimation.

5.3.2 Experiments

The results of the phantom experiments performed with various α values are presented in Fig.5.3. Similar to the simulation results, the calculated B_1^+ map was overestimated with small α and getting close to the conventional DAM B_1^+ map as α increases. Furthermore, as indicated by the dotted region in Fig.5.3(a), the resulting B_1^+ map with small α was sensitive

to off-resonance induced by air-water susceptibility difference. The bSSFP images before and after B_1^+ correction are shown in Fig. 5.3. After correction, the spatial inhomogeneities were reduced. However, there seems to be remaining spatial inhomogeneity, which seems to correlate with the receiver coil sensitivities. The calculated σ values are plotted in Fig.5.3(b) as a function of FA and their differences between before and after correction are also plotted in Fig.5.3(c). According to these results larger FAs produce improved results.

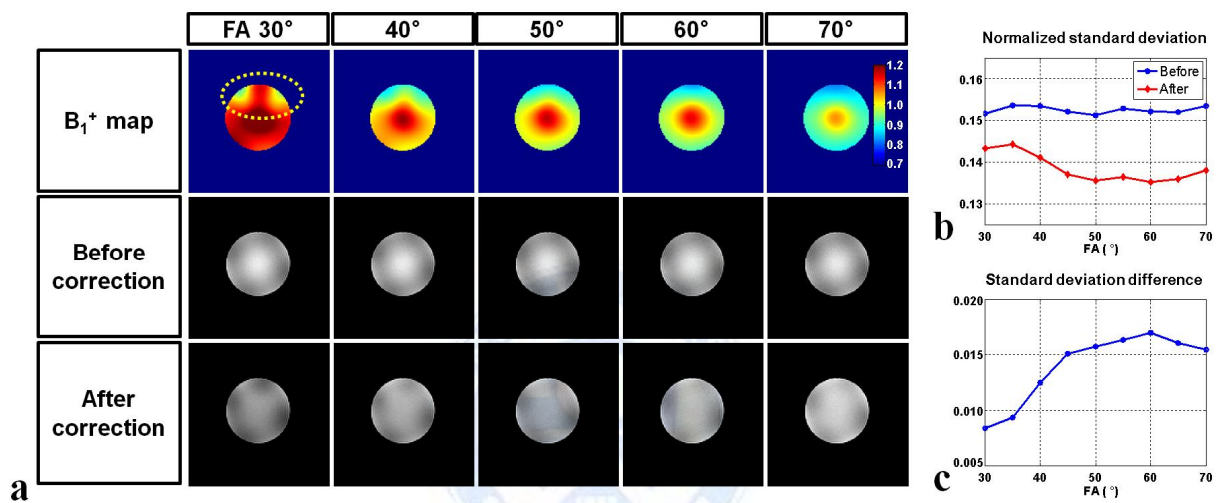


Figure 5.3 Phantom experiment results with various α values. The estimated B_1^+ maps and bSSFP images before and after B_1^+ correction are shown in (a). The estimated B_1^+ maps are overestimated with small FA and erroneous pattern (yellow dotted region) is observed due to the inhomogeneous B_0 field from the air bubbles close to the imaging slice. To estimate the increase of the uniformity after B_1^+ correction, normalized standard deviations of intensity values are shown in (b) and their differences are in (c). Note that the biggest standard deviation reduction is observed at $\alpha = 60^\circ$.

Figure 5.4 shows further details of the phantom experiment result with $\alpha = 60^\circ$ which corresponds to the FA sequence of 60° - 120° - 180° - 105° - 30° . I_1 and I_2 images acquired using single-shot spiral trajectory (Fig. 4a,b), B_1^+ map calculated using these two images [Fig.

5.4(c)], and B_1^+ map from the standard DAM (Fig. 4d) are provided. The bSSFP image with $\beta_{im}=30^\circ$ before correction [Fig. 5.4(e)] and the after correction [Fig. 5.4(f)] are shown. The intensity line plots at the center of the phantom images [Fig. 5.4(f)] show that B_1^+ -induced intensity modulation is alleviated after correction. The correlation coefficient coefficients between the proposed and the DAM B_1^+ maps were 0.966 at $\alpha = 60^\circ$.

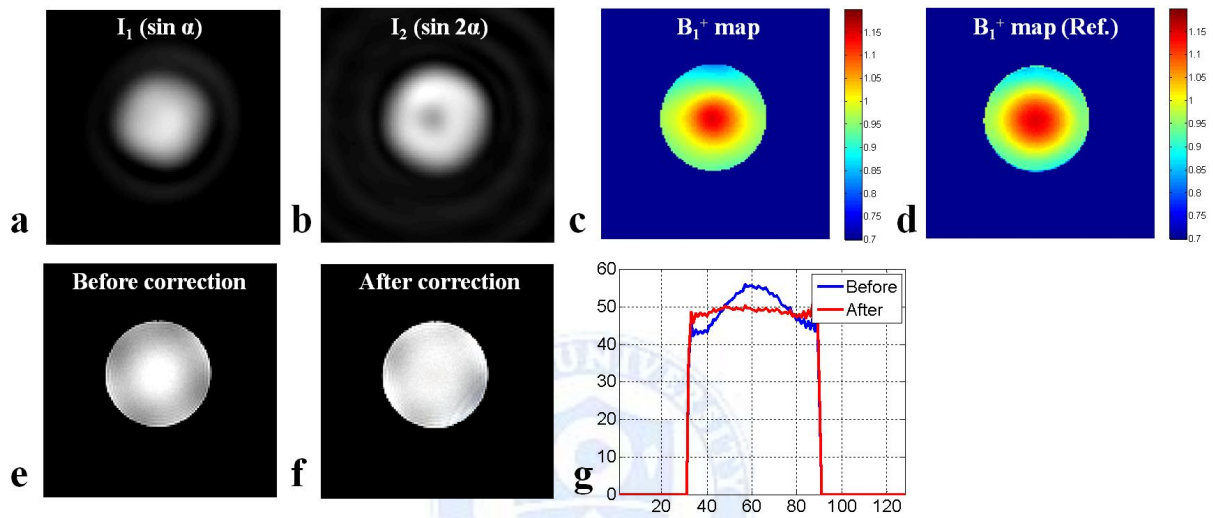


Figure 5.4 Step-by-step presentation of the phantom experiment using $\alpha = 60^\circ$. (a) I_1 . (b) I_2 . (c) B_1^+ map calculated with (a) and (b) based on DAM. (d) B_1^+ map with the conventional SE DAM. (e) Acquired normal bSSFP image with $\beta_{im} = 30^\circ$. (f) B_1^+ corrected bSSFP image. (g) Intensity line plots at the center of the images (e) and (f).

In vivo brain and liver results are shown in Fig. 5.5. The bSSFP images are shown before and after B_1^+ correction. The central brightening typically occurring in brain imaging was reduced after intensity correction as seen in the zoomed and color coded images in Fig.5.5(a) and (b). Furthermore, overall tissue intensities were more homogeneous after correction for each tissue type especially in the white matter region. The resulting before and after B_1^+ correction images and B_1^+ map for the liver scan are shown in Fig.5.5(e-f). In order to show the effect of B_1^+ correction more clearly, center regions are zoomed in and presented.

Intensities of spinal cord, vertebral body and left lobe of liver were homogenized after B_1^+ correction. B_1^+ pattern in liver is different to that in brain because the size of abdomen is much bigger than the wavelength of RF pulse in 3T. Some distortions due to B_0 inhomogeneity were observed at the air-tissue boundaries (arrows in Fig 5.5(f)).

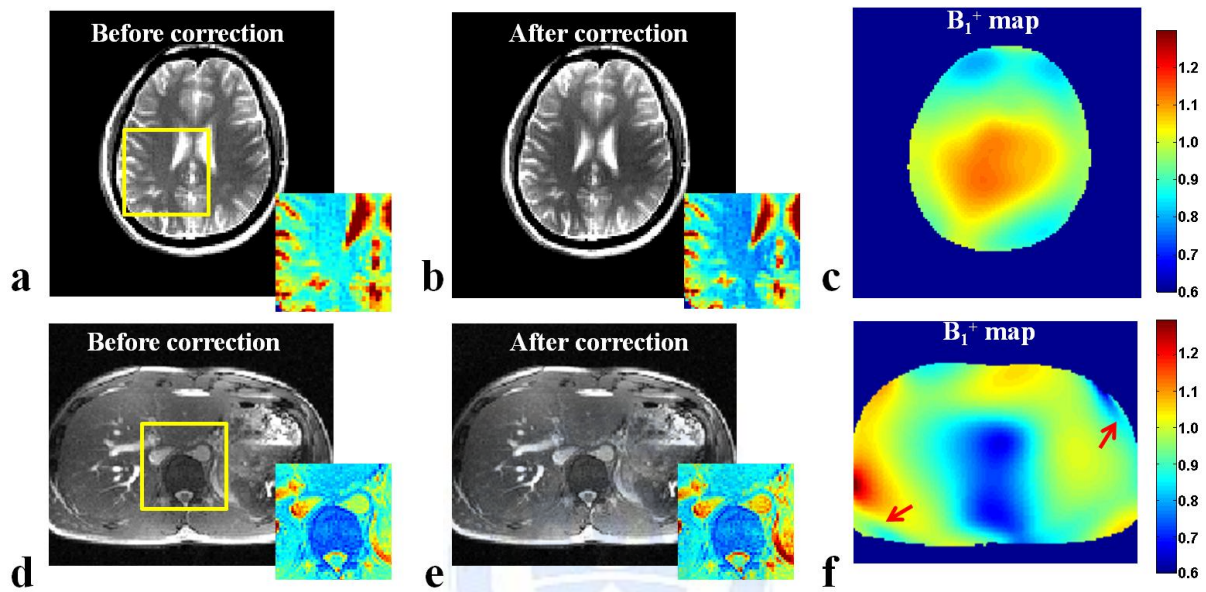


Figure 5.5 In vivo brain (a-c) and liver (d-f) images using the proposed method with $\alpha = 60^\circ$. (a, d) Acquired normal bSSFP images with $\beta_{im} = 30^\circ$. (b, e) B_1^+ corrected bSSFP images. (c, f) B_1^+ map using the proposed method. The yellow boxed regions are presented in jet color to show the improvement after B_1^+ correction more clearly.

5.4 Discussion

In this chapter, a fast B_1^+ mapping and correction methods using transient-state signal in bSSFP is presented. B_1^+ map was estimated without scan time increment and simultaneously acquired bSSFP image was corrected using this B_1^+ information. The simulation and experiment results show good agreements about B_1^+ mapping FA and off-resonance responses. Inhomogeneous intensity patterns of the acquired images are mitigated after B_1^+ correction.

The method was based on two assumptions 1) T_1 and T_2 relaxation during 2TR is negligible and 2) B_1^+ slowly varies in spatial domain. In order to quantify the B_1^+ estimation error caused by the first assumption, Bloch simulations with varying T_1 , T_2 , FA and ΔB_0 were performed. According to the simulation results, the estimated B_1^+ was more sensitive to T_2 than T_1 . The resulting B_1^+ was overestimated at short T_2 tissue. In order to alleviate T_2 sensitivity of B_1^+ estimation, applying large FA such as $\alpha = 60^\circ$ can be one solution (Fig. 2b and Fig. 3). Note that this FA was previously shown to be the most SNR efficient in the original DAM technique (32). Global distribution B_1^+ map can be represented with low resolution under the assumption of slow varying B_1^+ field. In a previous studies which used this assumption, B_1^+ map was estimated using low-frequency part of the k-space of the acquired image itself (98) or polynomial modelling (99). These techniques work well when the acquired image has low-contrast among different tissues. In other words, the B_1^+ estimation and correction performance depends on image contrast. The proposed method estimates B_1^+ map based on DAM, thus tissue contrast is cancelled out during dividing two different FA images. If higher resolution B_1^+ map is required, early transient-state signals can be used to fill low frequency region in k-space and the following signals can be used to fill high frequency k-space regions. Interleaved spiral acquisition technique could be another possible solution. However, the signal at the center of k-space is different for each interleaf, consequently, some image artifacts or B_1^+ estimation error will occur. Further investigation and optimization on continuing transient-state signals and FAs are required to increase spatial resolution of the proposed B_1^+ mapping technique.

BSSFP pulse sequence is widely used because of its high SNR in short acquisition time. However, it is inherently sensitive to off-resonance which results in signal enhancement or nulling called banding artifact. In the proposed method, the performance of B_1^+ estimation is also affected by off-resonance. According to the simulation result, B_1^+ is generally

overestimated as a function of off-resonance. This off-resonance effect reduces along FA increment. From the simulation result, the appropriate FA for B_1^+ mapping was approximately $\alpha = 60^\circ$. According to the experiment result in Fig.3, the estimated B_1^+ maps with small FAs (less than 45°) show ΔB_0 -related pattern and this distorted pattern reduces with increasing FA. The correction performances estimated by the difference of the normalized standard deviation of intensity before and after correction show no big difference with FAs over 45° . In general, considering the spatial nonuniformity of the FA themselves, it would seem that the practical FA for the proposed B_1^+ mapping should α over 50° .

In conclusion, a transient-state B_1^+ mapping method is presented based on bSSFP sequence. This technique can also be used as a prescan for B_1^+ compensation or shimming. Furthermore, the proposed method can be applied to other images acquired with different pulse sequences. In addition, complex B_1^+ mapping can be achievable assuming that the excited spins are refocused and the phase of bSSFP image reflects B_1^+ phase (7). Further investigations are required on interleaved B_1^+ acquisition for resolution flexibility and three-dimensional B_1^+ estimation.

According to the previous B_1^+ mapping techniques, their performances such as SNR, time efficiency, and estimation accuracy were sensitive to tissue relaxations. In SE based methods, long TR or saturation technique were adapted to reduce the effect of T_1 relaxation. In GRE based methods, TR much shorter than T_1 and perfect spoiling were assumed to ignore T_1 relaxation effect and residual transverse magnetization before next excitation. However, in the proposed method, we observed that the estimation performance was more sensitive to T_2 than T_1 although the proposed method is based on bSSFP technique which uses both longitudinal and transverse magnetizations. Since the TR of bSSFP is much shorter than T_1 , the relaxation effect could be minimized effectively. On the other hand, refocused signal used

in the proposed technique could be a source of T_2 sensitive result although TE was much shorter than T_2 . This T_2 related error can be reduced by adjusting FAs for B_1^+ mapping.



Chapter 6

Summary

“Additional gradients” is an essential keyword throughout this dissertation. Basic function of gradient field is encoding spin’s location by inducing linear field along specific direction. Several methods improving acquisition speed and/or image quality are presented by applying or combining additional gradients

In chapter 3, modified multi- and wide band imaging techniques are described, which use additional gradients to reduce the total acquisition time and increase the image quality. In multiband imaging, multi slices are simultaneously excited and these slices are stacked and aliased in the acquired image. This image is reconstructed to multi slices with the coil sensitivity information. Reconstruction performance is improved by introducing slice dependent shifts along readout direction using the additional gradient. In wideband imaging, fast acquisition is achieved by reducing the total number of PEs. The reduced PEs cause aliasings along PE direction and these aliasings are separated along the readout direction by increasing the total readout bandwidth. Further acceleration is achieved using parallel imaging technique, GRAPPA.

In chapter 4, MRT technique is introduced. Originally, tomosynthesis technique is used in x-ray to reconstruct 3D image from the 2D projection images. In MRI, volume (slice) selective projection images at different angle can be acquired using additional gradients. Optimal reconstruction method for MRT is determined by the SNR and PSF. With this technique, partial volume artifact along specific direction is reduced and aliasing artifacts occurred at the upper and lower slices in common 3D imaging due to the imperfect excitation profile are also resolved.

In chapter 5, a fast B_1^+ mapping and correction method in bSSFP imaging is presented. The transient-state signals are modified using variable flip angles to acquire B_1^+ information. Simulations were performed to estimate the estimation error according to T1, T2, off-resonance and FA. The phantom experiment results are matched well to the simulation results. The correction performance is evaluated using the improvement in the normalized standard deviations of intensity values before and after correction. The validity of this method is demonstrated by comparing with the conventional B_1^+ mapping technique in the phantom and in-vivo.

The works presented in this dissertation have their own advantages. Fast acquisition in CAIPIVAT gives a chance to increase multi-slice factor by providing the better reconstruction condition. Furthermore, it can be useful for reducing data acquisition time in SEMAC which has been proposed for correcting metal induced artifacts in conjunction with VAT. In the extended wideband imaging, its high acceleration capability can be useful for volumetric pre-scan imaging to acquire screening data for health checkups or global variations of B_0 field or coil sensitivities which need not to be high resolution. This technique is especially useful for huge volumetric imaging such as whole body imaging because it shows the best acceleration performance when imaging a long object along PE direction. The alternative 3D imaging technique, MRT, can resolve the slice aliasing by taking slice profile inhomogeneity into account for reconstruction process. This extended FOV reconstruction may be useful for localization of flow and motion components. Since flow components (along the slice direction) are encoded simultaneously during the data acquisition, velocity measurements seem to be feasible. Further exploration of these potential applications is a subject of future studies. Fast B_1^+ mapping technique can be employed in a prescan manner for B_1 shimming or correction. Since, this technique based on bSSFP, further extensions can be a combination with variable flip angle scheme for time efficiency and SNR and/or

dynamic phase cycling scheme for banding free imaging. Next object is, therefore, developing an ultimate bSSFP which means banding-free, optimized SNR, B_1^+ corrected, no wasting time bSSFP.



References

1. Bloch F. Nuclear Induction. *Physical Review* 1946;70(7-8):460-474.
2. Mansfield P. Spatial mapping of the chemical shift in NMR. *Magn Reson Med* 1984;1(3):370-386.
3. Dumoulin CL, Souza SP, Walker MF, Wagle W. Three-dimensional phase contrast angiography. *Magn Reson Med* 1989;9(1):139-149.
4. Mariappan YK, Glaser KJ, Ehman RL. Magnetic resonance elastography: a review. *Clinical anatomy* 2010;23(5):497-511.
5. Ogawa S, Lee TM, Nayak AS, Glynn P. Oxygenation-sensitive contrast in magnetic resonance image of rodent brain at high magnetic fields. *Magn Reson Med* 1990;14(1):68-78.
6. Denis de Senneville B, Quesson B, Moonen CT. Magnetic resonance temperature imaging. *International journal of hyperthermia : the official journal of European Society for Hyperthermic Oncology, North American Hyperthermia Group* 2005;21(6):515-531.
7. Katscher U, Kim DH, Seo JK. Recent progress and future challenges in MR electric properties tomography. *Computational and mathematical methods in medicine* 2013;2013:546562.
8. Haacke EM, Xu Y, Cheng YC, Reichenbach JR. Susceptibility weighted imaging (SWI). *Magn Reson Med* 2004;52(3):612-618.
9. Kong X, Zhu M, Xia L, Crozier S, Wang Q, Ni Z, Liu F. A novel passive shimming method for the correction of magnetic fields above the patient bed in MRI. *Journal of magnetic resonance* 2015;257:64-69.

10. Koch KM, Brown PB, Rothman DL, de Graaf RA. Sample-specific diamagnetic and paramagnetic passive shimming. *Journal of magnetic resonance* 2006;182(1):66-74.
11. Osterbauer RA, Wilson JL, Calvert GA, Jezzard P. Physical and physiological consequences of passive intra-oral shimming. *NeuroImage* 2006;29(1):245-253.
12. Juchem C, Muller-Bierl B, Schick F, Logothetis NK, Pfeuffer J. Combined passive and active shimming for in vivo MR spectroscopy at high magnetic fields. *Journal of magnetic resonance* 2006;183(2):278-289.
13. Lauterbur PC. Image-Formation by Induced Local Interactions - Examples Employing Nuclear Magnetic-Resonance. *Clinical orthopaedics and related research* 1989(244):3-6.
14. Mansfield P. Multi-planar image formation using NMR spin echoes. *Journal of Physics C: Solid State Physics* 1977;10(3):L55.
15. Beatty PJ, Nishimura DG, Pauly JM. Rapid gridding reconstruction with a minimal oversampling ratio. *IEEE Trans Med Imaging* 2005;24(6):799-808.
16. Pruessmann KP, Weiger M, Scheidegger MB, Boesiger P. SENSE: sensitivity encoding for fast MRI. *Magn Reson Med* 1999;42(5):952-962.
17. Griswold MA, Jakob PM, Heidemann RM, Nittka M, Jellus V, Wang J, Kiefer B, Haase A. Generalized autocalibrating partially parallel acquisitions (GRAPPA). *Magn Reson Med* 2002;47(6):1202-1210.
18. Busch MG, Finsterbusch J. Hadamard-encoding combined with two-dimensional-selective radiofrequency excitations for flexible and efficient acquisitions of multiple voxels in MR spectroscopy. *Journal of magnetic resonance imaging : JMRI* 2012;35(4):976-983.
19. Wu EL, Huang YA, Chiueh TD, Chen JH. Single-frequency excitation wideband MRI (SE-WMRI). *Med Phys* 2015;42(7):4320-4328.

20. Wu EL, Chen JH, Chiueh TD. Wideband MRI: theoretical analysis and its applications. Conference proceedings : Annual International Conference of the IEEE Engineering in Medicine and Biology Society IEEE Engineering in Medicine and Biology Society Annual Conference 2010;2010:5681-5684.
21. Larkman DJ, Hajnal JV, Herlihy AH, Coutts GA, Young IR, Ehnholm G. Use of multicoil arrays for separation of signal from multiple slices simultaneously excited. Journal of magnetic resonance imaging : JMRI 2001;13(2):313-317.
22. Breuer FA, Blaimer M, Heidemann RM, Mueller MF, Griswold MA, Jakob PM. Controlled aliasing in parallel imaging results in higher acceleration (CAIPIRINHA) for multi-slice imaging. Magn Reson Med 2005;53(3):684-691.
23. Zhuo J, Gullapalli RP. AAPM/RSNA physics tutorial for residents: MR artifacts, safety, and quality control. Radiographics : a review publication of the Radiological Society of North America, Inc 2006;26(1):275-297.
24. Meyer CH, Pauly JM, Macovski A, Nishimura DG. Simultaneous spatial and spectral selective excitation. Magn Reson Med 1990;15(2):287-304.
25. Glover GH, Schneider E. Three-point Dixon technique for true water/fat decomposition with B0 inhomogeneity correction. Magn Reson Med 1991;18(2):371-383.
26. Cho ZH, Kim DJ, Kim YK. Total inhomogeneity correction including chemical shifts and susceptibility by view angle tilting. Med Phys 1988;15(1):7-11.
27. Hornak JP, Szumowski J, Bryant RG. Magnetic field mapping. Magnetic Resonance in Medicine 1988;6(2):158-163.
28. Yang QX, Wang J, Zhang X, Collins CM, Smith MB, Liu H, Zhu X-H, Vaughan JT, Ugurbil K, Chen W. Analysis of wave behavior in lossy dielectric samples at high field. Magnetic Resonance in Medicine 2002;47(5):982-989.

29. Venkatesan R, Lin W, Haacke EM. Accurate determination of spin-density and T1 in the presence of RF-field inhomogeneities and flip-angle miscalibration. *Magn Reson Med* 1998;40(4):592-602.
30. Deoni SC. High-resolution T1 mapping of the brain at 3T with driven equilibrium single pulse observation of T1 with high-speed incorporation of RF field inhomogeneities (DESPOT1-HIFI). *Journal of magnetic resonance imaging : JMRI* 2007;26(4):1106-1111.
31. Cooper MA, Nguyen TD, Spincemaille P, Prince MR, Weinsaft JW, Wang Y. Flip angle profile correction for T1 and T2 quantification with look-locker inversion recovery 2D steady-state free precession imaging. *Magnetic Resonance in Medicine* 2012;68(5):1579-1585.
32. Stollberger R, Wach P. Imaging of the active B1 field in vivo. *Magnetic Resonance in Medicine* 1996;35(2):246-251.
33. Wang J, Qiu M, Yang QX, Smith MB, Constable RT. Measurement and correction of transmitter and receiver induced nonuniformities in vivo. *Magnetic Resonance in Medicine* 2005;53(2):408-417.
34. Cunningham CH, Pauly JM, Nayak KS. Saturated double-angle method for rapid B1+ mapping. *Magnetic Resonance in Medicine* 2006;55(6):1326-1333.
35. Ganter C, Settles M, Dregely I, Santini F, Scheffler K, Bieri O. B1+-mapping with the transient phase of unbalanced steady-state free precession. *Magnetic Resonance in Medicine* 2013;70(6):1515-1523.
36. Spielman DM, Pauly JM, Meyer CH. Magnetic resonance fluoroscopy using spirals with variable sampling densities. *Magnetic Resonance in Medicine* 1995;34(3):388-394.

37. Irarrazabal P, Nishimura DG. Fast Three Dimensional Magnetic Resonance Imaging. *Magnetic Resonance in Medicine* 1995;33(5):656-662.
38. Feinberg DA, Hale JD, Watts JC, Kaufman L, Mark A. Halving MR imaging time by conjugation: demonstration at 3.5 kG. *Radiology* 1986;161(2):527-531.
39. Sodickson DK, Manning WJ. Simultaneous acquisition of spatial harmonics (SMASH): Fast imaging with radiofrequency coil arrays. *Magnetic Resonance in Medicine* 1997;38(4):591-603.
40. Pruessmann KP, Weiger M, Scheidegger MB, Boesiger P. SENSE: Sensitivity encoding for fast MRI. *Magnetic Resonance in Medicine* 1999;42(5):952-962.
41. Griswold MA, Jakob PM, Heidemann RM, Nittka M, Jellus V, Wang J, Kiefer B, Haase A. Generalized autocalibrating partially parallel acquisitions (GRAPPA). *Magnetic Resonance in Medicine* 2002;47(6):1202-1210.
42. Weaver JB. Simultaneous multislice acquisition of MR images. *Magnetic Resonance in Medicine* 1988;8(3):275-284.
43. Wu EL, Chen J-H, Chiueh T-D. Wideband MRI: a new dimension of MR image acceleration. In: *Proceedings of the 17th annual meeting of ISMRM. Hawaii, USA2009.* p 2678.
44. Breuer FA, Blaimer M, Heidemann RM, Mueller MF, Griswold MA, Jakob PM. Controlled aliasing in parallel imaging results in higher acceleration (CAIPIRINHA) for multi-slice imaging. *Magnetic Resonance in Medicine* 2005;53(3):684-691.
45. Larkman DJ, Hajnal JV, Herlihy AH, Coutts GA, Young IR, Ehnholm G. Use of multicoil arrays for separation of signal from multiple slices simultaneously excited. *Journal of Magnetic Resonance Imaging* 2001;13(2):313-317.
46. Paley MNJ, Lee KJ, Wild JM, Fischele S, Whitby EH, Wilkinson ID, Van Beek EJ, Griffiths PD. B1AC-MAMBA: B1 array combined with multiple-acquisition micro

- B0 array parallel magnetic resonance imaging. *Magnetic Resonance in Medicine* 2003;49(6):1196-1200.
47. Paley MNJ, Lee KJ, Wild JM, Griffiths PD, Whitby EH. Simultaneous parallel inclined readout image technique. *Magn Reson Imaging* 2006;24(5):557-562.
 48. Wu F-H, Wu E, Kuo L-W, Chen J-H, Chiueh T-D. Wideband Parallel Imaging. In: *Proceedings of the 17th annual meeting of ISMRM. Hawaii, USA2009.* p 2677.
 49. Wu EL, Chen JH, Chiueh TD. Wideband MRI: Theoretical analysis and its applications. 2010 Aug. 31 2010-Sept. 4 2010; Buenos Aires, Argentina. p 5681-5684.
 50. Cho ZH, Kim DJ, Kim YK. Total inhomogeneity correction including chemical shifts and susceptibility by view angle tilting. *Medical Physics* 1988;15(1):7-11.
 51. Zho S-Y, Kim D-H. Time-varying view angle tilting with spiral readout gradients. *Magnetic Resonance in Medicine* 2011:n/a-n/a.
 52. Butts K, Pauly JM, Gold GE. Reduction of blurring in view angle tilting MRI. *Magn Reson Med* 2005;53(2):418-424.
 53. Kim M-O, Kwak S, Kim D-H. Deblurring in view angle tilting. 2014; Milan, Italy. p 1647.
 54. Conolly S, Nishimura D, Macovski A, Glover G. Variable-rate selective excitation. *Journal of Magnetic Resonance (1969)* 1988;78(3):440-458.
 55. Norris DG, Koopmans PJ, Boyacioglu R, Barth M. Power Independent of Number of Slices (PINS) radiofrequency pulses for low-power simultaneous multislice excitation. *Magn Reson Med* 2011;66(5):1234-1240.
 56. Setsompop K, Gagoski BA, Polimeni JR, Witzel T, Wedeen VJ, Wald LL. Blipped-controlled aliasing in parallel imaging for simultaneous multislice echo planar imaging with reduced g-factor penalty. *Magn Reson Med* 2012;67(5):1210-1224.

57. Jackson JJ, Meyer CH, Nishimura DG, Macovski A. Selection of a convolution function for Fourier inversion using gridding [computerised tomography application]. *Medical Imaging, IEEE Transactions on* 1991;10(3):473-478.
58. Blaimer M, Breuer F, Mueller M, Heidemann RM, Griswold MA, Jakob PM. SMASH, SENSE, PILS, GRAPPA: How to Choose the Optimal Method. *Topics in Magnetic Resonance Imaging* 2004;15(4):223-236.
59. Lu W, Pauly KB, Gold GE, Pauly JM, Hargreaves BA. SEMAC: Slice encoding for metal artifact correction in MRI. *Magnetic Resonance in Medicine* 2009;62(1):66-76.
60. Miao J, Wong WCK, Narayan S, Wilson DL. K-space reconstruction with anisotropic kernel support (KARAOKE) for ultrafast partially parallel imaging. *Medical Physics* 2011;38(11):6138-6142.
61. Sodickson DK, McKenzie CA. A generalized approach to parallel magnetic resonance imaging. *Medical Physics* 2001;28(8):1629-1643.
62. Meyer CH, Hu BS, Nishimura DG, Macovski A. Fast spiral coronary artery imaging. *Magn Reson Med* 1992;28(2):202-213.
63. Pipe JG. Motion correction with PROPELLER MRI: application to head motion and free-breathing cardiac imaging. *Magn Reson Med* 1999;42(5):963-969.
64. Barger AV, Block WF, Toropov Y, Grist TM, Mistretta CA. Time-resolved contrast-enhanced imaging with isotropic resolution and broad coverage using an undersampled 3D projection trajectory. *Magn Reson Med* 2002;48(2):297-305.
65. Qian Y, Boada FE. Acquisition-weighted stack of spirals for fast high-resolution three-dimensional ultra-short echo time MR imaging. *Magn Reson Med* 2008;60(1):135-145.
66. Dobbins JT, 3rd, Godfrey DJ. Digital x-ray tomosynthesis: current state of the art and clinical potential. *Phys Med Biol* 2003;48(19):R65-106.

67. Godfrey DJ, McAdams HP, Dobbins JT, 3rd. Optimization of the matrix inversion tomosynthesis (MITS) impulse response and modulation transfer function characteristics for chest imaging. *Medical Physics* 2006;33(3):655-667.
68. Kolitsi Z, Panayiotakis G, Anastassopoulos V, Scodras A, Pallikarakis N. A multiple projection method for digital tomosynthesis. *Medical Physics* 1992;19(4):1045-1050.
69. Maravilla KR, Murry RC, Jr., Horner S. Digital tomosynthesis: technique for electronic reconstructive tomography. *AJR Am J Roentgenol* 1983;141(3):497-502.
70. Ren L, Zhang J, Thongphiew D, Godfrey DJ, Jackie Wu Q, Zhou S-M, Yin F-F. A novel digital tomosynthesis (DTS) reconstruction method using a deformation field map. *Medical Physics* 2008;35(7):3110.
71. Sone S, Kasuga T, Sakai F, Aoki J, Izuno I, Tanizaki Y, Shigeta H, Shibata K. Development of a high-resolution digital tomosynthesis system and its clinical application. *Radiographics* 1991;11(5):807-822.
72. Wu T, Moore RH, Rafferty EA, Kopans DB. A comparison of reconstruction algorithms for breast tomosynthesis. *Medical Physics* 2004;31(9):2636.
73. Godfrey DJ, Warp RJ, Dobbins Iii JT. Optimization of matrix inverse tomosynthesis. In: Antonuk LE, Yaffe MJ, editors. 1 ed. Volume 4320. San Diego, CA, USA: SPIE; 2001. p 696-704.
74. Fleischmann D, Boas F. Computed tomography—old ideas and new technology. *Eur Radiol* 2011;21(3):510-517.
75. Haldar JP, Zhi-Pei L. On MR experiment design with quadratic regularization. 2011 March 30 2011-April 2 2011. p 1676-1679.
76. Larson PZ, Gurney PT, Nishimura DG. Anisotropic field-of-views in radial imaging. *IEEE Trans Med Imaging* 2008;27(1):47-57.

77. Kim M-O, Kim D-H. SNR analysis of 3D magnetic resonance tomosynthesis (MRT) imaging. In: Pelc NJ, Nishikawa RM, Whiting BR, editors 2012; San Diego, California, USA. SPIE. p 83136C-83136.
78. Sechopoulos I, Ghetti C. Optimization of the acquisition geometry in digital tomosynthesis of the breast: AAPM; 2009. 1199-1207 p.
79. Scheffler K, Lehnhardt S. Principles and applications of balanced SSFP techniques. *Eur Radiol* 2003;13(11):2409-2418.
80. Chavhan GB, Babyn PS, Jankharia BG, Cheng HL, Shroff MM. Steady-state MR imaging sequences: physics, classification, and clinical applications. *Radiographics* : a review publication of the Radiological Society of North America, Inc 2008;28(4):1147-1160.
81. Bieri O, Scheffler K. Fundamentals of balanced steady state free precession MRI. *Journal of Magnetic Resonance Imaging* 2013;38(1):2-11.
82. Bangerter NK, Hargreaves BA, Vasanawala SS, Pauly JM, Gold GE, Nishimura DG. Analysis of multiple-acquisition SSFP. *Magn Reson Med* 2004;51(5):1038-1047.
83. Zelaya FO, Roffmann WU, Crozier S, Teed S, Gross D, Doddrell DM. Direct visualisation of B1 inhomogeneity by flip angle dependency. *Magnetic resonance imaging* 1997;15(4):497-504.
84. Scheffler K. On the transient phase of balanced SSFP sequences. *Magnetic Resonance in Medicine* 2003;49(4):781-783.
85. Lohan DG, Saleh R, Tomasian A, Krishnam M, Finn JP. Current status of 3-T cardiovascular magnetic resonance imaging. *Topics in magnetic resonance imaging* : TMRI 2008;19(1):3-13.
86. Wieben O, Francois C, Reeder SB. Cardiac MRI of ischemic heart disease at 3 T: potential and challenges. *European journal of radiology* 2008;65(1):15-28.

87. Dagia C, Ditchfield M. 3 T MRI in paediatrics: Challenges and clinical applications. *European journal of radiology* 2008;68(2):309-319.
88. Suttie JJ, DelaBarre L, Pitcher A, van de Moortele PF, Dass S, Snyder CJ, Francis JM, Metzger GJ, Weale P, Ugurbil K, Neubauer S, Robson M, Vaughan T. 7 Tesla (T) human cardiovascular magnetic resonance imaging using FLASH and SSFP to assess cardiac function: validation against 1.5 T and 3 T. *NMR in biomedicine* 2012;25(1):27-34.
89. Sung K, Nayak KS. Measurement and characterization of RF nonuniformity over the heart at 3T using body coil transmission. *Journal of Magnetic Resonance Imaging* 2008;27(3):643-648.
90. Katscher U, Voigt T, Findekle C, Vernickel P, Nehrke K, Dossel O. Determination of electric conductivity and local SAR via B_1 mapping. *IEEE Trans Med Imaging* 2009;28(9):1365-1374.
91. Metzger GJ, Snyder C, Akgun C, Vaughan T, Ugurbil K, Van de Moortele P-F. Local B_1+ shimming for prostate imaging with transceiver arrays at 7T based on subject-dependent transmit phase measurements. *Magnetic Resonance in Medicine* 2008;59(2):396-409.
92. van den Bergen B, Stolk CC, Berg JB, Lagendijk JJ, Van den Berg CA. Ultra fast electromagnetic field computations for RF multi-transmit techniques in high field MRI. *Physics in medicine and biology* 2009;54(5):1253-1264.
93. Gilbert KM, Curtis AT, Gati JS, Klassen LM, Menon RS. A radiofrequency coil to facilitate $B_1(+)$ shimming and parallel imaging acceleration in three dimensions at 7 T. *NMR in biomedicine* 2011;24(7):815-823.

94. Voigt T, Katscher U, Doessel O. Quantitative conductivity and permittivity imaging of the human brain using electric properties tomography. *Magn Reson Med* 2011;66(2):456-466.
95. Klose U. Mapping of the radio frequency magnetic field with a MR snapshot FLASH technique. *Med Phys* 1992;19(4):1099-1104.
96. Jiru F, Klose U. Fast 3D radiofrequency field mapping using echo-planar imaging. *Magn Reson Med* 2006;56(6):1375-1379.
97. Yarnykh VL. Actual flip-angle imaging in the pulsed steady state: a method for rapid three-dimensional mapping of the transmitted radiofrequency field. *Magn Reson Med* 2007;57(1):192-200.
98. Yang S, Nam Y, Kim MO, Kim EY, Park J, Kim DH. Computer-aided detection of metastatic brain tumors using magnetic resonance black-blood imaging. *Investigative radiology* 2013;48(2):113-119.
99. Tincher M, Meyer CR, Gupta R, Williams DM. Polynomial modeling and reduction of RF body coil spatial inhomogeneity in MRI. *IEEE Trans Med Imaging* 1993;12(2):361-365.

국문요약

추가 경사 자장을 이용한 자기 공명 영상 고속 획득

기법 및 인공물 보정 기술 개발

자기 공명 영상은 핵 자기 공명 현상에 그 기반을 두고 있는데, 핵 자기 공명 현상 관찰에서 영상화 단계로 넘어오게 되는데에는 경사 자장의 역할이 매우 중요했다. 경사자장으로 공간적 위치에 따라 스핀의 주파수 및 위상을 다르게 하여 위치 정보를 획득할 수 있게 되었기 때문이다. 뿐만아니라 선형 자장은 모양 및 가해지는 패턴을 바꾸어 신호 감쇄, 자화 준비, 유체 감지 등의 여러 가지 목적으로 사용할 수 있다. 여기에 경사 자장을 가해주는 코일의 지속적인 발전은 자장이 공간적, 시간적으로 보다 복잡하고 다양한 패턴으로 가해질 수 있게 해주었다. 본 논문은 추가 경사 자장을 이용한 고속 획득 기법과 인공물 보정 기술 개발에 초점을 두고 있다.

본 논문에서는 추가 경사 자장을 이용하여 다중 및 광대역 영상 획득 기법, 자기 공명 단층 영상 합성법, 고속 B_1^+ 지도화 및 보정 기법을 소개한다.

먼저 다중 및 광대역 영상 획득 기법은 추가 경사 자장을 이용하여 고속 영상 기법에서 발생하는 겹침 인공물을 최소화하여 추가 고속화 및 복원 영상의 질적 향상을 도모한다. 다음으로 자기 공명 단층 영상 합성법에서는 추가 경사 자장을 이용하여 여러 장의 서로 다른 각도에서 투사한 것과 유사한 이차원 자기 공명 단면 영상을 얻어 삼차원으로 복원하여 부분 채적 인공물 및 단면 겹침 현상을 감소 시킨다. 마지막으로 한 펄스열에서 경사 자장을 조절하여 두 개의 획득

래적을 이용해서 B_1^+ 분포를 지도화하고 그 정보를 이용해 연속적으로 얻어진 일반 영상에서 밝기 왜곡을 완화 시킨다.

위 연구 성과들은 자기 공명 영상에서 사용하는 경사 자장을 응용하는 부분에서 많은 도움이 될 수 있을 것으로 생각하고, 영상화 기술 발전에 기여하여 고속 영상 획득을 통한 환자의 편의성 증대 및 인공물 완화를 통한 자기 공명 영상의 질적 향상에 이바지 할 수 있을 것으로 기대한다.

핵심어: 자기공명영상, 경사 자장 조절, 영상 획득 고속화 기법, 영상 인공물 보정 기술

